Measurement of the Single Top t-channel Cross Section Using a Cut Based Analysis With the ATLAS Detector in pp Collisions at $\sqrt{s} = 7$ TeV

Matilde Teixeira Dias Castanheira

A thesis submitted in fulfilment of the requirements of the degree of Doctor of Philosophy to Queen Mary University of London

Supervisor: Professor Steve Lloyd

Co-Supervisor: Dr. Lucio Cerrito

October 2013

To Rui
Who taught me to dance

Abstract

This thesis presents studies of the single top t-channel in the electron plus jets mode. In order to understand this channel, an account of the present theoretical models is given. This work relies on collisions data from the ATLAS detector and its components are presented here. A summary of the work involving the SCT, part of the tracking system in ATLAS, is also explained here. Studies were performed to optimize the measurement of the Lorentz Angle of the holes in the Silicon for the initial data taking period.

The data studied was acquired by ATLAS during 2011, with a total integrated luminosity of 4.7 pb^{-1} at a $\sqrt{s} = 7$ TeV. Monte Carlo simulation of signal and background events was also used throughout.

Background studies were performed to correctly determine the expected amount of QCD via the Jet Electron data-driven method and of light or heavy flavour jets produced in association with a W boson, which is one of the dominant backgrounds for the t-channel.

A cut based analysis was then applied to the data and simulation in order to better discriminate the t-channel signal. A binned likelihood fit to the invariant mass of the reconstructed top quark was performed and the cross section value for the t-channel process was calculated: $\sigma_{t-channel} = 62.2 \pm 8.0(\text{stat})^{+8.6}_{-8.8}(\text{syst})$ pb which is in good agreement with the theoretically predicted value.

Finally, the response ($\text{p}_T^{reco}/\text{p}_T^{true}$) of light quark or gluon initiated jets is evaluated for both the t-channel and the Wt associated production, in order to determine the flavour composition uncertainty, as part of the framework that provides the jet energy scale uncertainties in a multiple jets environment. Other sources of systematics are also reviewed.

Acknowledgements

First and foremost I would like to thank my supervisor Steve Lloyd for his kind guidance, patiente and immense knowledge. I am very thankful for all the ideas we discussed that helped to get this PhD into shape.

A big thank you to Marcella Bona for her help during my service work at CERN. Thank you also to the SCT group for their very useful suggestions.

To the IT staff, Alex Owen and Cozmin Timis, thank you so much for your ever so prompt and efficient help with all my computer related problems (and they were so many!). To Graham Beck, thank you for the delicious carefully chosen biscuits and the chats while eating them!

Thank you to all my office collegues, who were essential in providing a cheerfull work environment! Thank you Alex Hyndman, James Poll, Katy Ellis, Tom Macey and Jack Goddard.

A special mention to Elisa Piccaro, my friend and constant company throughout all these years: thank you so much for so much, that words can barely describe. Thank you for being always here for me.

To my friends back in Portugal, always giving me support and encouragement, despite the distance, Miguel Fiolhais, Rita Coimbra and Filipa Balau, muito obrigada!

A huge thank you to my Mother and Father, for their support and excellent care as only amazing parents can do.

This great achievment would have been so much harder to go through if not for the strength my husband always and tirelessly gave me. Even when I doubted myself, you would be certain I could do it. Thank you for that. And for everything else.

Contents

List of Figures

List of Tables

Chapter 1

Introduction

This thesis presents the work done as part of my PhD degree. The main topics are the contribution towards the Semiconducter Tracker (SCT) and the analysis performed to determine the cross section of the leptonic single top t-channel.

The top quark is the least known of all the other quarks present in the Standard Model (SM). It was discovered at the Tevatron in 1995, by the CDF [1] and DØ [2] experiments and it has completed the three family structure of the SM. The top quark mass is of about 175 GeV and its charge is 2/3e. It decays quickly and almost exclusively as $t \rightarrow Wb$.

The LHC particle collider is an ideal place for studies of the top quark, due to its high energy proton collisions. These are exciting times for particle physics: the LHC has acquired more data than ever before with higher energies than ever. As of July 2012 the Higgs boson was officially discovered at a mass $M_H \sim 126$ GeV with the $gg \rightarrow H$ the dominant channel by the biggest experiments in the LHC: ATLAS [3] and CMS [4].

The single top t-channel is the dominant process in the single top production, at the LHC. Even so, the $t\bar{t}$ production is twice as probable, making the signal discrimination challenging. The data analysed in this work was acquired in 2011 and amounts to around 4.7 fb^{-1} in integrated luminosity. The statistics available is enough for a measurement on the leptonic single top t-channel cross section, which is the aim of this thesis. However, due to its signature being similar to part of the $t\bar{t}$ and to some of the W+jets background processes, there needs to be a robust selection of events.

The contents of this thesis organize as follows. This chapter gives the motivation for the work done.

Chapter 2 presents some theoretical background about the particles and interactions of the SM. Some more recent results at the LHC are presented in the top quark area: the mass and cross sections are the main ones.

Chapter 3 describes the ATLAS detector and its main components. The trigger system is briefly explained and an overview of the data acquired so far and future plans is given.

Chapter 4 is about my contribution to one of the inner detector components, the SCT. Calculations and studies towards the determination of the Lorentz angle are presented and conclusions based on the results are made.

Chapter 5 explains the steps to scale data and simulation. The method for the simulation of the QCD background based on a data-driven method is described.

Chapter 6 presents the cut based analysis of the t-channel. The objects needed to select t-channel events are defined and reconstructed when needed. After a selection of events, discriminating cuts are applied and a binned likelihood fit is performed to the invariant mass of reconstructed top events. The cross section is then extracted.

Chapter 7 shows my contribution towards a tool to determine the uncertainty associated to the jet energy scale in a multi-jet environment. Other sources of systematic uncertainties are listed, and the final cross section value with the associated uncertainty is shown. Finally on Chapter 8 conclusions on this work are made.

In this thesis the convention $\hbar = c = 1$ is used. Therefore momenta, energy and mass are given in units of GeV.

Chapter 2

Theoretical Background

In this chapter, an introduction to the Standard Model of particles is given. The properties of the top quark are presented, as well as the most recent experimental measurements. Single top quark production is explained, with a special attention to the t-channel, the object of study of this thesis.

2.1 The Standard Model

The Standard Model (SM) describes the physics of the strong and electroweak interactions and was formulated between 1960 and 1970. It is the most accepted model and has had, to this date, full experimental confirmation. The SM includes twelve fermions, the top quark being one of them. These twelve fermions are divided into leptons and quarks and the particles within each group belong to three distinct families with different masses. Besides the fermions, the SM also contains another kind of particles, the exchange bosons.

Figure 2.1 [5] is a schematic diagram representing the elementary particles of the SM: the three families of leptons and quarks and the bosons, which are the force carriers. For each charged particle, there exists an antiparticle, with opposite charge. Amongst the bosons, the photon is massless and mediates the electroweak interactions, along with the massive bosons Z, W^+ and W^-. The gluon is the mediator of the strong force. Table 2.1 presents the three families of fermions and their properties: their helicity (L=left, R=right), the charge Q, the isospin T, the third component of the weak isospin, T_3, and the hypercharge Y. These will be explained in the following sections.

The SM dynamics is determined through the Lagrangian:

$$\mathcal{L}_{SM} = \mathcal{L}_{QCD} + \mathcal{L}_{electroweak}. \tag{2.1}$$

This is a classical construction, however it determines perturbatively the cross
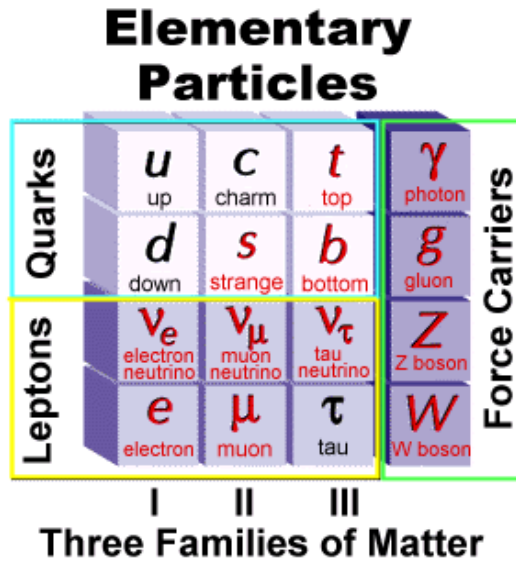
Figure 2.1: *Scheme of the particles that constitute the Standard Model, all of them experimentally observed: three families of quarks and leptons and the force carriers [5].*

sections that can be measured experimentally. These are calculated through a perturbative series on the theory couplings, represented by the Feynman diagrams. These diagrams are constructed through a set of Feynman rules that can be directly determined by the above Lagrangian. The kinetic terms of the fields give its propagators and the remaining terms describe the interactions and determine the vertices. With this set of rules it is possible to associate to each diagram an analytical expression that allows us to compute a given cross section.

2.1.1 The Electroweak Theory

Structure of the Electroweak sector

Weak and electromagnetic interactions are described by the Weinberg-Salam-Glashow model. These two forces are unified under a symmetric gauge group $SU(2)_L \times U(1)_Y$. This group acts differently on particles of different helicity (i.e. different helicity fields group themselves in distinct representations) and is a spontaneously broken symmetry. The electroweak Lagrangian can be divided into three parts:

$$\mathcal{L}_{electroweak} = \mathcal{L}_{gauge} + \mathcal{L}_{fermions} + \mathcal{L}_{Higgs}. \tag{2.2}$$

The quarks and the leptons are grouped into SU(2) representations, according to their helicity (L=left, R=right),

Family	Lepton	T	T_3	Y	Q	Quark	T	T_3	Y	Q
	$\nu_{e,L}$	$\frac{1}{2}$	$\frac{1}{2}$	-1	0	d_L	$\frac{1}{2}$	$-\frac{1}{2}$	$\frac{1}{3}$	$-\frac{1}{3}$
I	e_L	$\frac{1}{2}$	$-\frac{1}{2}$	-1	-1	u_L	$\frac{1}{2}$	$\frac{1}{2}$	$\frac{1}{3}$	$\frac{2}{3}$
	e_R	0	0	-2	-1	u_R	0	0	$\frac{4}{3}$	$\frac{2}{3}$
						d_R	0	0	$-\frac{2}{3}$	$-\frac{1}{3}$
	$\nu_{\mu,L}$	$\frac{1}{2}$	$\frac{1}{2}$	-1	0	s_L	$\frac{1}{2}$	$-\frac{1}{2}$	$\frac{1}{3}$	$-\frac{1}{3}$
II	μ_L	$\frac{1}{2}$	$-\frac{1}{2}$	-1	-1	c_L	$\frac{1}{2}$	$\frac{1}{2}$	$\frac{1}{3}$	$\frac{2}{3}$
	μ_R	0	0	-2	-1	c_R	0	0	$\frac{4}{3}$	$\frac{2}{3}$
						s_R	0	0	$-\frac{2}{3}$	$-\frac{1}{3}$
	$\nu_{\tau,L}$	$\frac{1}{2}$	$\frac{1}{2}$	-1	0	b_L	$\frac{1}{2}$	$-\frac{1}{2}$	$\frac{1}{3}$	$-\frac{1}{3}$
III	τ_L	$\frac{1}{2}$	$-\frac{1}{2}$	-1	-1	t_L	$\frac{1}{2}$	$\frac{1}{2}$	$\frac{1}{3}$	$\frac{2}{3}$
	τ_R	0	0	-2	-1	t_R	0	0	$\frac{4}{3}$	$\frac{2}{3}$
						b_R	0	0	$-\frac{2}{3}$	$-\frac{1}{3}$

Table 2.1: *Fermions of the Standard Model and their respective charges with respect to the electroweak sector $SU(2)_L \times U(1)_Y$ and to the $U(1)_Q$ groups. In terms of the strong sector, $SU(3)$, only the quarks transport colour.*

$$
\begin{cases}
\text{leptons}: & \ell_L^I \equiv \begin{pmatrix} \nu_e \\ e \end{pmatrix}_L, e_R; \quad \ell_L^{II} \equiv \begin{pmatrix} \nu_\mu \\ \mu \end{pmatrix}_L, \mu_R; \quad \ell_L^{III} \equiv \begin{pmatrix} \nu_\tau \\ \tau \end{pmatrix}_L, \tau_R; \\
\text{quarks}: & q_L^I \equiv \begin{pmatrix} u \\ d' \end{pmatrix}_L, u_R, d_R; \quad q_L^{II} \equiv \begin{pmatrix} c \\ s' \end{pmatrix}_L, c_R, s_R; \quad q_L^{III} \equiv \begin{pmatrix} t \\ b' \end{pmatrix}_L, t_R, b_R.
\end{cases}
\tag{2.3}
$$

While ℓ_L and q_L (which are doublets) rotate under $SU(2)_L$, e_R, t_R and b_R are left invariant (they are singlets of this group). Thus $SU(2)_L$ only acts on left helicity fields.

SU(2) has three generators $\{T_1, T_2, T_3\}$. Each particle multiplet is an eigenstate of $\sum T_i^2$ and T_3 (called the isospin). U(1) has one generator, Y, called the hypercharge. The particle's charge Q is related to its weak hypercharge and third component of the weak isospin (T_3) through $Q = \frac{1}{2}Y + T_3$.

The kinetic and self-coupling terms of the massless W_μ and B_μ fields are given, in its conventional form, by:

$$
\mathcal{L}_{gauge} = -\overbrace{\frac{1}{4}F_i^{\mu\nu}F_{\mu\nu}^i}^{SU(2)} - \overbrace{\frac{1}{4}B^{\mu\nu}B_{\mu\nu}}^{U(1)},
\tag{2.4}
$$

with

$$F^i_{\mu\nu} = \partial_\mu W^i_\nu - \partial_\nu W^i_\mu - g_2\epsilon^{ijk}W^j_\mu W^k_\nu, \tag{2.5}$$

$$B_{\mu\nu} = \partial_\mu B_\nu - \partial_\nu B_\mu. \tag{2.6}$$

Where $\vec{W}_\nu$ is the three-component $SU(2)$ gauge field and B_ν is the $U(1)$ gauge field. The Pauli matrices indices are represented by i, j, k, while μ and ν are the Lorentz indices. For the fermionic sector there is:

$$\mathcal{L}_{fermions} = \sum_{\psi_L} \bar{\psi}_L i\slashed{D}\psi_L + \sum_{\psi_R} \bar{\psi}_R i\slashed{D}\psi_R, \tag{2.7}$$

with

$$\mathcal{D}_\mu\psi_R = \left(\partial_\mu + \frac{i}{2}g_1 Y B_\mu\right)\psi_R, \tag{2.8}$$

$$\mathcal{D}_\mu\psi_L = \left((\partial_\mu + \frac{i}{2}g_1 Y B_\mu) + \frac{i}{2}g_2\vec{\tau}\cdot\vec{W}_\mu\right)\psi_L, \tag{2.9}$$

where $\psi_{L,R}$ are the fermion fields, g_1 and g_2 are the electroweak couplings (associated to the gauge field U(1)$_Y$ and SU(2)$_L$, respectively), $\slashed{D} = \gamma^\mu \mathcal{D}_\mu$, γ^μ the gamma matrices, ϵ^{ijk} the Levi-Civita symbol and $\vec{\tau}$ the Pauli matrices.

Note that there is no mass term in the above expressions. To do this in a gauge invariant way, which means remaining unchanged due to a local transformation of the type $\phi(x) \rightarrow e^{i\alpha(x)}\phi(x)$ ($\alpha(x)$ is a function that depends on space and time in an arbitrary manner), a mechanism in order to break the $SU(2)$ symmetry and a scalar particle called the Higgs boson are introduced.

2.1.2   QCD

The sector of the SM that describes the strong interactions is named Quantum Chromodynamics (QCD) and is identified by the existence of local non-abelian SU(3) symmetry (of colour). The fields that describe the quarks $\psi^{(\alpha)} = (\psi_j^{(\alpha)})$, where α is the flavour index, are found in the fundamental representation of that group: they transport colour and $j = 1, 2, 3$. In order for the theory to become invariant, it is necessary to introduce a standard, non-Abelian (the symmetry group is non-commutative) field, A^a_μ, in which a is the colour index. The field is written in the joint representation of the group: $a = 1, \ldots, 8$. The field's quanta are the eight gluons. The Lagrangian for this sector then takes the form:

$$\mathcal{L}_{QCD} = -\frac{1}{4}F^{\mu\nu}_a F^a_{\mu\nu} + \sum_\alpha \bar{\psi}_j^{(\alpha)}(i\slashed{D}_{jk} - m^{(\alpha)}\delta_{jk})\psi_k^{(\alpha)}, \tag{2.10}$$

with

$$F_{\mu\nu}^a = \partial_\mu A_\nu^a - \partial_\nu A_\mu^a - g_3 f^{abc} A_\mu^b A_\nu^c, \qquad (2.11)$$

with g_3 the theory coupling, $m^{(\alpha)}$ the quark masses obtained from the electroweak sector by spontaneous symmetry breaking, f^{abc} the SU(3) structure constants and A_μ^a are the gluon fields. $\mathcal{D}_\mu$ is simply the covariant derivative with respect to A_μ^a,

$$\mathcal{D}_\mu \psi = \left(\partial_\mu + i g_3 A_\mu^a \frac{\lambda_a}{2} \right) \psi, \qquad (2.12)$$

where λ_a are the Gell-Mann matrices.

By applying Equations 2.11 and 2.12 into Equation 2.10, the kinetic terms that define the Feynman propagators can be determined along with the interaction terms that are given by the vertices in the Feynmen rules.

CKM Matrix

The Cabibbo-Kobayashi-Maskawa (CKM) matrix is unitary and contains information about couplings with the exchange of flavour and allows for interactions between different family quarks to happen. It is [6]:

$$V \equiv \begin{pmatrix} V_{ud} & V_{us} & V_{ub} \\ V_{cd} & V_{cs} & V_{cb} \\ V_{td} & V_{ts} & V_{tb} \end{pmatrix}$$

$$= \begin{pmatrix} 0.97427 \pm 0.00015 & 0.22534 \pm 0.00065 & 0.00351^{+0.00015}_{-0.00014} \\ 0.22520 \pm 0.00065 & 0.97344 \pm 0.00016 & 0.0412^{+0.0011}_{-0.0005} \\ 0.00867^{+0.00029}_{-0.00031} & 0.0412^{+0.0011}_{-0.0005} & 0.999146^{+0.000021}_{-0.000046}. \end{pmatrix} \qquad (2.13)$$

This is a numerical matrix, determined experimentally and by using the unitarity requirement. The CKM matrix determines the currents that change the flavour of the quarks and these currents in its turn determine the vertices of interactions of the type $q_1 \rightarrow q_2 W^\pm$, where a quark q changes flavour by emitting a charged gauge boson. One can then interpret the CKM matrix as an indication of how favourable a certain decay with a change of flavour is.

For example, the vertex of the decay $t \rightarrow Wb$ is proportional to $V_{tb} = 0.999146$, whereas $t \rightarrow Wd$ is proportional to $V_{td} = 0.00867$. The decay probabilities, are, as a first approximation, proportional to V_{tb}^2 and V_{td}^2. As $V_{td} << V_{tb}$, t decaying into b is much more probable. Higher order corrections in powers of V_{tb} and V_{td} favour this decay even more.

Parton Distribution Functions

The protons can be treated as a set of partons (quarks and gluons) and its components can be described by structure functions. Within this parton model context, the calculation of production cross-sections at hadron colliders depends on the knowledge of Parton Distribution Functions (PDF). The PDFs express the probability for a parton i inside the proton to carry a fraction x of the proton's momentum. This distribution is described as a function of the squared momentum transfer Q^2 carried by the exchanged particle in the scattering process. The PDFs cannot be calculated perturbatively, thus being evaluated through the measurement of deep-inelastic scattering and jet production at colliders and extrapolated with the DGLAP[1] evolution equations[7, 8, 9, 10]. The DGLAP equations are a matrix equation of dimension $(2n_f + 1)$ where n_f is the number of quark and anti-quark flavour that contribute. In particular, the ZEUS and H1 experiments at HERA[11, 12] have performed fits to the data acquired by HERA to extract parton distributions at low x, which is a region dominated by gluons. Figure 2.2 shows the PDFs evaluated by the CTEQ Collaboration that include data from experiments at HERA and Tevatron [13].

2.2   The Top Quark

The top quark belongs to the third family of quarks, according to the SM. It has spin $\frac{1}{2}$ and an electric charge of $\frac{2}{3}$ times the electron charge. As it is a quark, it transforms as a triplet according to the SU(3) group, responsible for the strong force and forms, together with the b quark, a doublet according to SU(2)$_L$ from the electroweak sector.

The top quark is very massive, nearly 35 times the mass of the b quark, positioning it close to the electroweak symmetry breaking scale. With such high mass and since the V$_{tb}$ element in the CKM matrix is greater than both V$_{td}$ and V$_{ts}$ and very close to unity, the top quarks decays mainly as $t \rightarrow Wb$.

The width predicted by the SM is, at next-to-leading order, NLO, and neglecting the second order terms m_b^2/m_t^2, α_s^2 and $(\alpha_s/\pi)M_W^2/m_t^2$ [6]:

$$\Gamma_{NLO}(t \rightarrow Wb) = \frac{G_F m_t^3}{8\pi\sqrt{2}} \left(1 - \frac{M_W^2}{m_t^2}\right)^2 \left(1 + 2\frac{M_W^2}{m_t^2}\right) [1 - \frac{2\alpha_s}{3\pi}\left(\frac{2\pi^2}{3} - \frac{5}{2}\right)], \quad (2.14)$$

where M_W and m_t are the mass of the W boson and the top quark respectively, and $\alpha_s(M_Z)$ the strong coupling constant. The width for a mass of $m_t = 171$ GeV, based on the world average, and $\alpha_s(M_Z) = 0.118$ is 1.29 GeV and increases with the mass.

---

[1]DGLAP stands for Dokshitzer-Gribov-Lipatov-Altarelli-Parisi
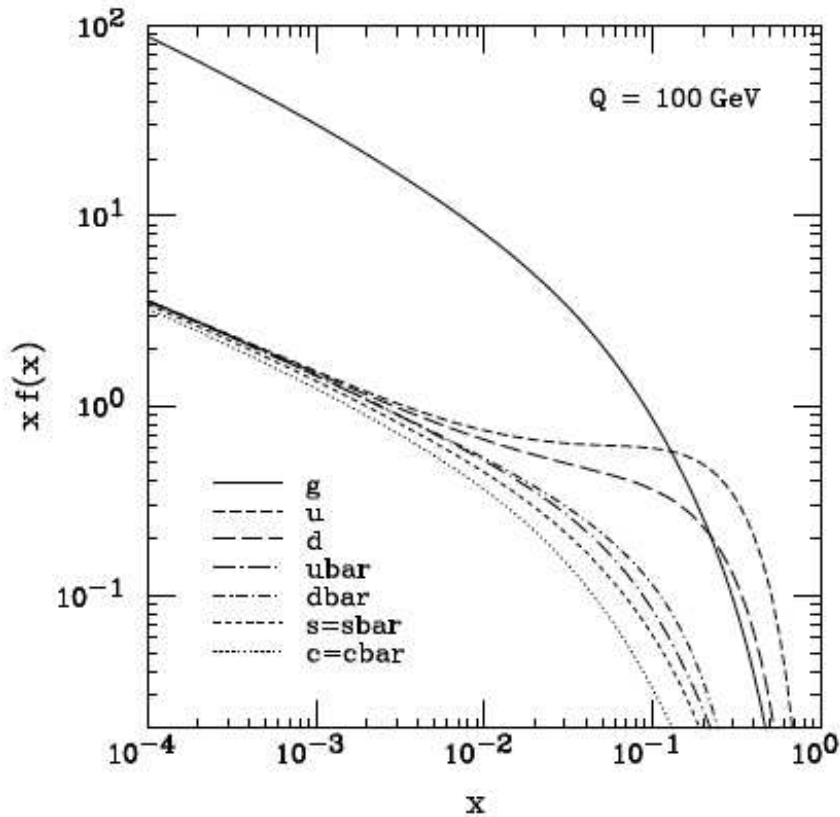
Figure 2.2: *Parton Distribution Functions for Q = 100 GeV, evaluated by the CTEQ Collaboration, (CTEQ 6M) [13].*

The top quark's lifetime is very small, $\sim 0.5 \times 10^{-24}$ s and so it decays before hadronizing, and therefore any spin information is preserved by the decay products.

Due to all these properties, the top quark has been extensively studied by particle colliders. It was the last quark to be observed, in 1995, by the Tevatron, at the Fermilab laboratory, by the CDF [1] and DØ [2] experiments. The Tevatron was a proton-anti-proton collider, in operation between 1983 and 2011 and measured most of the top quark properties, such as mass, top pair and single top productions cross sections and kinematics. The latest Tevatron results are with a centre of mass energy of $\sqrt{s} = 1.96$ TeV and it has acquired up to 10 fb^{-1} [14] of data.

Due to the differences of the energy of the centre of mass, between the Tevatron and the LHC, the cross sections will be considerably different, and some physics processes that were very hard to detect at the Tevatron, are easier to measure in ATLAS. Figure 2.3 shows the different processes' cross sections measured at the Tevatron and predicted at the LHC [15].
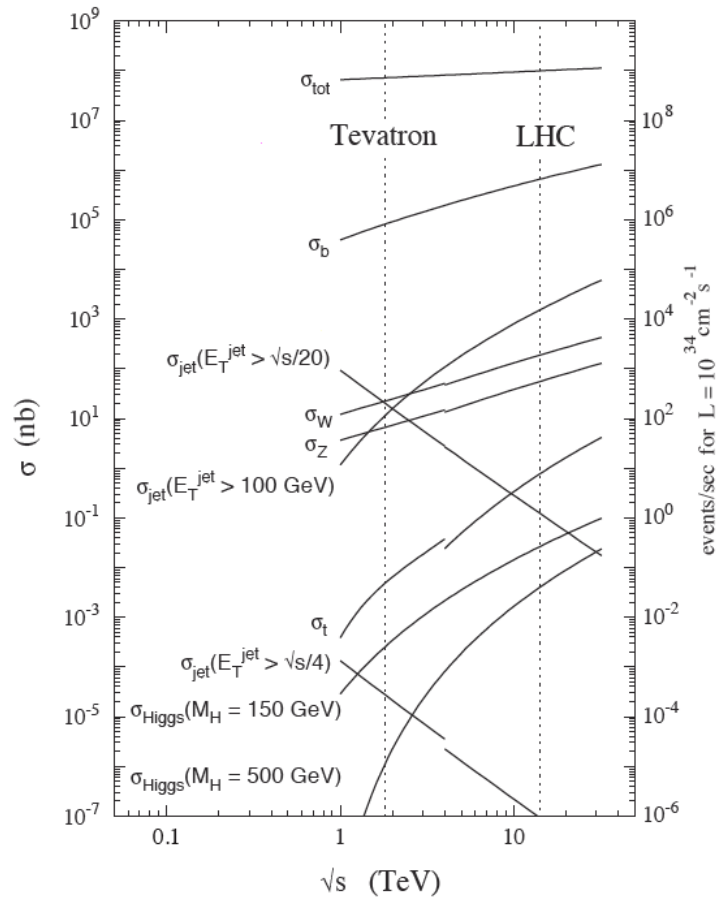
Figure 2.3: *Cross sections of the different physics processes at the Tevatron and the LHC as a function of the centre of mass energy ($\sqrt{s}$) [15].*

2.2.1   Production of the Top Quark

Top quarks are produced mainly in pairs through quark pair or gluon fusion: $q\bar{q} \rightarrow t\bar{t}$ or $gg \rightarrow t\bar{t}$. At the Tevatron 85% of the top quark pairs are produced from $q\bar{q}$ annihilation, whereas at the LHCgluon-gluon fusion is the dominant way of producing top pairs, creating about 90% for $\sqrt{s} = 14$ TeV (the design LHC centre of mass energy) and 80% for a $\sqrt{s} = 7$ TeV. Figure 2.4 shows the Feynman diagrams for $t\bar{t}$ production.

The NNLO cross section for the top pair at the Tevatron ($\sqrt{s} = 1.96$ TeV) is $\sigma_{t\bar{t}} = 7.93 \pm 0.36$ pb for $m_t = 173$ GeV, whereas for LHC ($\sqrt{s} = 7$ TeV) it is $\sigma_{t\bar{t}} = 165^{+10}_{-11}$ pb [16].

In this process, almost all the time, both t and $\bar{t}$ decay to a W boson and a b quark. But the W can decay into quark pairs or into a charged lepton and a neutrino. Therefore, the final states for the top pair production are divided into three sub-processes:
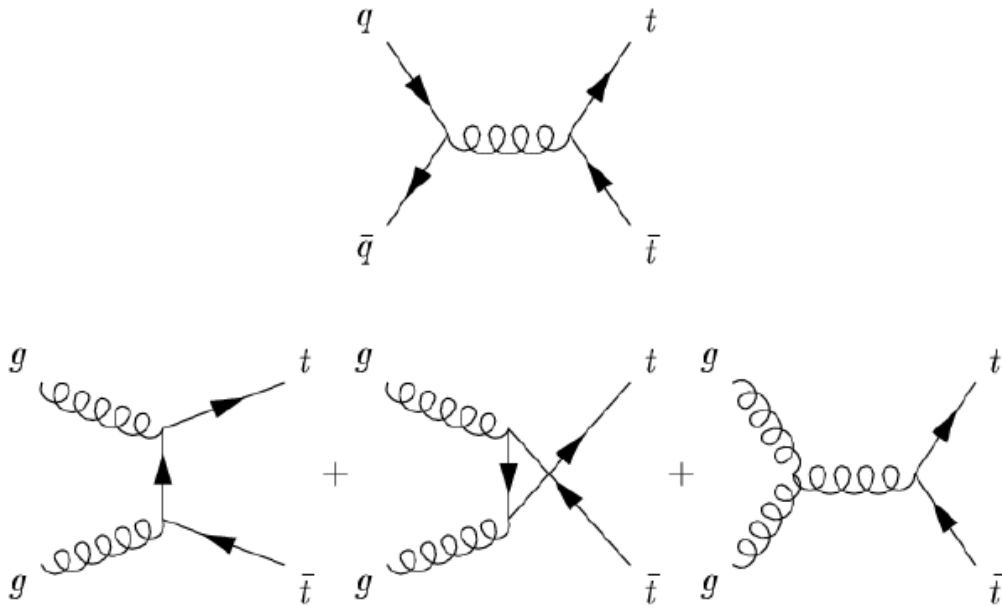
Figure 2.4: *The leading order Feynman diagrams for the $t\bar{t}$ process. The gluon fusion diagrams (bottom) dominate over the $q\bar{q}$ diagram (top) at the LHC.*

- all hadronic - $t\bar{t} \rightarrow W^+bW^-b \rightarrow q\bar{q}'b + q''\bar{q}'''\bar{b}$ (45.7%);

- lepton+jets - $t\bar{t} \rightarrow W^+bW^-b \rightarrow q\bar{q}'b\ell^-\bar{\nu}\bar{b} + \ell^+\nu bq''\bar{q}'''\bar{b}$ (43.8%);

- dilepton - $t\bar{t} \rightarrow W^+bW^-b \rightarrow \ell^+\nu b + \ell^-\nu\bar{b}$ (10.5%);

where ℓ can be any charged lepton, electron, muon or tau.

Top quarks can also be created by electroweak single top mechanisms, such as $q\bar{q} \rightarrow t\bar{b}$ and $qb \rightarrow q't$. These mechanisms have a smaller cross section and are divided into three channels: t-channel, with the exchange of a virtual W boson, s-channel with the decay of a virtual W boson and the associated production of a top quark and a W boson. The Tevatron was able to observe the single top mechanism, via the t-channel and s-channel, but observation of the associated production was not possible due to its very small cross section. In $p\bar{p}$ collisions at the Tevatron, the production cross section for a top is the same as for an anti-top, however that is not the case for the LHC. These three channels are presented in more details in the following sections.

2.2.2   Top Quark measurements at the LHC

The LHC, in operation since 2009, has already provided accurate studies of the top quark. With $\sqrt{s} = 7$ TeV (8 TeV in 2012) and a recorded integrated luminosity of

5 fb^{-1} (20 fb^{-1} in 2012), already exceeding that from the Tevatron, 10 fb^{-1}.

The mass of the top quark has been measured mainly through the production of top quark pairs by all the capable experiments. Figure 2.5 presents the latest (as of July 2012) measurements and combined values, in the Tevatron and the LHC [17].
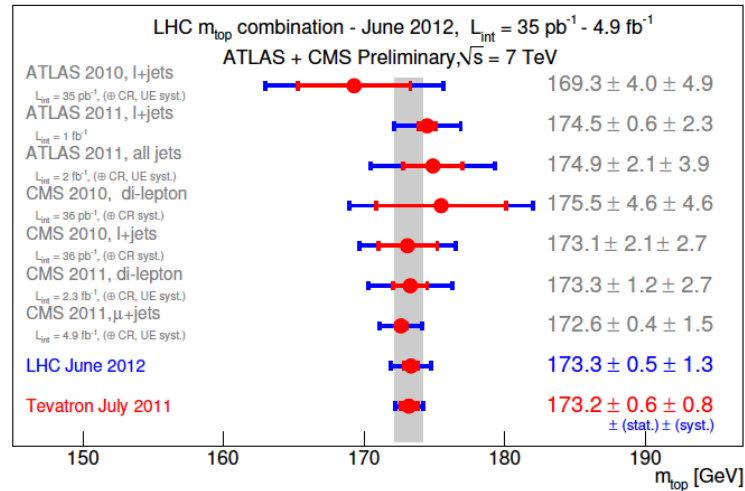
Figure 2.5: *Combined values of the top quark mass, measured by the experiments at CDF and DØ at the Tevatron and by ATLAS and CMS at the LHC [18].*

Besides the mass, a number of properties are currently under study at the LHC. Right from the beginning of its operation with proton collisions, both ATLAS and CMS have had access to a number of top quarks candidates created and had the ability to determine with an increasingly better precision the cross section of the top quark pairs ($173.3 \pm 2.3_{stat} \pm 9.8_{syst}$ pb [19]), the top charge, where the exotic quark charge of $-\frac{4}{3}|e|$ was excluded [20], and other properties of the quark top, such as $t\bar{t}$ spin correlations, charge asymmetries and also properties related to the t-W-b decay vertex, such as the helicity of the W bosons originating from the top decay (all these properties compiled in [6]).

2.3 Single Top Quark Production

The production of a single top quark was officially observed in 2009, by DØ [21] and CDF [22] based on analyses counting events of t-channel and s-channel combined. Single top quark production is sensitive to the parton distribution function (PDF) of the light quarks in the proton. As mentioned before, there are three different single top mechanisms:

- **t-channel:** also called 'W-gluon fusion', this is the dominant mechanism for the single top production. It is characterised by the exchange of a virtual W
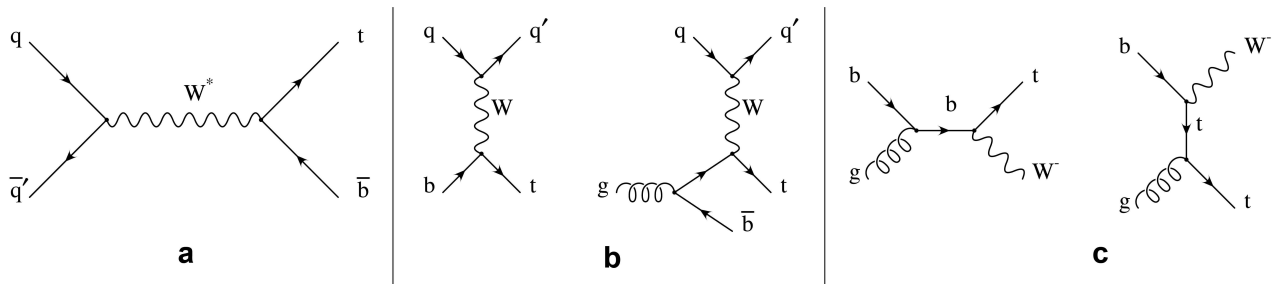
Figure 2.6: *Feynman diagrams of the single top production: (a) the s-channel, (b) t-channel and (c) Wt associated production.*

boson. The final state has a W boson decaying into a lepton plus a neutrino and a quark;

- **s-channel:** is the least probable mechanism, involving the decay of a virtual W boson into a t and a $\bar{b}$. In the final state there are two b quarks, the other one comes from the top decay and a W which can decay into a charged lepton and a neutrino.

- **Wt production:** involves the associated production of a real W boson. The final state has two W bosons, either one decaying leptonically (lepton and neutrino) and other hadronically (quark pair) or both leptonically;

Figure 2.6 shows the Feynman diagrams of the three single top mechanisms: (a) s-channel, (b) t-channel and (c) Wt associated production. The expected next-to-next-to-leading order (NNLO) cross sections of each process are presented in Table 2.2 [23, 24, 25].

Process	σ [pb]
t-channel	$64.2^{+1.8}_{-1.1}$
s-channel	4.6 ± 0.3
Wt	15.6 ± 1.2

Table 2.2: *Expected NNLO cross sections for the three single top production mechanisms at the LHC, at $\sqrt{s} = 7$ TeV, for $m_t = 173$ GeV.*

Table 2.2 indicates the expected cross sections of the single top mechanisms at the LHC, with $\sqrt{s} = 7$ TeV, for a $m_t = 173$ GeV. At the Tevatron, the t-channel and the s-channel cross sections were first measured combined, and the measured cross section for the two processes is $\sigma_{s+t} = 2.76^{+0.58}_{-0.47}$ pb, for a $m_t = 170$ GeV [26].

The single top cross section is proportional to $|V_{tb}|^2$, providing the only direct measurement of V_{tb} without having to rely on the number of quark generations.

Single top production is a very interesting channel of study, because it poses an important background to Higgs production (for example with ttH production) and may be relevant to new physics searches, such as anomalous couplings, a fourth quark generation, FCNC (production of a single top via flavour-changing neutral-currents) and charged Higgs production.

Experimentally, the observation of single top quark production is somewhat challenging, not only because of the relatively small cross sections (the $t\bar{t}$ cross section is twice the t-channel one), but mainly because the signature of such processes is not completely distinctive, as it is very similar to one branch of the $t\bar{t}$ and has large backgrounds composed mainly of W+jets processes and $t\bar{t}$.

At the Tevatron, the discovery of the single top quark was through the combination of the t-channel and the s-channel as signal. The Wt production channel was very hard to detect there.

At the LHC, as for the Tevatron, the t-channel is the dominant one, however the least probable one is the s-channel. In Figure 2.7 one can see the relative amount of each channel, for the Tevatron (left) and for the LHC (right).
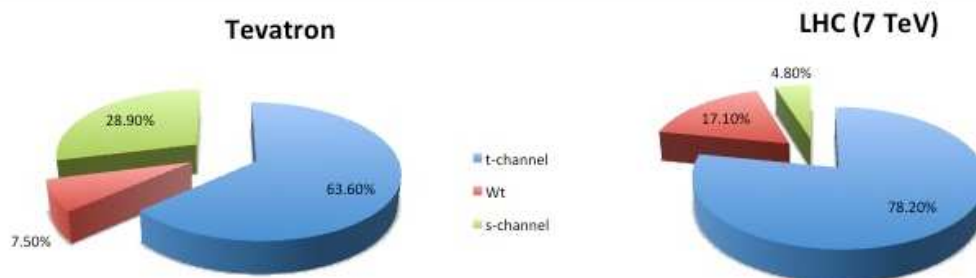
Figure 2.7: *The relative amount of each of the three single top channels for the Tevatron (left) and for the LHC (right).*

2.3.1 t-channel

Measurement of the t-channel is the goal of study of this thesis. It is the dominant channel in the single top production. Experimentally, the way to look for this signal is to detect the final state products and try to reconstruct the channel considered.

The top quark almost always decays into a W boson and a b quark. The W can decay into a charged lepton and a neutrino. The lepton can be an electron e , muon μ or a tau τ, however the τ decays leptonically or into a combination of

mesons, making it a complex particle to reconstruct, so only the cases when the W decays to an e or a μ are considered. Figure 2.8 on the left shows the diagram of the production and decay of the top. On the right is a representation of the experimental signature of the t-channel: the lepton and the neutrino and the quarks, represented here as jets.
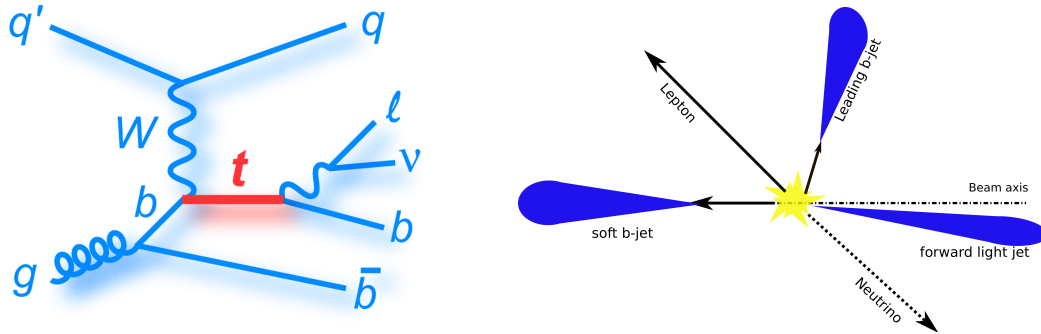
Figure 2.8: *Diagram of the t-channel production and decay (left) and the experimental signature of the t-channel (right).*

Jets are the experimental manifestation of quarks in the detector, which sees a quark or anti-quark as a shower of hadronized particles within a defined area of energy. So the final state has the b-jet from the top decay, the light jet from the top production and a second b-jet, that is very soft and emitted at very low angle, thus escaping detection by the ATLAS detector. This b-jet is normally ignored in the selection.

The latest published result for the t-channel in ATLAS is with a total integrated luminosity of $1.04\,\text{fb}^{-1}$ which corresponds to data acquired between March and June 2011 [27]. The cross section for the t-channel has been measured by selecting events with two or three jets, one of them tagged as a b-jet, a charged lepton being an electron or a muon and a large quantity of missing transverse energy (representing the neutrino that cannot be fully detected in ATLAS).

The method applied for the determination of the cross section involves a set of selection requirements in order to best isolate the signal and afterwards, because the signal is still difficult to distinguish between the background, a multivariate discriminant constructed with a Neural Network is applied. The V_{tb} component can also be determined, since $|V_{tb}|^2$ is proportional to the cross section, so one of the first results for the t-channel in ATLAS is:

$$\sigma_t = 83 \pm 4\,(\text{stat})^{+20}_{-19}\,(\text{syst})\,\text{pb},$$
$$|V_{tb}| = 1.13^{+0.14}_{-0.13},\ \ |V_{tb}| > 0.75,\ 95\%\,\text{CL}.$$

The background for the t-channel signal needs to be well studied, taking into account Monte Carlo simulation of both the signal and the expected background, based on the current theory models, and afterwards needs to be modelled to the actual detector and the real data. The better knowledge one has of the detector, the more precise is the measurement.

Since LHC has started operation recently, most measurements are still dominated by the systematic errors, as can be seen in the following measurements. Figure 2.9 shows the most recent measurements of the Single Top processes cross sections in ATLAS.
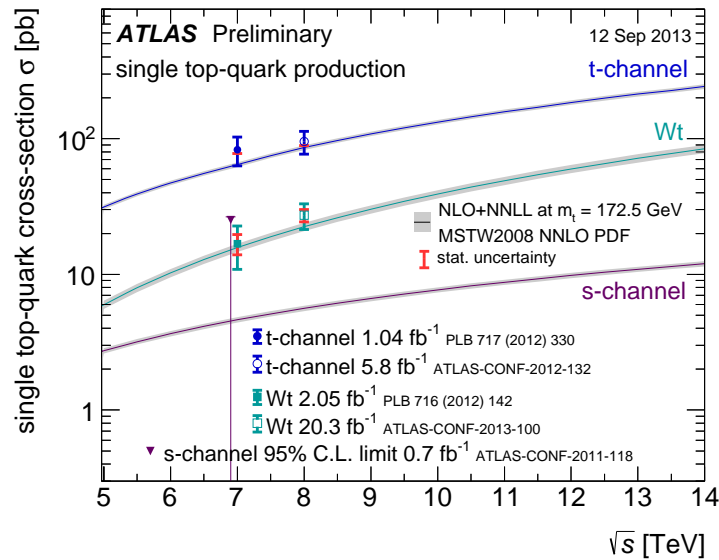
Figure 2.9: *Measurements of the single top processes cross sections in ATLAS as a function of the centre of mass energy compared to the theoretical calculation based on NLO QCD complemented with NNLL resummation. Only an upper limit is shown for the s-channel [28].*

Chapter 3

The ATLAS Detector

In this chapter, the ATLAS detector is described. ATLAS, *A large Toroidal LHC ApparatuS*, is a multi purpose particle detector, of cylindrical shape with several sub systems to detect the various particles involved. It is one of the four main experiments of the Large Hadron Collider (LHC), part of the CERN laboratory, based in Geneva, Switzerland. The LHC will be briefly described in this chapter, and attention will be given to each of the sub detectors in ATLAS.

3.1 CERN

CERN, European Organization for Nuclear Research is one of the largest particle physics research centres in the world. Its goal is as complex as the laboratory itself: to understand the elementary world of the particles, achieving a knowledge of the Universe and its creation.

CERN was founded in 1954 and nowadays it includes collaboration with more than 20 countries.

3.1.1 The discoveries

Since the beginning of its existence, CERN has been providing a number of discoveries and breakthroughs, not only in physics, but in several fields, including medical instrumentation, computing and electronics. Here are only a few of the many discoveries made at CERN, throughout the times:

- In 1968 Georges Charpak developed the multi-wire proportional chamber, a gas-filled box with parallel detecting wires connected to amplifiers, which pass the information to a computer. This type of chambers is still used in detectors for the tracking system;

- In 1973, neutral currents are confirmed in a Gargamelle bubble chamber experiment, by observing that neutrinos could interact with particles in a target without producing charged leptons;

- 1983 was the year the bosons W and Z were discovered in proton-anti-proton collisions;

- In 1990 the World Wide Web (WWW) was created to meet the demand for information sharing between scientists all over the world;

- In 1995 anti-hydrogen atoms were created for the first time;

- In 2000 it was announced the discovery of a state of matter twenty times denser than the nuclear one, in which the quarks, instead of forming protons or neutrons, are free. This state is called quark-gluon plasma.

- In July 2012, ATLAS and CMS (Compact Muon Solenoid), the two multi-purpose experiments, announced the discovery of a new particle consistent with the Standard Model Higgs boson, thus approaching the completion of such model.

3.2 LHC

The LHC is a particle accelerator and collider of beams of protons (or heavy-ions), constructed in a circular 26.7 Km tunnel, the same tunnel used for the previous experiment, LEP.

Figure 3.1 is a representation of the LHC, where the main experiments can be observed: ATLAS, CMS (the two multi purpose detectors), ALICE (used for heavy-ion physics) and LHCb (B-physics). Along the 26.7 Km accelerator, there are four collision points of the two beams, one for each experiment. Dividing the LHC into eight octants, ATLAS is situated in the first octant, between ALICE and LHCb and CMS is right opposite, on the fifth octant.

Table 3.1 shows some quantities relevant to the LHC [30].

3.2.1 Luminosity in the LHC

The aim of the LHC is to reveal physics beyond the known Standard Model, with collisions of protons of design centre of mass energy up to 14 TeV. The number of events generated per second is given by [31]:

$$N_{event} = L\sigma_{event}, \tag{3.1}$$
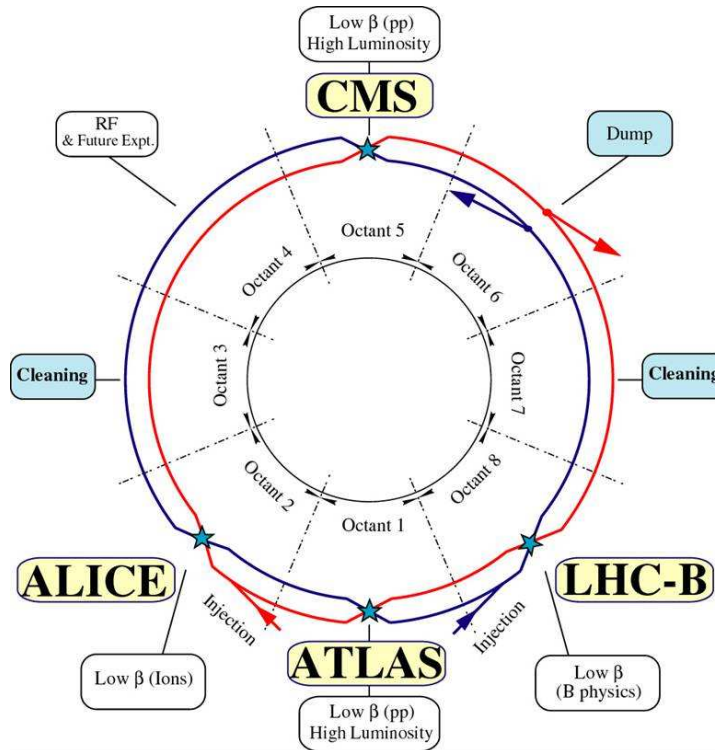
Figure 3.1: *Scheme of the LHC, divided in eight octants [29]. The collision points and the main experiments can also be seen. Beam 1 (showed in red) circulates clockwise, whereas Beam 2 (showed in blue) circulates counter-clockwise.*

where σ_{event} is the cross section[1] of that event considered and L the luminosity of the machine, given by:

$$L = \frac{N_b^2 n_b f_{rev} \gamma_r}{4\pi \epsilon_n \beta^\star} F, \tag{3.2}$$

where N_b is the number of particles per bunch, n_b is the number of bunches per beam, f_{rev} the revolution frequency, γ_r is the Lorentz factor $\left(\gamma_r = \frac{1}{\sqrt{1-\frac{v^2}{c^2}}}\right)$, ϵ_n is the normalized transverse beam emittance, $\beta^\star$ is the beta function at the collision point and F is the geometric luminosity reduction factor due to the crossing angle at the interaction point (IP):

$$F = \left(1 + \frac{\theta_c \sigma_z}{2\sigma^\star}^2\right)^{-1/2}, \tag{3.3}$$

where θ_c is the full crossing angle at the IP, σ_z is the RMS bunch length and $\sigma^\star$ is the transverse RMS beam size at the IP. The previous expression assumes round beams, $\sigma_z << \beta$ and equal parameters for both beams.

---

[1]The cross section of an interaction is a measure of the likelihood of a specific process to occur and is quantified as an effective area.

Quantity	number
Circumference	26 659 m
Dipole operating temperature	1.9 K
Number of magnets	9593
Number of main dipoles	1232
Number of main quadrupoles	392
Number of RF cavities	8 per beam
Design energy, protons	14 TeV
Operation energy, protons	7 TeV (2009-2011), 8 TeV (2012-onwards)
Nominal energy, ions	2.76 TeV/u (energy per nucleon)
Peak magnetic dipole field	8.33 T
Min. distance between bunches	$\sim$7 m
Design luminosity	10^{34} cm^{-2} s^{-1}
No. of bunches per proton beam	2808
No. of protons per bunch (at start)	1.1×10^{11}
Number of turns per second	11 245
Number of collisions per second	600 million

Table 3.1: *Some interesting design LHC parameters [30].*

Therefore, when exploring rare events, both a high beam energy and a high beam intensity are required [31].

3.3 ATLAS

ATLAS is a general purpose particle detector, that is designed to focus on the measurement of the broadest possible range of signals.

The detector is of cylindrical shape, with various sub-detectors: from the centre there is the inner detector, which identifies electrons and measures the momenta of charged particles, including leptons. Through secondary vertex reconstruction, it is also where jets are associated to heavy flavour quarks. After the inner detector there is the calorimeter system, composed of the electromagnetic (EM) calorimeter which identifies electrons and photons, the hadronic calorimeter which measures the energy deposition of hadrons, such as protons, neutrons, pions and kaons and the forward calorimeter which detects jets at very small angles. Neutrinos are inferred from the overral missing energy and momentum. Finally in the outer layer, there is the muon spectrometer (MS), to detect and measure the momenta of muons.

Figure 3.2 shows the ATLAS detector, with its main parts in evidence. ATLAS
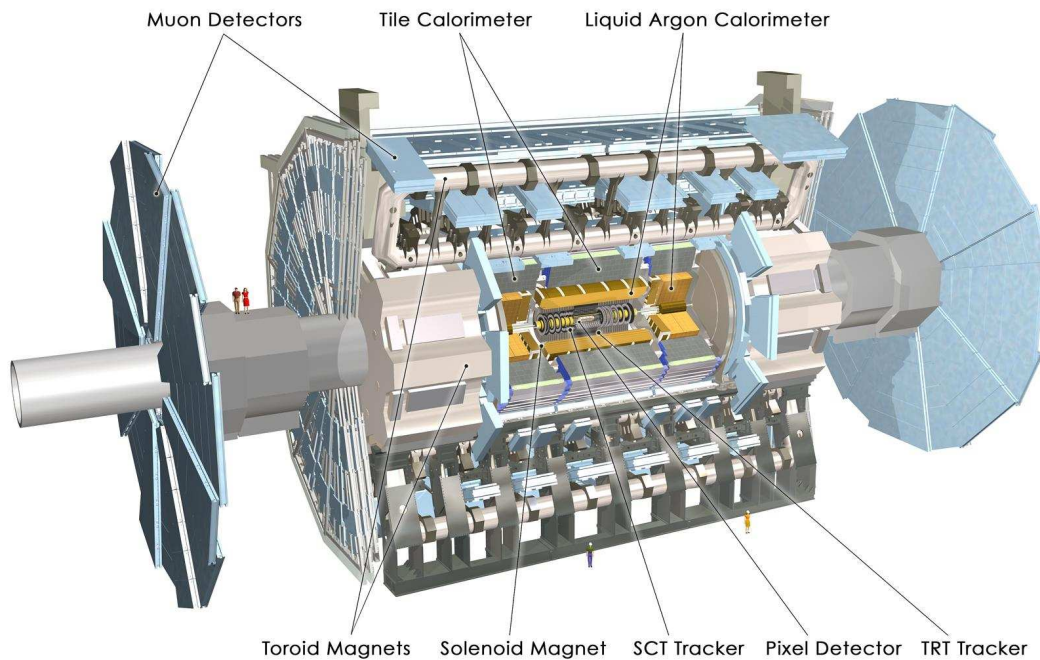
Figure 3.2: *Computer generated image of the ATLAS detector [29]. People can be seen on the left side, as scale.*

is about 45 m long and 25 m high, and weighs about 7000 tons. It is roughly the size of a 7-storey building. It is a very big collaboration of around 3000 physicists and engineers from 38 countries around the world.

In subsequent sections, more details will be given for each of the subdetectors.

3.3.1   Main Requirements

With the unprecedented amount of luminosity and energy being reached at the LHC, ATLAS will be able to observe new phenomena at the TeV scale.

The main objective is the search for the Standard Model Higgs boson, H. The predominant decay mode would be to hadrons, which is a very difficult channel to assess, due to the large amount of QCD background in the detector. The two-photon decay mode is very important. One can also consider the associated production of H, through $t\bar{t}H$, WH, ZH with $H \rightarrow b\bar{b}$.

Besides the H searches, in masses up to 6 TeV, new heavy W' and Z' would also be accessible in ATLAS. There are also searches for flavour changing neutral currents and lepton flavour violation through decays such as $\tau \rightarrow 3\mu$ or $\tau \rightarrow \mu\gamma$.

Furthermore, it is possible to search for super-symmetric particles such as squarks and gluinos, by measuring a large amount of missing transverse energy in the detector.

Here are the main requirements for such ambitious physics goals [29]:

- Close to full azimuthal angle (ϕ) coverage and large acceptance in pseudorapidity (η) are required;

- The electronics and sensors of the several sub-detectors need to be fast and radiation-hard. Also, a high granularity ($\eta \times \phi$) is necessary, in order to deal with the particle fluxes and being able to reduce the influence of overlapping events;

- In order to tag τ leptons and b jets by observing secondary vertices, vertex reconstruction detectors need to be near the interaction point;

- For the electron and photon identification and measurements, a very good electromagnetic calorimeter is necessary. In addition, a full coverage hadronic calorimeter for jets and missing transverse energy measurements is needed to complete the calorimeter system;

- Excellent muon identification and momentum resolution, from a low to high p_T range, and an unambiguous high p_T muon charge determination;

- In order to achieve a reasonable trigger rate, a high efficiency triggering on low momentum objects with sufficient background rejection is necessary.

3.3.2 Coordinate System

The ATLAS coordinate system is defined such that the beam direction defines the z axis. The collisions point is the origin of the coordinate system. The positive x axis points towards the centre of the LHC circumference and the positive y axis direction is upwards. The x-y plane is transverse to the beam direction. The transverse momentum, p_T and energy E_T are defined in such x-y plane. Figure 3.3 (a) represents the Cartesian axis system in ATLAS.

In spherical coordinates, the azimuthal angle ϕ is the angle around the beam axis. The polar angle θ is the one measured from the beam axis. A quantity widely used in ATLAS is the pseudorapidity, η, defined as:

$$\eta = -\ln \tan\left(\frac{\theta}{2}\right).$$

In Figure 3.3 (b), η as a function of ϕ is shown, for angles between 0 and π radians.

The distance in the pseudorapidity-azimuthal angle space, ΔR is also used, which translates into a cone around an object and is given by:

(a)   (b)
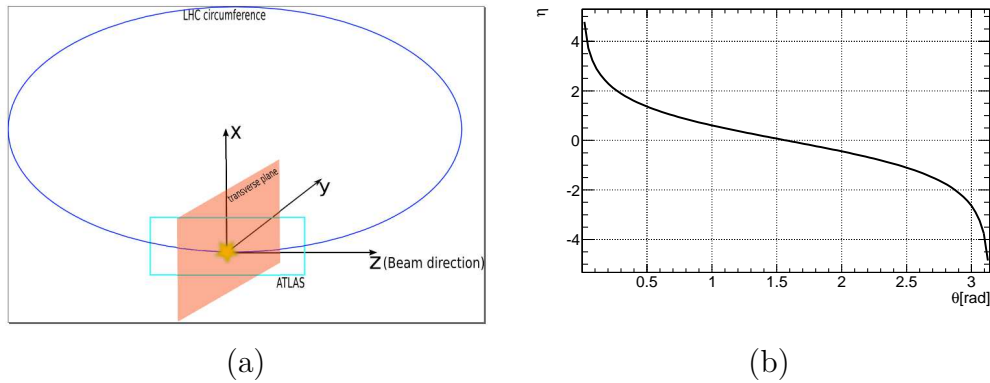
Figure 3.3: *(a) Non scale schematics of the ATLAS coordinate system; (b) η as a function of θ.*

$$\Delta R = \sqrt{(\Delta\eta)^2 + (\Delta\phi)^2}.$$

The design resolutions and $|\eta|$ coverage for each of the subdetectors are presented in Table 3.2 [29].

Components	Resolution	η	*Trigger* (η)
Tracking	$\frac{\sigma_{p_T}}{p_T} = 0.05\%p_T \oplus 1\%$	±2.5	
EM Calorimetry	$\frac{\sigma_E}{E} = 10\%/\sqrt{E} \oplus 0.7\%$	±3.2	±2.5
Hadronic Calorimetry (jets)			
Barrel and Endcap	$\frac{\sigma_E}{E} = 50\%/\sqrt{E} \oplus 3\%$	±3.2	±3.2
Forward	$\frac{\sigma_E}{E} = 100\%/\sqrt{E} \oplus 10\%$	$3.1 < |\eta| < 4.9$	$3.1 < |\eta| < 4.9$
Muon Spectrometer	$\frac{\sigma_{p_T}}{p_T} = 10\%$ at p_T=1 TeV	±2.7	±2.4

Table 3.2: *General resolutions and $|\eta|$ coverage of the ATLAS sub-detectors [29].*

3.3.3 Inner Detector

The Inner Detector (ID) is, as the name indicates, in the inner-most layer of AT-LAS. In Figure 3.4, the ID is represented. It consists of three independent but complementary systems for the tracking of charged particles: the Pixel detector, the *Semiconductor Tracker* (SCT) and the *Transition Radiation Tracker* (TRT).

The ID is 6.2 m long and has a maximum diameter of 2.1 m. It is surrounded by a 2 T magnetic field generated by the central solenoid. Both Pixels and the SCT cover the region $|\eta| < 2.5$. The goal is to provide a hermetic and robust pattern recognition, excellent momentum resolution and the ability to measure both primary and secondary vertices of charged tracks with a minimum p_T as low as 0.5 GeV.
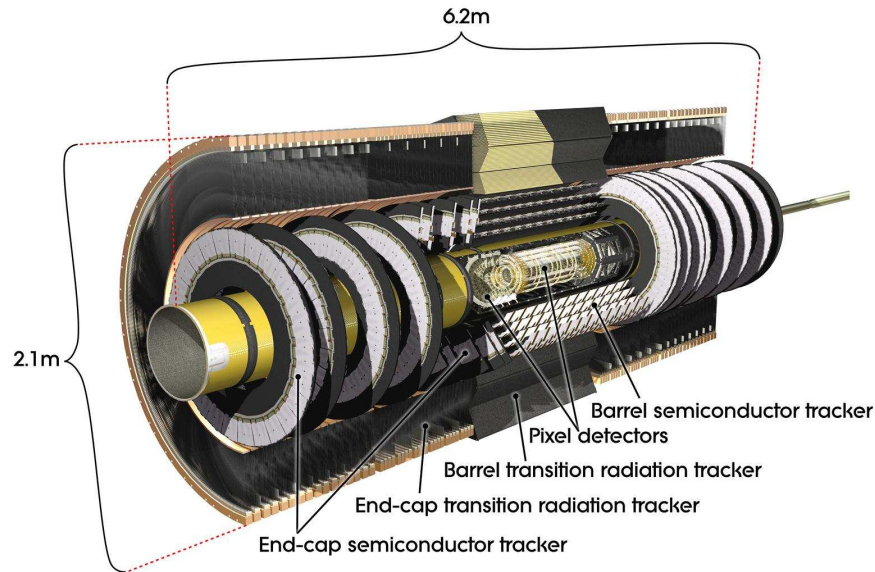
Figure 3.4: *View of the Inner Detector [29]. The innermost layer is the Pixels system, followed by the SCT and the TRT.*

Particles traversing the ID interact with the material which causes energy loss and deviation from the trajectory. Because the main requirement of the ID is the precise reconstruction of particles' trajectories, the material in the ID needs to be as minimum as possible. Figure 3.5 shows the amount of material expressed in number of radiation length, $X0^2$, averaged over ϕ as a function of $|\eta|$ separated by the contribution of each sub-detector and the various services (area in red) required to operate the ID.

Pixel

The Pixel system is the one closest to the IP. It consists of three layers of silicon pixel sensor in the Barrel and three discs each side in the Endcap, of the same material. The sensors are 250 μm thick, with oxygenated n-type wafers with the readout pixels on the n^+ implanted side of the detector. There are 1744 pixel sensors in total, which can operate at voltages of up to 600 V in order to provide good charge collection efficiency throughout the years of use. The size of one pixel sensor is 50×400 μm^2 for 90% of the sensors, and the rest are 50×600 μm^2. There are in total 46080 readout channels.

---

[2]Radiation length, X_0 is the mean path length required to reduce the energy of high energy electrons through Bremsstrahlung by the factor $1/e$, or 0.368, as they pass through matter.
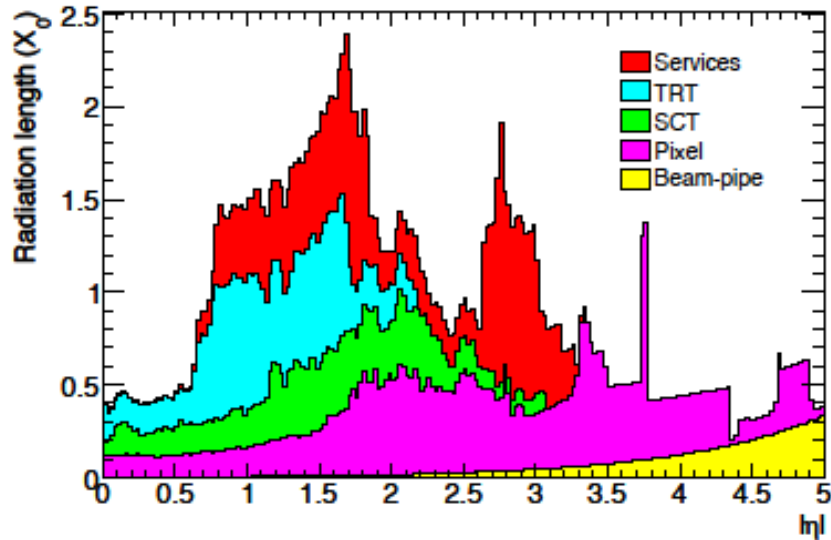
Figure 3.5: *Material in the ID in terms of radiation length X_0 as function of $|\eta|$ [29].*

SCT

The SCT consists of four cylindrical layers in the Barrel and nine disks on each side
of the Endcap. Each layer contains modules of two pairs of single-sided micro-strip
sensors glued back to back. There are a total of 15912 sensors of p-in-n junction[3]
with AC-coupled readout strips.

In Chapter 4 a more extensive description is provided.

TRT

The TRT consists of Polyamide drift, straw-shaped, tubes. The straw tube wall was
developed to have good electrical and mechanical features within a small amount of
material and is made of two 35 mm multi-layer films glued back to back. The TRT
provides discrimination between electrons and pions over the energy range between
1 and 200 GeV by utilizing transition radiation. Transition radiation happens when
a charged particle passes through inhomogeneous media.

The TRT provides a large number of hits per track (usually 36) and allows

---

[3]p-n junction consists of two semiconductor regions with opposite doping type. Current will
flow readily in one direction (forward biased) but not in the other (reverse biased). The -n is the
conducting band while the p- is the valence band. When a p-n junction is formed, some of the free
electrons in the n-region diffuse across the junction and combine with holes to form negative ions
in the depletion area.
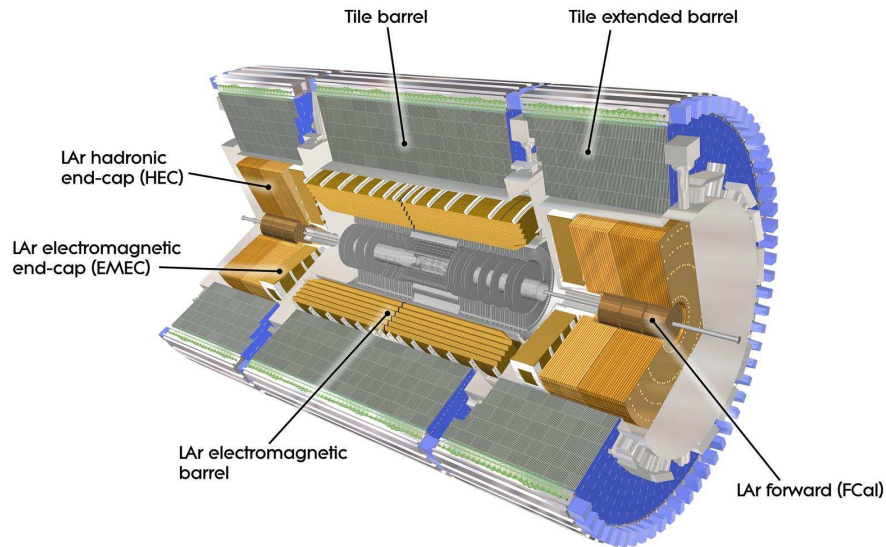
Figure 3.6: *View of the Calorimeter system [29]. The inner part is the electromagnetic calorimeter. This is surrounded by the hadronic calorimeter system.*

tracking up to $|\eta| < 2.0$. It only provides $R-\phi$ (R denotes radial length) information when an intrinsic accuracy on 130 mm per straw is provided. In the Barrel region, the straws are 144 cm long and run parallel to the beam axis. In the Endcap, the 37 cm long straws are arranged radially in wheels. The total number of readout channel is around 351000.

3.3.4 Calorimetry

The calorimeter system provides the information on both position and energy of a given particle with excellent resolution.

A calorimeter works by collecting and measuring the energy deposited by a particle shower. The energy may be measured fully if the calorimeter is able to fully contain the particle shower, or it can be sampled, which is the case of the calorimeter under discussion. Calorimeters typically consist of layers of absorbing high density material, such as lead alternated with layers of active medium, like solid lead-glass or liquid argon.

In Figure 3.6 the system of calorimeters in ATLAS is presented. It consists of two sub-systems: the EM calorimeter and the hadronic calorimeter. The calorimeters cover a range $|\eta| < 4.9$, so they have to cope with the specifics of the different physics processes that occur through them. They consist of sampling detectors with full symmetry in ϕ and good coverage around the beam axis.

The EM calorimeter detects the particles that interact electromagnetically, such as charged particles and photons, whereas the hadronic calorimeter absorbs the energy from the particles that go through the EM calorimeter and interact via the strong force; these are mainly hadrons, as the name suggests.

EM Calorimeter

The EM calorimeter is the closest to the beam line. It is divided into a Barrel part ($|\eta| < 1.475$) and two Endcap components ($1.375 < |\eta| < 3.2$), all of them enclosed in their own cryostat. There is a centre solenoid in front of the EM calorimeter, which shares the same vacuum vessel with the ID, thus eliminating the need for two vacuum walls. The active medium of the EM is lead-liquid Argon (LAr) and the absorber medium is lead over the full coverage of the system. The EM calorimeter consists of accordion-shaped kapton electrodes. Such geometry gives full ϕ symmetry without cracks in the azimuthal component. In terms of radiation lengths, the total thickness of the EM calorimeter is more than 22 X_0 in the Barrel and more than 24 X_0 in the Endcap.

The Barrel is divided into two halves, separated in $z = 0$ by a gap of approximately 4 mm. Each Endcap is divided into two coaxial wheels: the outer one covers the region $1.375 < |\eta| < 2.5$ whereas the inner one covers $2.5 < |\eta| < 3.2$.

For the region $|\eta| < 1.8$, a presampler detector is used to correct for the energy lost by electrons and photons before the detector. This presampler consists of a 1.1 cm layer of active LAr in the Barrel and a 0.5 cm layer of active LAr in the Endcap.

Hadronic Calorimeter

The hadronic calorimeter is the next system after the EM calorimeter. In Figure 3.6 the different subsystems are shown: the Tile Barrel and extended Barrel, LAr hadronic Endcap and the LAr forward calorimeter.

- **Tile Calorimeter**. The Tile calorimeter is a sampling calorimeter with steel as the absorbent medium and scintillator as the active medium. Radially, it extends from an inner radius of 2.28 m to an outer radius of 4.25 m. It is composed of a Barrel, that covers $|\eta| < 1.0$ and two extended Barrels, covering $0.8 < |\eta| < 1.7$. These two parts are divided azimuthally into 64 modules.

  The Tile calorimeter is segmented in depth in three layers of different interaction lengths (λ): 1.5, 4.1 and 1.8 (Barrel) and 1.5, 2.6 and 3.3 (extended Barrel). The total detector thickness, in terms of interaction length is 9.7 λ, at

$\eta = 0$. Two separate photomultiplier tubes read out, by means of wavelength shifting fibres, the two sides of the scintillating tiles.

- **LAr Hadronic Endcap Calorimeter**. The Hadronic Endcap Calorimeter (HEC) has a flat designed copper/liquid-argon (copper plates interleaved with the active medium LAr) sampling calorimeter, which covers $1.5 < |\eta| < 3.2$. It shares each of the two liquid-argon Endcap cryostats with the EM calorimeter Endcap and the forward calorimeter. The limits of the range in η overlap with both the EM calorimeter and the forward calorimeter in order to reduce in material at the transitions with these detectors.

  The HEC is composed of two wheels in each Endcap cryostat, the front and the back wheel, containing two longitudinal sections. These four wheels each have 32 identical wedge shaped modules. The wheels closer to the interaction point are built from 25 mm parallel copper plates, whereas the ones further away have 50 mm copper plates. The inner and outer radius of the copper plates is 0.475 m and 2.03 m respectively.

- **LAr forward calorimeter**. The Forward Calorimeter (FCal) shares its cryostat with the Endcaps of the calorimeter and provides a coverage of $3.1 < |\eta| < 4.9$. As it is quite close to the other systems, it is of a hermetic design and allows for less energy loss in the cracks and minimises background for the Muon system. The FCal is approximately 10 λ, and each FCal side is composed of three 45 mm deep modules: one electromagnetic module (FCal1) and two hadronic modules (FCal2 and FCal3). Copper plates are the absorber medium for FCal1 and tungsten is the absorber for FCal2 and FCal3, in order to contain and decrease the lateral spread of the hadronic showers.

  Also to reduce background in the Endcap muon system, a shielding plug of copper alloy was mounted behind the FCal3.

3.3.5 Muon System

The Muon system is the outer most layer of the ATLAS detector. It is shown in Figure 3.7. It is designed to detect charged particles exiting the detector (mainly muons) and measure their momentum in a range of $|\eta| < 2.7$. It also serves to trigger high energy muons. The toroids that can be observed in Figure 3.7 are large superconducting air core toroid magnets and serve to bend the trajectories of the muons. In the Barrel the toroid has a trajectory coverage over a range of $|\eta| < 1.4$ and in the Endcaps over the range of $1.6 < |\eta| < 2.7$. In the range $1.4 < |\eta| < 1.6$, which is a transition region, the magnetic deflection is given by a combination of
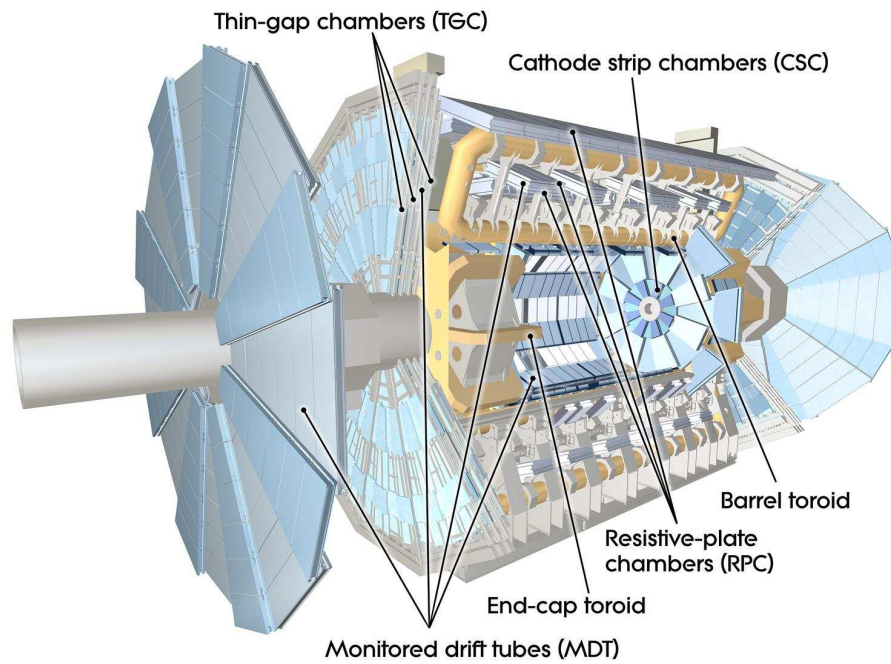
Figure 3.7: *View of the Muon system and its different composing parts [29].*

Barrel and Endcap fields. The other components of the muon system showed in Figure 3.7 are: Monitored Drift Tubes (MDT), Cathode Strip Chambers (CSC), Resistive Plate Chambers (RPC) and Thin Gap Chambers (TGC).

The MDT provide a precision measurement of the track coordinates in the deflecting direction of the magnetic field over almost all η range. The drift tubes are mechanically isolated to ensure a reliable and robust operation.

The CSC are multi-wire proportional chambers with cathodes segmented into strips and cover the range $2 < |\eta| < 2.7$, placed in the innermost plane of the system.

The RPC and TGC are part of the triggering system. The RPC are used in the Barrel and the TGC in the Endcaps; they cover the region $|\eta| < 2.4$ and serve three purposes: provide bunch crossing identification, give well defined p_T thresholds and measure the muon coordinates which are orthogonal to the one determined by the precision tracking chambers.

3.3.6 Magnetic System

The magnetic system involves the whole of the ATLAS detector. It is composed of four systems of large superconducting magnets, as listed below:

- Central Solenoid: is aligned with the beam axis and provides a 2 T magnetic
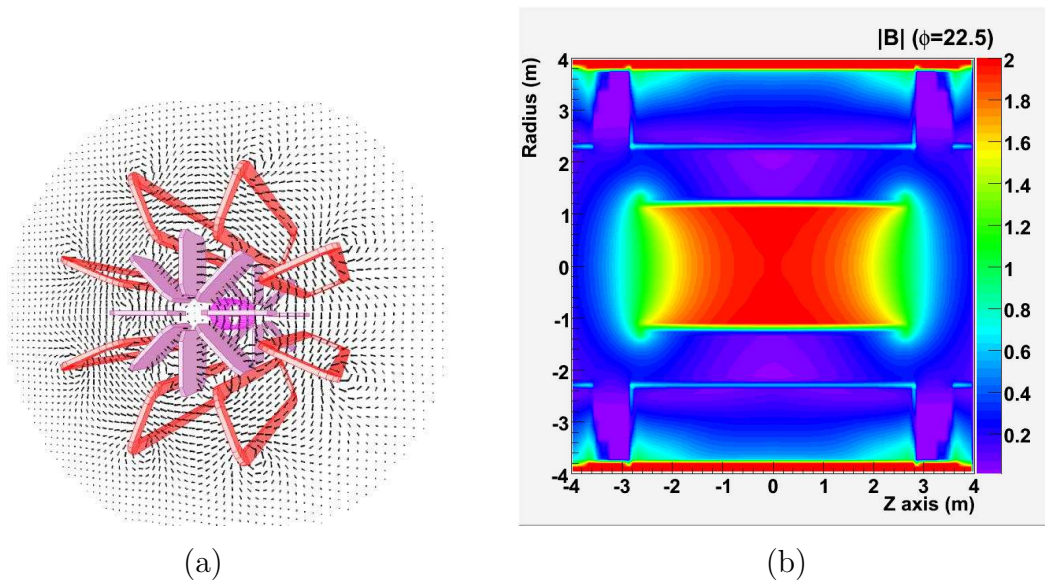
Figure 3.8: *(a) shows a schematic diagram of the magnet system with the magnetic field lines indicated. (b) shows the mapping of the magnetic field intensity around the central solenoid [32].*

field to the ID. Because of its proximity to the calorimeter, the material thickness next to the calorimeter needs to be very small, in this case of 0.66 λ at a normal incidence. The inner and outer diameters of the solenoid are 2.46 m and 2.56 m, with an axial length of 5.8 m. The conductor used is Al-stabilised NbTi, developed to achieve high fields while optimized the thickness.

- Barrel toroid: creates a 0.5 T magnetic field for the muon detectors around the centre. It consists of 8 flat superconducting race-track coils around the outer calorimeter structure, individually encased in stainless steel vessels. These coils are supported by 16 rings. Its conduction material is similar to the central solenoid: Al-stabilised Nb/Ti/Cu conductor.

- Two Endcap toroids: create a 1 T magnetic field for the muon detectors in the Endcaps. They can slide along central rails to facilitate access to other components. Each Endcap is composed of one cold mass inserted into the cryostat, eight coils and eight keystone wedges, all bolted and glued together into a rigid structure. Their inner and outer diameters are 1.65 m and 10.7 m, respectively.

Figure 3.8 (a) shows the shapes of all the magnet system components, as well as the field lines along the structure. Figure 3.8 (b) shows the mapping of the magnetic field intensity along the central solenoid, which goes up to 2 T.
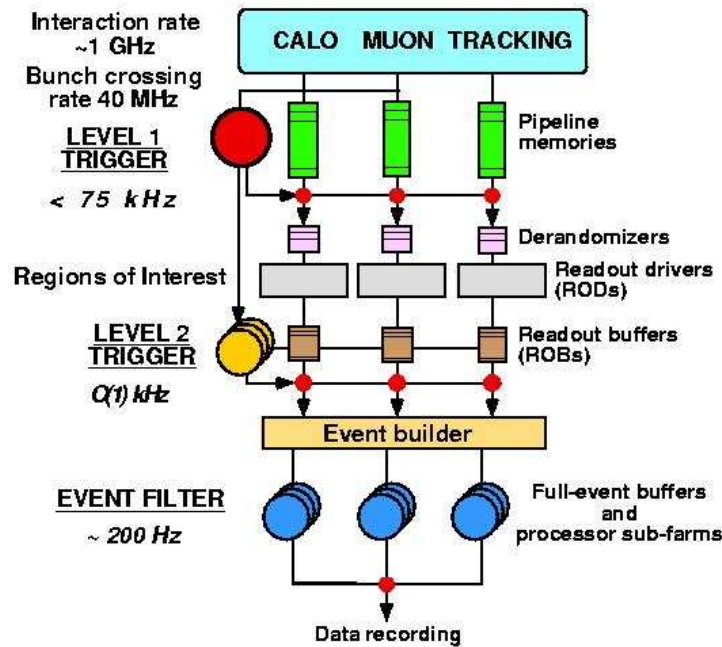
Figure 3.9: *Scheme for the Trigger system. There are three distinct trigger levels: Level 1, Level 2 and Event Filter, which accept decreasing rates of data [33].*

3.3.7 Forward Detectors

In addition to these main components described in the previous sections, there are three smaller detecting systems in the forward region of ATLAS:

- **LUCID - LUminosity measurement using Cherenkov Integration Detector**, situated at $\pm$ 17 m from the IP, as the full name indicates, this system determines the luminosity delivered to ATLAS. It is the main online monitor for the relative luminosity in ATLAS. It also detects inelastic p-p scattering in the forward region.

- **ALFA - Absolute Luminosity For ATLAS**, situated at $\pm$ 240 m of the IP. It also measures the luminosity via scintillating fibre trackers inside Roman pots designed to approach the beam as close as 1 mm.

- **ZDC - Zero Degree Calorimeter** is located at $\pm$ 140 m from the IP and its goal is to detect forward neutrons in a range $|\eta| < 8.3$ in heavy-ion collisions.

3.3.8 Trigger System and Data Acquisition

The Trigger system consists of three levels of event selection: Level-1 (L1), Level-2 (L2) and Event Filter (EF). The L2 and EF compose the High Level Trigger (HLT).

Figure 3.9 shows a schematic diagram of all these levels for the trigger system [33].

The L1 Trigger is implemented using electronics. It searches for signatures from high p_T muons, electrons/photons, jets, τ leptons that decay into hadrons, missing transverse energy and large total transverse energy. The information from the RPC and TGC, described above, is used by the L1 for the high p_T muons. For the remaining signatures, the calorimeter systems are used. The maximum rate which the L1 readout systems can handle is 75 kHz and its decision time is within 2.5 μs after the associated bunch crossing. The regions of the detector where the L1 has identified possible trigger objects in the event are called Regions of Interest (RoI's). These carry information on coordinates (η and ϕ), energy and type of signatures. The events selected by the L1 are passed to the readout drivers (RODs) via derandomizers, which average out the high data rate at the output to match with the input bandwidth of the RODs.

The L2 trigger then uses the RoI information to limit the amount of data transferred from the detector readout. It reduces the event rate to around 3 kHz, with a processing time of up to 40 ms. The information then passes to the readout buffers (ROBs) and from there to the EF, in a process called event building. The EF uses offline analysis procedures on fully-built events to further select events and to be able to reduce its rate to about 200-600 Hz, with an average processing time of about four seconds.

The whole HLT uses the data from the whole detector (muon system, ID and calorimeters) given full information on granularity and precision, since information on energy deposition improves the selection threshold cuts.

The Data Acquisition system (DAQ) receives and stores data temporarily in local buffers. If an event is associated with a RoI, the L2 passes that event. The events selected by the L2 are then passed on to the EF for final selection. The events that pass the EF are moved to permanent storage at the CERN computer centre. The DAQ is also used to monitor and control the software and hardware components that provide the data-taking tasks.

3.3.9   Radiation

The main source of background radiation in ATLAS comes from the IP. At smaller radii, the dominant background radiation is in the inner detector, created by charged hadrons from inelastic proton-proton interactions. At a larger radius other sources of background are dominant, mainly from neutrons.

Most of the energy from primary particles is absorbed in two regions: the FCal and the Target Absorber Secondary (TAS) collimators, which end up being the sources for secondary radiation.

In order to contain the effects from radiation, around 3000 tonnes of shielding are used in ATLAS. These are composed of three-layers: the inner layer, made of iron or copper stops high energy hadrons. The second layer is made of doped polyethylene hydrogen enriched and moderates the neutron radiation that escapes from the first layer. The third layer is made of steel or lead and stops the photons created by neutron capture.

3.3.10 Acquired Data And Detector Performance

From March 2010 up until November 2011, the LHC has been running at a centre-of-mass energy ($\sqrt{s}$) of 7 TeV and ATLAS has recorded around 5 fb^{-1}. During this time the LHC delivered a total of 48.1 pb^{-1} of integrated luminosity during the 2010 operation, and a total of 5.6 fb^{-1} of integrated luminosity during the 2011 operation. Furthermore, from March 2012 until December 2012, the LHC has been running at a centre-of-mass energy of 8 TeV and ATLAS has recorded around 20 fb^{-1}. The highest instantaneous luminosity achieved during this period was 7.4×10^{33}cm^{-2}s^{-1} [34].

Since 2009 ATLAS has been successful in acquiring data. A timeline of the ATLAS operation can be summarised as:

- End of 2009 - Second startup of LHC and first event collisions at a total energy of 0.9 TeV and later at 2.36 TeV. This was the highest achieved collisions energy ever;

- March 2010 - Proton-proton collisions with a centre of mass energy of 7 TeV, for about eight months. Also there were a few days of heavy-ion collisions in November;

- March 2011 - A full year of intensive data taking at 7 TeV, followed by a few weeks of heavy-ion collisions and a winter shutdown;

- March 2012 - Event collisions at $\sqrt{s} = 8$ TeV. Another year of intensive data taking;

- 2013 - A shutdown is scheduled to prepare ATLAS to increase the energy up to its design value of 14 TeV;

- Next 15-20 years - Data taking and publications are due to continue.

Figure 3.10 (a) shows, the delivered online luminosity in the years 2010, 2011 and 2012, for the p-p collisions and the Pb-Pb collisions. The latest we acquired during a few weeks in November 2010 (magenta line) and November 2011 (torquoise line).
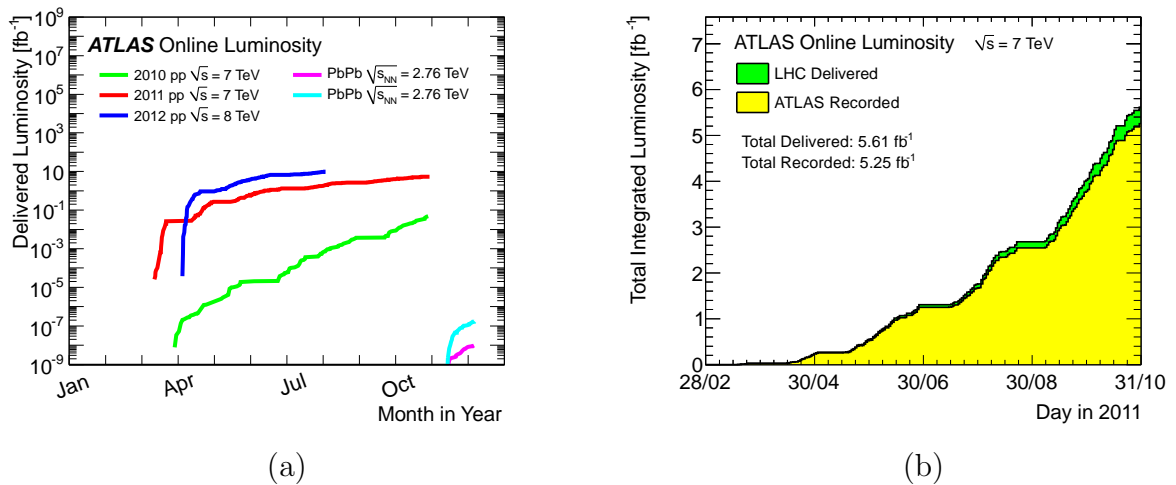
Figure 3.10: *(a) Delivered luminosity throughout the months for the years 2010, 2011 and 2012, for the p-p collisions (green, red and blue lines) and the Pb-Pb ones (torquoise and magenta). (b) Total integrated luminosity for the year 2011, delivered to (green), and recorded by ATLAS (yellow) [35].*

Figure 3.10 (b) shows the total integrated luminosity for the whole 2011, in which this thesis will mainly focused. This luminosity is accumulated in ATLAS from the start of stable beams until the LHC requests to turn the sensitive detectors off, to start a beam dump. This luminosity is obtained through counting rates provided by the luminosity detectors, which are calibrated via the Van-Der-Meer beam-separation method, where the two opposing beams are scanned in the horizontal and vertical planes in order to be able to measure their overlap functions [35].

The first performance studies were done with the first collisions in 2009 [36]. The overall efficiency for data-taking was about 90% and the subdetectors operated in general at 99%. Collision candidates were selected with very low background levels. The Trigger/DAQ computing infrastructure was very effective. The tracking and electromagnetic calorimeter were the most tested, due to their proximity to the interaction point and performed well [36]. For the tracking system, there was a very precise clustering due to studies related to incident and Lorentz angles and very good spatial resolution. Its hit efficiencies, resolutions and particle identification capabilities are well modelled by Monte Carlo simulations, indicating that the tracking system is well understood. Good calorimeter performance was demonstrated by the measurement of the resolution of the missing transverse energy, following the expectations from Monte Carlo over the entire energy range studied [36].

Figure 3.11 shows the relative fraction of good quality data for the most recent pp collision runs. As can be seen, the overall performance is nearly 96% and the

ATLAS p-p run: April-December 2012										
Inner Tracker			Calorimeters		Muon Spectrometer				Magnets	
Pixel	SCT	TRT	LAr	Tile	MDT	RPC	CSC	TGC	Solenoid	Toroid
99.9	99.1	99.8	99.1	99.6	99.6	99.8	100.	99.6	99.8	99.5
All good for physics: 95.5%										
Luminosity weighted relative detector uptime and good quality data delivery during 2012 stable beams in pp collisions at √s=8 TeV between April 4th and December 6th (in %) – corresponding to 21.3 fb⁻¹ of recorded data.										

Figure 3.11: *Relative fraction of good quality data obtained between April and December of 2012 amounting to 21.3 fb^{-1}, weighted by luminosity for the different subdetectors in pp collisions at $\sqrt{8}$ TeV [37].*

detector uptime is higher than 99% for all systems.

Chapter 4

Lorentz Angle Studies In The ATLAS SCT

This chapter describes the Semiconducter Tracker (SCT) and the calculation of the Lorentz angle.

4.1 The SCT

The SCT is a high resolution tracking system which measures the trajectories of charged particles produced in particle interactions at high energy at the LHC. It is a part of the Inner Detector, along with the Pixels detector (closest to the collision point) and the TRT. These three detectors are designed to allow precision measurements of charged particles trajectories where numerous tracks are present. The Pixels mainly measure vertices accurately, whereas the SCT measures precisely the particle momenta and the TRT facilitates the pattern recognition, through its large number of hits.
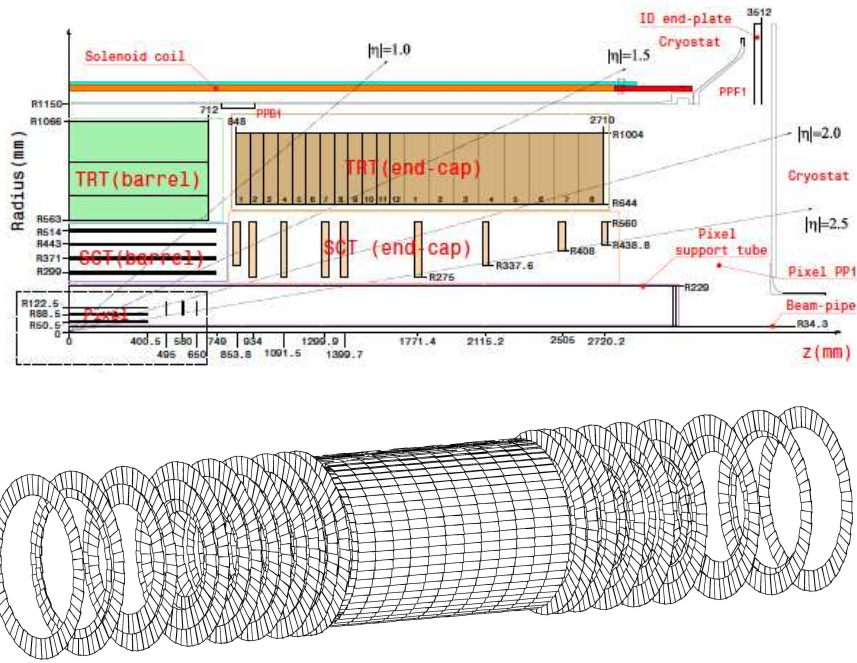
Figure 4.1: *Top, diagram of a quarter-section of the inner detector system, in terms of the z and radial distances. Bottom, a scheme of the SCT cylindrical shape. Both the Barrel and the Endcap are shown [29].*

In Figure 4.1, top, is a diagram of a quarter-section of the Inner Detector system: the Pixels, SCT and TRT, where the z and radial distances are shown, as well as the $|\eta|$ coverage. The ID covers a region of $|\eta| < 2.5$. The bottom diagram shows the shape of the SCT: cylindrical, with the Barrel layers around the collision point and the Endcap layers perpendicular to the beam direction.

The SCT is a system of 4088 Silicon Strip modules. 2112 of the modules are distributed through four layers around the beam pipe (Barrel) and 1976 modules in 18 disks (nine on each side) perpendicular to the beam pipe (Endcap).

The SCT uses semiconductor technology, each module is built with two pairs of single-sided, p-in-n silicon micro-strip sensors glued back to back around a high thermal conductivity substrate.

When silicon is doped in a manner that a region of n-type is adjacent to a p-type, a p-in-n junction is created. For the p-in-n junction to be in thermal energy, the Fermi energy[1] must be at the same level on both sides. This equilibrium happens with a small transfer of electrons from the n-type to the p-type, where they will annihilate with the holes. When this transfer happens, a region without free

---

[1]Fermi energy is the energy difference between the highest and lowest occupied single-state particles in a quantum system of non-interacting fermions at absolute zero temperature.

charge carriers is created, called the depletion zone. In this zone, the donor and acceptor ions are locked into the lattice creating a region of space charge, that in its turn originates a potential difference across the junction which bends the valence and conduction bands. Valence band is the highest energy band that is occupied and conduction band is the next group of electron energy levels above the valence band [38]. Figure 4.2 shows the described behaviour of a p-in-n junction: a) shows p- and n- zones, with the junction at $x = 0$, b) shows the variation of the charge carrier concentration with x. c) Shows the charge density, $\rho(x)$ and d) shows the bending of the valence and conduction bands.
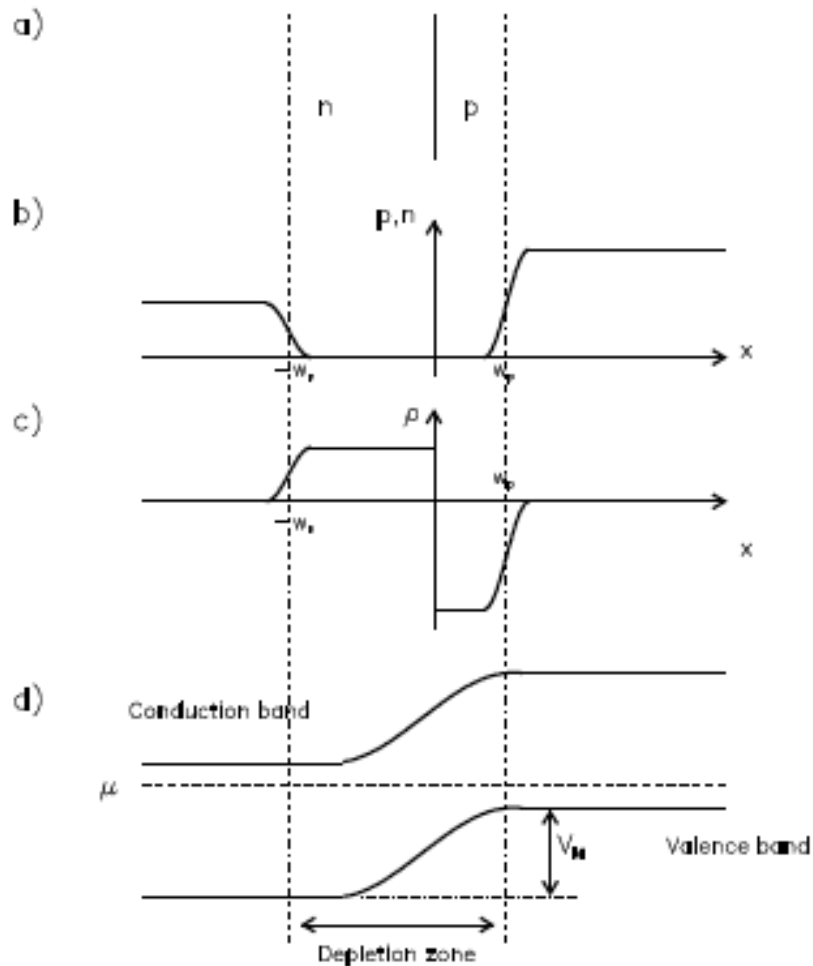
Figure 4.2: *Schematics of a p-in-n junction in silicon: a) p- and n- zones, with the junction at $x = 0$, b) the variation of the charge carrier concentration with x, c) the charge density, $\rho(x)$ and d) the bending of the valence and conduction bands. [38].*

The sensor strips are AC coupled to binary read-out electronics with the ABCD3TA custom ASICs providing front-end amplification, discrimination, pipeline, deran-

domisation and data compression functions. A threshold of 1 fC is used to detect charge deposited on the strip [39].

The design of the SCT modules is shown in Figure 4.3, for the Barrel (left) and the Endcap (right). For the Barrel modules, the readout is between the two pairs of sensor strips, whereas for the Endcap modules it's located at the extremity of one of the pairs. The two sides of the strips are rotated by an angle of 40 mrad.

The ID is surrounded by a 2 T magnetic field created by the central Solenoid. This magnetic field is perpendicular to the modules of the Barrel and parallel to the ones in the Endcap.

4.2 The Lorentz Angle

The presence of a magnetic and electric fields generate a Lorentz force: the charge carriers drift at an angle, called the Lorentz angle. A particle passes through the silicon and generates charge carriers which drift along a direction at an angle ϕ_L (Lorentz angle) with respect to the electric field direction.

In Figure 4.4 a schematic view of particles crossing the silicon is shown. The top diagram shows a particle passing through the silicon perpendicularly; the charge carriers drift to the sensor and a hit is recorded if the deposited charge is above a certain threshold. In the bottom diagram, the incident particle crosses the sensor at an angle equal to the Lorenz angle, and the mean number of strips above threshold (cluster size) is a minimum in this case.

The Lorentz angle can be measured in the Barrel, where the magnetic field is perpendicular to the drift. For the Endcaps, the drift being almost parallel to the magnetic field, the Lorentz angle is approximately zero. The charge carriers considered for the SCT are the holes collected at the p-implant electrode.

4.2.1 Lorentz Angle Model Prediction

Theoretically, the Lorentz angle ϕ_L of the silicon in a magnetic field B is given by [41]:

$$\tan\phi_L = \mu_H B = \gamma\mu_d B, \qquad (4.1)$$

where μ_H is the Hall mobility, γ is a Hall factor, which is of the order 1 and μ_d is the drift mobility, proportional to the drift velocity, v_d. The following relationship holds: $\mu_d = \frac{v_d}{E}$, where E is the electric field.

According to the digitisation model [42], the electric field along the z direction of the sensor depth is given by:
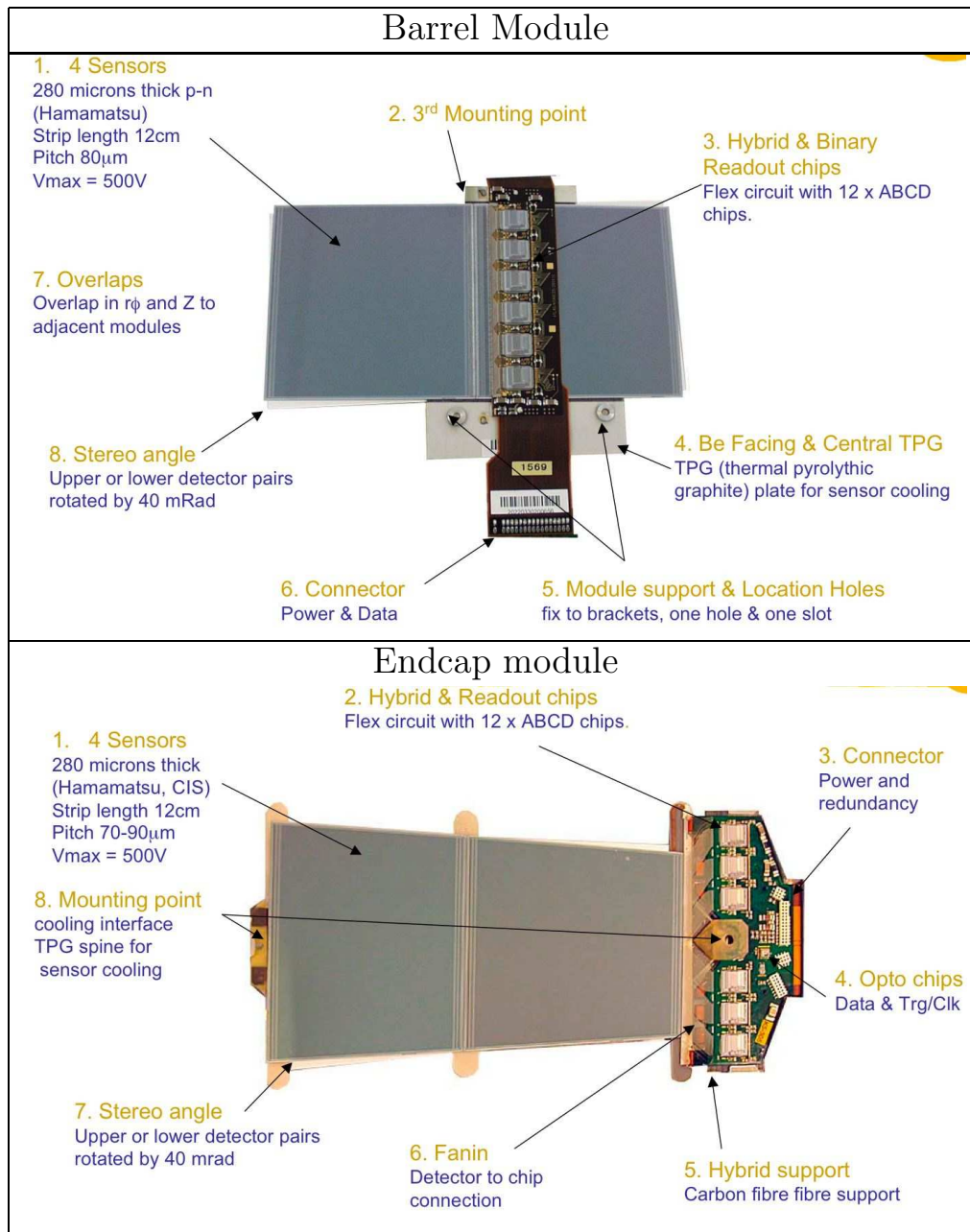
Figure 4.3: *Modules used in the Barrel and Endcap of the SCT [29].*
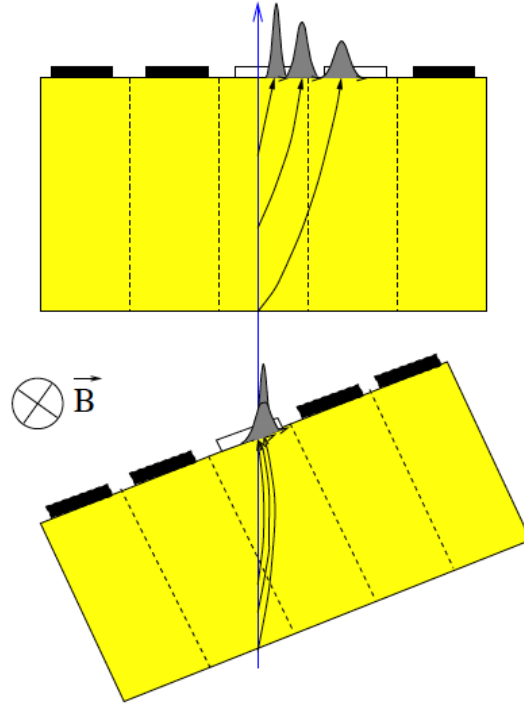
Figure 4.4: *Diagram of a particle passing through the silicon: the top figure shows a particle crossing the module perpendicularly. The bottom figure shows the particle crossing the sensor at the Lorentz angle [40].*

$$E_z = \frac{V_B + V_D}{d} - 2\frac{V_D}{d^2}z, \tag{4.2}$$

where V_B is the bias voltage necessary for the sensor to work, with its nominal value of 150 V, $V_D = 70$ V is the depletion voltage, d is the sensor thickness (285μm). The Lorentz angle is estimated in the centre of the sensor at $z = d/2$. The theoretical Lorentz angle value is predicted using Equations 4.1 and 4.2, for a temperature $T = -2°$ C (Layers 0, 1, 2) or $T = 4.5°$ C (Layer 3) and a magnetic field B of 2 T, with a drift velocity v_d of 2.29×10^6 cm s-1 [42]:

$$\phi_L(T = -2°) = 3.88 \pm 0.28, \quad \phi_L(T = 4.5°) = 3.71 \pm 0.27, \tag{4.3}$$

where the errors come from the model and are obtained with the uncertainties mentioned in Section 4.2.2. These are the values shown for the model expectation comparison in all the Lorentz angle results given in this chapter.

4.2.2   Drift velocity uncertainty

As shown in the next sections, the value for the Lorentz angle for collisions data differs from the one predicted by the model. The cosmic data results fail to show that this discrepancy due to the large statistical error associated with the measurement, derived from the low number of events available after selection.

The Pixel group already reviewed the uncertainty in the drift velocity, which in the case of this detector is the drift velocity of electrons, from 5% to 12% (see [40]), based on a set of different references. The Lorentz angle value in the Pixel system is also above the model prediction, but within the uncertainty [43]. The uncertainty on the drift velocity v_d dominates the systematic error, along with the electric field's non-uniformity, both currently set to 5%. In this section only a possible change in the drift velocity uncertainty is attempted, since the literature has not suggested a variation in the electric field uncertainty. The temperature and magnetic field variables also contribute to the systematic error in the Lorentz angle, but to a smaller degree, 0.03 degrees and 0.75%, respectively. The bias voltage and impurity in concentration uncertainty values are negligible. The expression for v_d is given by the parametrization [44]:

$$v_d = \mu_d E = v_s \frac{E/E_c}{[1 + (E/E_c)^\beta]^{1/\beta}}.$$ (4.4)

Where E (V/cm) is the electric field, v_s (cm/s) is the saturation velocity, E_c (V/cm) is the electric field scale at which the transition from the linear regime to the saturation occurs, and β describes the rapidity of the transition between the two regimes. The values can be found in Table 4.1, with $T = 300$ K and E $= 6 \times 10^6$ kV m^{-1}.

Parameter	Value
v_s	$1.68 \times 10^8 \times$ T$^{-0.52}$ cm sec^{-1}
E_c	$1.24 \times T^{1.68}$ V cm^{-1}
β	$0.46 \times T^{0.17}$

Table 4.1: *Parametrization values used for the drift mobility calculation [44].*

This parametrisation can be used in the case where the temperature T is above 150 K and the electric field is along the $< 111 >$ crystallographic direction. It has been obtained by the fitting of experimental data using the parameters listed above.

Figure 4.5 shows the drift velocity as a function of the electric field for room temperature, using the described parametrisation. This model is implemented in the SCT digitisation [42] and thus is present in the Monte Carlo simulation.
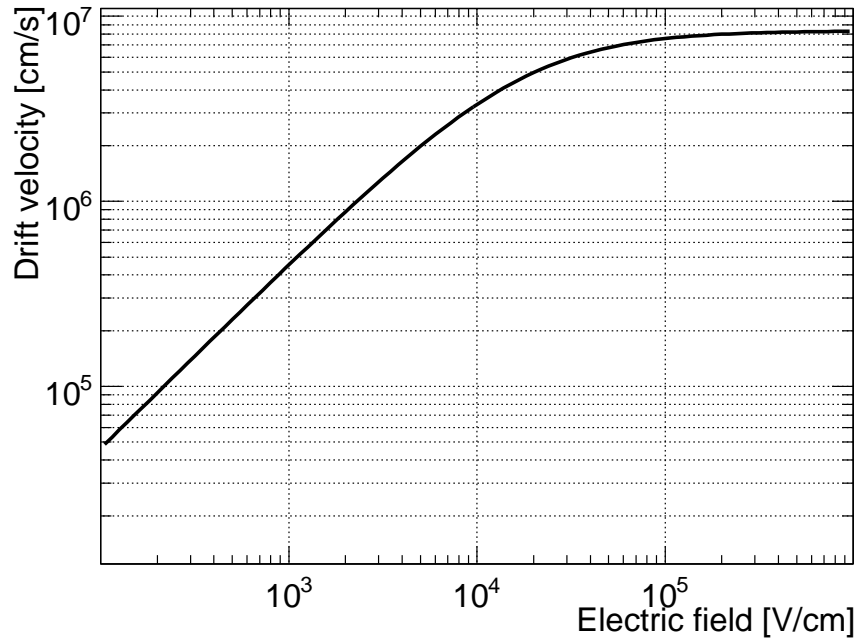
Figure 4.5: *Room temperature drift velocity of holes in silicon as a function of the electric field, according to parametrisation given in [44].*

Following the references given by Jacoboni ([44]-Figure 2), five articles are studied. They present two different methods of calculating the drift velocity of both electrons and holes, Time of Flight (ToF) and conductivity Technique:

- **Time of Flight** - Measures the time T_R taken by the charge carriers to travel across a region of thickness W under the influence of an electric field E ($v_d = W/T_R$) [44].

- **Conductivity Technique** - Measures the current density $j(E) = nqv_d(E)$, where n, the carrier density, is determined by the Hall effect and q is the carrier charge. n needs to be constant or a short-pulse can be applied to avoid being affected by changes of E [44].

The Conductivity Technique is less accurate in the determination of the v_d, since it is only applicable to materials of low resistivity and gives an indirect measurement of v_d. Hence, the ToF technique is more reliable.

The values obtained for the drift velocity are shown in Table 4.2. The drift velocity calculated through the Conductivity Technique gives lower values than the ToF technique. Taking into account the different values obtained in the literature, the uncertainty on the drift velocity should be increased to 12%, calculating this value

Reference	Method	v_d ($\times$ 10^6 cm s^{-1})	Uncertainty (%)
Canali et al [45]	ToF	2.20	5
Seidel [46]	Cond. Techn.	2.00	10
Rodriguez, Ruegg [47]	Cond. Techn.	1.70	5
Sigmon, Gibbons [48]	ToF	2.25	5
Norris, Gibbons [49]	ToF	2.30	5
Combined value (all methods)		2.04	12.03
Combined value (only ToF method)		2.25	2.22
Parametrisation value		2.29	

Table 4.2: *Values found in the literature for the drift velocity of holes in Silicon. The combined value is calculated through standard deviation and the parametrisation value is given by Equation 4.4.*

through the standard deviation, assuming all the measurements are independent and have the same weight.

However, if one only considers the ToF method, as it gives a more precise measurement, the uncertainty amounts to 2%, as shown in Table 4.2. So in the determination of the uncertainty for the drift velocity, only the ToF method was taken into account, and thus it can be concluded that the uncertainty value should not be changed from its previous value of 5%, which is already a very conservative value.

4.2.3   Lorentz angle Extraction and Calculation

The Lorentz angle is extracted mainly using the information of the number of consecutive strips above a chosen charge threshold.

Layers 0, 1 and 2 have a temperature of -2° C, whereas Layer 3 has a higher temperature of +4.5° C. Therefore, the Lorentz angle is different on the layer further away from the interaction point.

The incidence angle is measured in the plane defined by the normal to the wafer surface and the axis (in the wafer plane) perpendicular to the strip direction. The cluster size is given by the number of consecutive strip that were above threshold. Hence the Lorentz angle is given by the incidence angle which corresponds to the minimum of the average cluster size.

Figure 4.6 shows a schematic view of a cosmic ray traversing the SCT Barrel. The modules are slightly tilted with respect to the Barrel, as can be seen on the left side. On the right hand-side of Figure 4.6 the diagram of an incident particle trajectory in the module and the angle that is measured are shown. To extract the
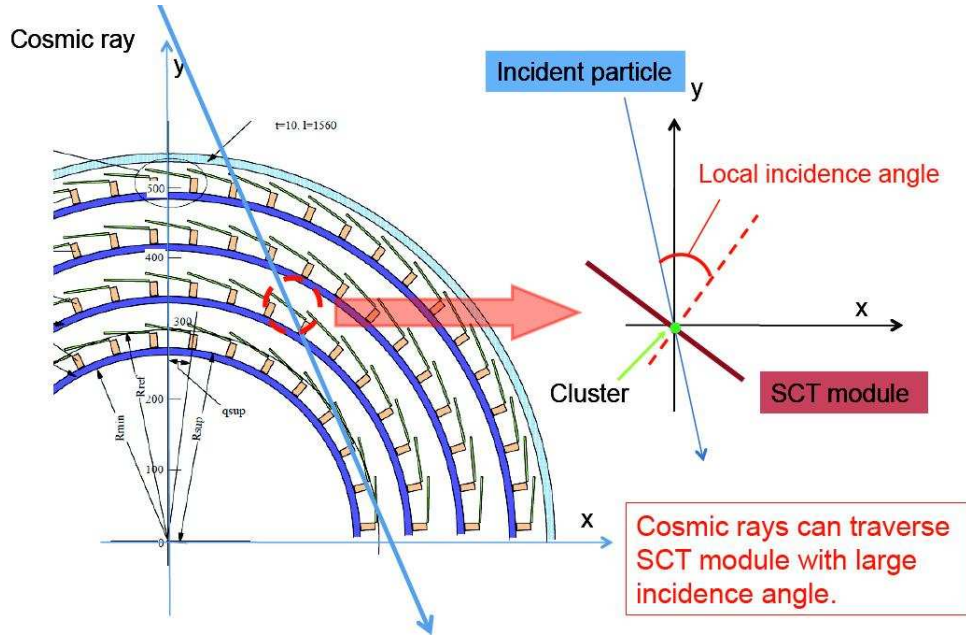
Figure 4.6: *Drawings of the SCT transverse section and the SCT wafer [50].*

angle for which the cluster size has its minimum, a fit is made following the empirical expression [51]:

$$
\begin{aligned}
f(\phi) &= (a|\tan\phi - \tan\phi_L| + b) \otimes \mathrm{Gaussian}(\phi) \qquad\qquad (4.5)\\
&= \int_{-\infty}^{+\infty} (a|\tan\phi - \tan\phi_L| + b)\frac{1}{\sqrt{2\pi}\sigma}\exp\left(-\frac{(\phi-\phi')^2}{2\sigma^2}\right)d\phi'.
\end{aligned}
$$

This expression gives the average cluster size as a function of the track's incidence angle, $f(\phi)$ and has four parameters: the Lorentz angle, ϕ_L, the slope, a, the minimum cluster size, b and the smearing effect, σ. The experimental data is only well fitted by this expression in a small region around the minimum (the literature range is within $\pm 12.5°$ around the minimum). This function fails to be adequate for larger incidence angles. Figure 4.7 shows the shape of the function used, for the whole range of the incidence angle (left) and for the area around the minimum (right).

The fit is done on a TProfile distribution, a 2D histogram that displays the mean value of Y (the average cluster size) and its RMS for each bin in X (the incidence angle) [52].

There are two types of different data acquired on the SCT: cosmic ray data, when the SCT is ON and records the events originating only from cosmic ray events and collision data, when the SCT records the proton-proton collisions. The statistics acquired for the cosmic runs are far less than for the collision data.
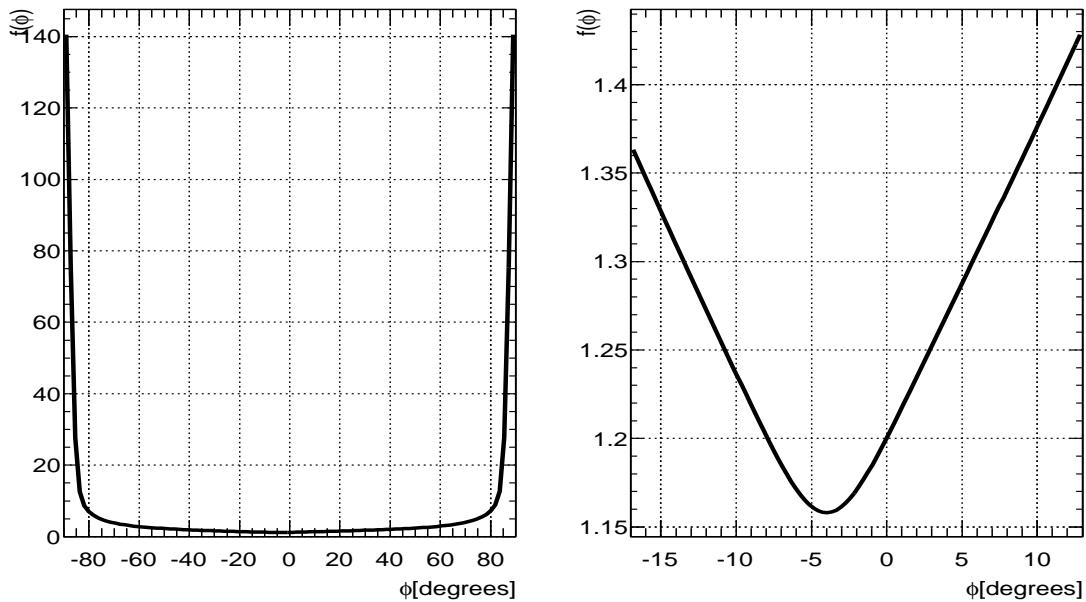
Figure 4.7: *The function f(φ) used in the fit of the profile of the average cluster size as a function of the incidence angle. The parameters used for this plot are adequate for the latter. The plot on the left shows the full range of the function. On the right the function zoomed around the minimum is shown.*

The Monte Carlo simulation is obtained through the digitisation model for the SCT. In this chapter, the several cosmic ray data samples are presented in tables throughout, the collisions data runs used are the ones acquired when 7 TeV collisions where available, choosing only the luminosity blocks when the SCT Barrel had the high voltage (HV) on at a nominal voltage of 150 V. The reconstruction stream used is the MINBIAS stream. In order to compare with the collisions data, the Monte Carlo used is a Minimum Bias sample (dataset 105001).

4.3   Cosmic Rays Studies

Before collision data were available, the SCT was already working fully with the available data originating from cosmic ray events. This data allowed for a range of studies to be performed, concerning the Lorentz angle measurement.

Selection of Events

The cosmic ray events here analysed were acquired between October 2009 and February 2010. Due to low statistics, a set of very loose selections are applied:

- Number of Silicon Hits ≥ 8 or number of TRT Hits ≥ 30;

- Impact Parameter[2], $d_0 \leq 500$ mm;

- Transverse momentum, $p_T \geq 1$ GeV;

- $-10ns \leq$ TRT event phase[3] ≤ 40 ns (not zero);

- Consider clusters associated with a good track.

This selection is taken from the previous analysis [51] and kept for all the cosmic data analyses.

4.3.1 Voltage Dependence Studies

The Lorentz angle depends on the magnetic field, the temperature, the mobility and the bias voltage. For full depletion of the sensors, the minimum bias voltage is 70 V. The nominal reverse bias voltage is set at 150 V. To check the dependence on the bias voltage, cosmic runs were taken varying the voltage of Layer 2 of the SCT Barrel, between 30V and 350V. All the other layers (Layers 0, 1 and 3) remain with the unchanged nominal voltage of 150 V. Table 4.3 lists the run number of the data used, the voltage set for Layer 2 and the date those runs were taken. The nominal voltage of 150 V is also used in some of the runs.

Figures 4.8 and 4.9 show the dependence of the Lorentz angle on the voltage. On Figure 4.8 is the value as a function of the voltage. The full lines show the expected values for different temperatures. The red dots are from more recent runs than the black ones. For smaller voltages, the Lorentz angle values are less reliable, since the minimum applied voltage to have fully depleted sensors is about 70 V. The values of the more recent runs differ and are smaller than the runs acquired earlier.

On Figure 4.9, is shown the average cluster size as a function of the incidence angle for all the runs with different voltage, older and more recent ones. The runs above the minimum depletion voltage have a similar distribution, whereas the ones below show a visibly decreasing slope, which is caused by the cluster size being smaller, as not all the charge is deposited.

---

[2]The Impact Parameter, d_0, is defined as the distance between the point of closest approach of a track and primary vertex in the transverse plane x,y.

[3]The TRT event phase is the measurement of the time of an interaction. For collision data, it's defined as the time when a track passes through the Barrel of the TRT with respect to the bunch spacing. For the cosmic ray data case the time is measured with respect to the readout window measured by the TRT. This event phase information includes readout window offset and time of flight effects [53].

Layer 2 HV	Run number	Date
30 V	136455, 136459, 136460, 136599	October 2009
40 V	136379, 136409	October 2009
50 V	135863, 135855, 136183, 136176, 135926	October 2009
60 V	135664, 135736, 135813, 135816	October 2009
100 V	139016	October 2009
150 V	134967, 135106	October 2009
	147931	February 2010
200 V	135140, 135146, 135195	October 2009
250 V	135304, 135351, 135356	October 2009
300 V	135388, 135441	October 2009
	148072	February 2010
350 V	148209	February 2010

Table 4.3: *List of cosmic ray runs for which Layer 2 of the SCT Barrel has a different voltage applied. Three runs at nominal 150 V are also included.*

θ angle re-weighting study

Taking into consideration the discrepancy between cosmic runs acquired at different dates, a study has also been made to assess whether the θ angle is dependent on the incidence angle used to measure the Lorentz angle. The θ angle is defined as the angle measured in the plane described by the normal to the wafer surface and the axis parallel to the strip direction.

The θ distribution of the old run (October 2009) is weighted to the distribution of the most recent runs, and the incidence angle distribution is redrawn with a different weight for each event. In Figure 4.10 the result of the re-weighting is shown. (a) shows the θ distribution for the two different runs and the oldest run re-weighted. As intended, the re-weighted run has the same shape as the February run. The incidence angle as a function of the average cluster size is also shown (Figure 4.10 (b), (c)) and as can be observed, the incidence angle distribution does not change.

This is also verified in Figure 4.11, where the Lorentz angle value is shown by layer for the February run (left), October run (middle) and the reweighed October run (right). To be noted that despite the Lorentz angle being a negative quantity, it is depicted as positive on these plots. That is a mere case of convenience. All the similar distributions henceforth will have the same feature.
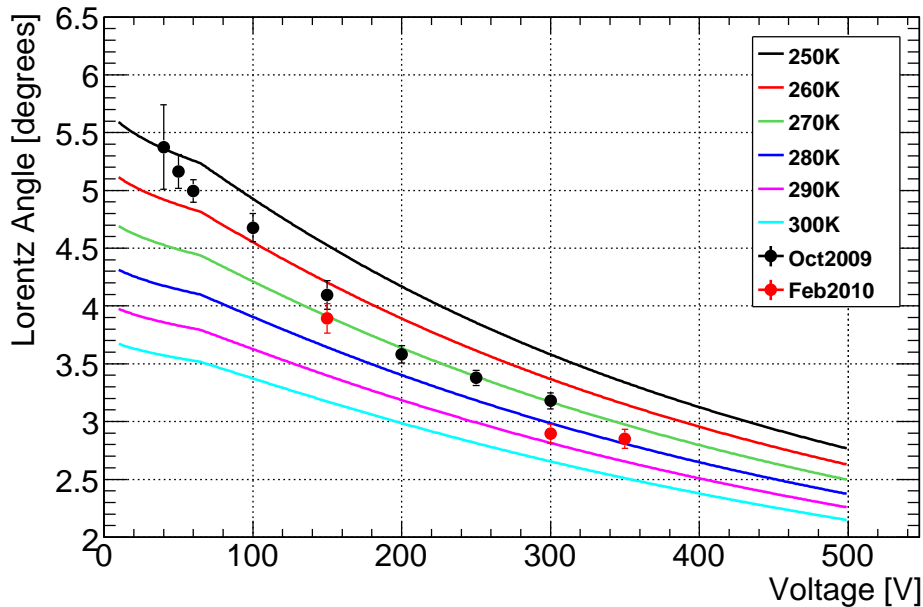
Figure 4.8: *Lorentz angle value as a function of voltage. Continuous lines show the temperature dependence of the Lorentz angle value from the model. Points correspond to fit results for Layer 2 of the SCT Barrel as this is the only one on which the applied voltage has changed in each run. Black points represent the October 2009 runs, while the red ones represent February 2010 [50].*

4.3.2 Threshold Cut

In the SCT, the signal collected is of the holes which drift towards the electrodes. This signal is amplified with a nominal threshold of 1 fC: when the charge exceeds this value, an impulse is recorded.

Run	t.c. (fC)	date	duration	# events
138460	1	Nov 09 2009	12h 13m	8,548,90
138598	1.1	Nov 10 2009	2h 7m	178,411
138623	1.1	Nov 10 2009	0h 20m	101,947
138628	1.1	Nov 10 2009	0h 9m	47,090
138630	1.1	Nov 10 2009	12h 24m	8,314,904
138790	1.2	Nov 11 2009	12h 7m	13,033,631

Table 4.4: *Cosmic runs taken between June and November 2009, varying the threshold cut in the SCT, in the range from 0.9 fC to 1.2 fC. One run with the nominal 1.0 fC threshold is included for comparison.*
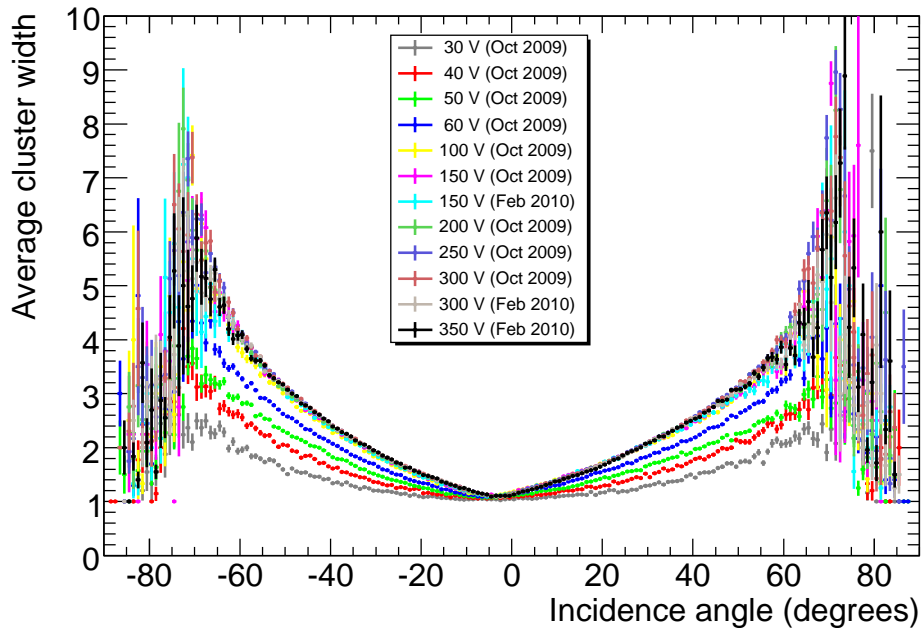
Figure 4.9: *Distribution of the average cluster size as function of the incidence angle for various cosmic runs corresponding to different voltages applied to Layer 2 of the SCT Barrel. The High voltage for this layer changes between 30 V up to 350 V [50].*

Some cosmic runs were taken varying this threshold in the SCT, in the range from 0.9 fC to 1.2 fC. These cosmic runs were taken between June and November 2009 and they are shown in Table 4.4: one run with the nominal 1.0 fC threshold is included for comparison. All these runs have been analysed and the Lorentz angle determined and compared to the previously measured values.

The plots in Figure 4.12 show the Lorentz angle values as function of layer for each threshold cut value (left column) and some example fitted plots for the average cluster size as function of the incidence angle for these test runs. No meaningful difference or defined trend can be observed in the values, dominated by statistical fluctuations varying layer by layer. Note that the results for a threshold cut of 0.9 fC were considered inconclusive, due to the lack of statistics, not allowing the fit to converge.

As expected, the conclusion can be made that the Lorentz angle does not depend on the threshold cut.

4.3.3 Null test: B-off runs

In the absence of a magnetic field, the charge carriers are not deflected, so the minimum of the cluster size must occur at null incident angle. As a test, runs in
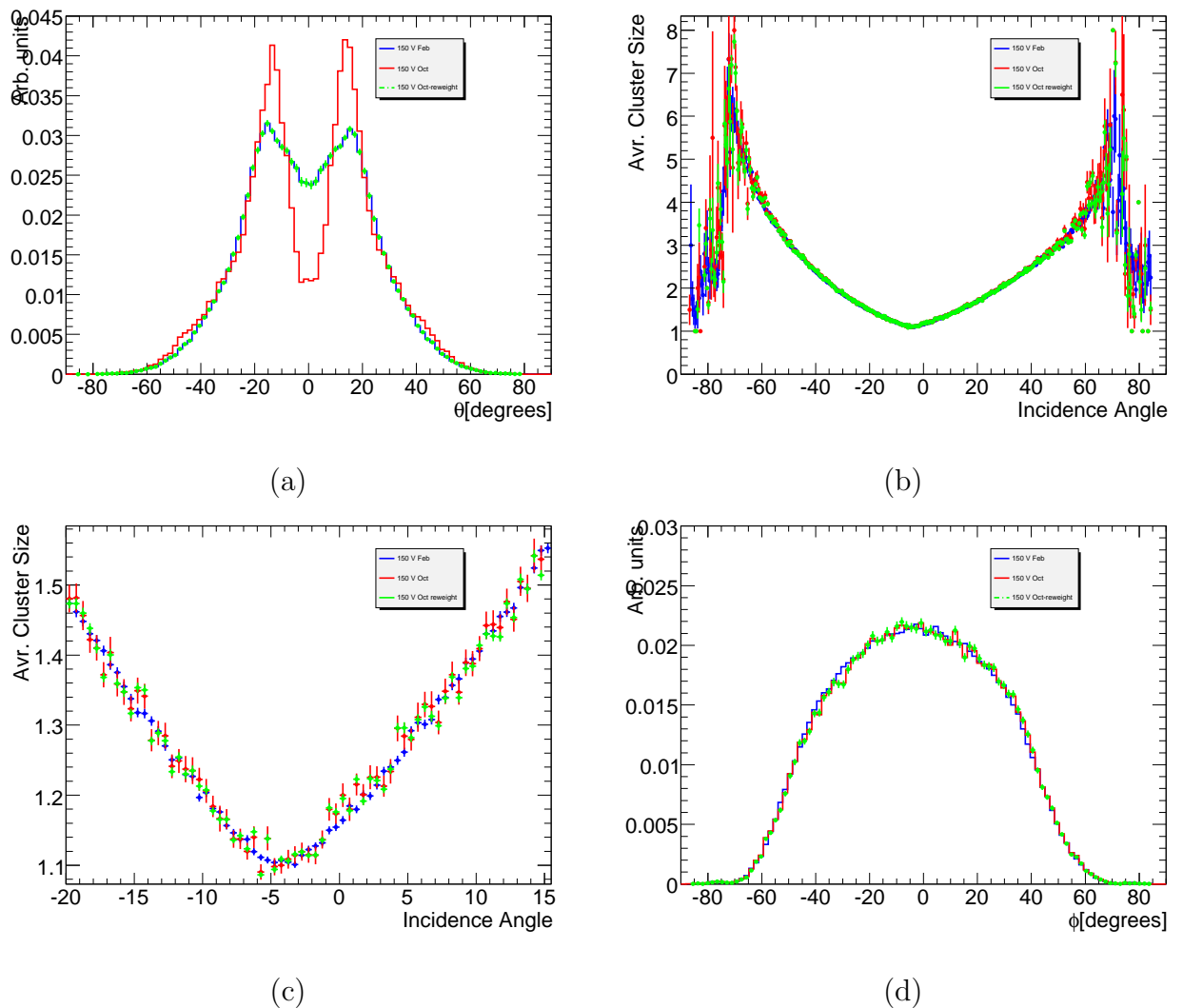
Figure 4.10: *Re-weight of the 150 V October run to the February run: (a) θ distribution for the October run (red line), February run (blue line) and the October run re-weighted (dashed line). (b) Incidence angle as a function of the average cluster size for the same conditions. (c) The latter plot zoomed around the minimum. (d) The incidence angle distributions.*

which the magnetic field is switched off have been analysed (see Table 4.5 for the runs description).

As can be observed from Figure 4.13, there is an agreement with zero and with previous measurements [51].
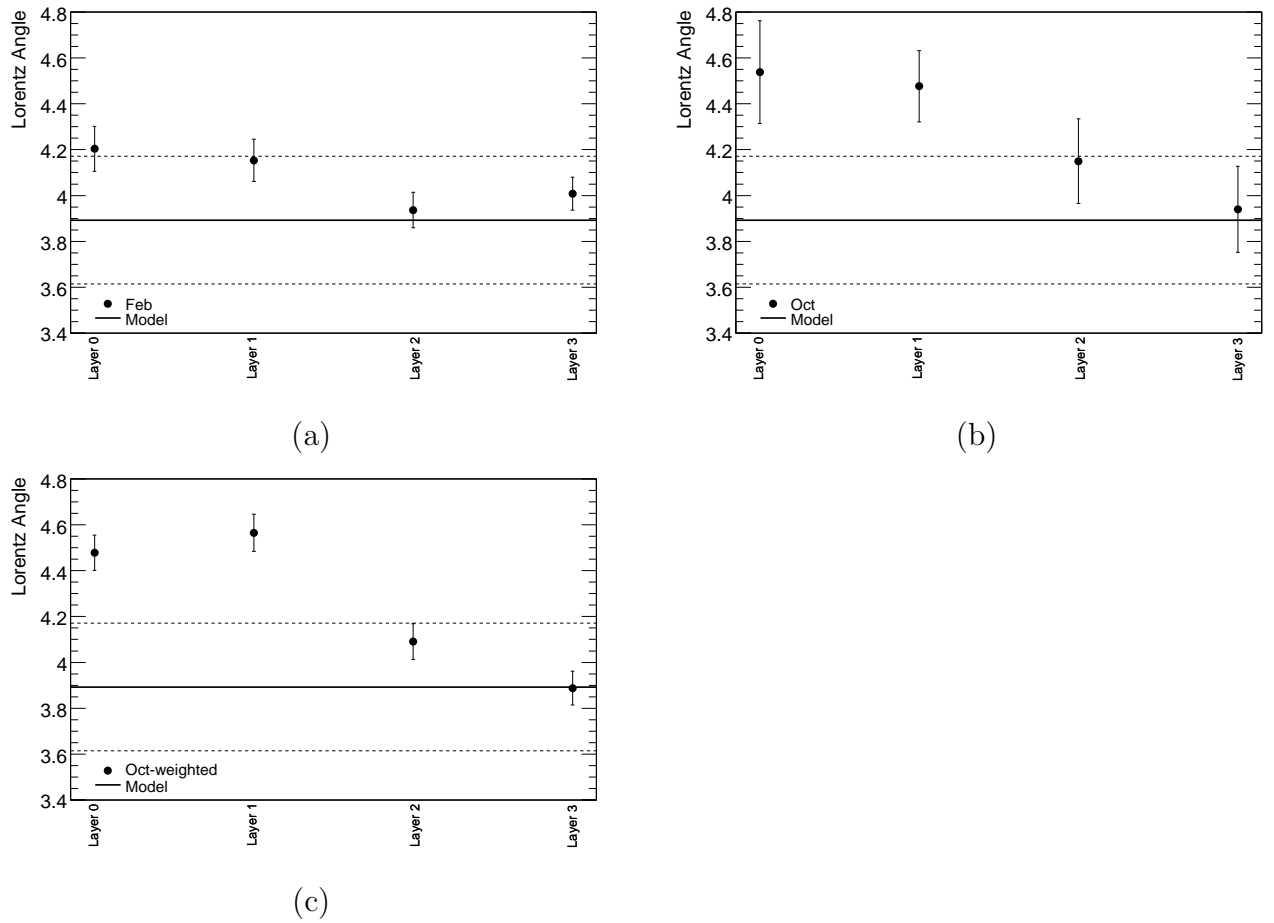
Figure 4.11: *Lorentz angle values by layer of the February run (a), October run (b) and the reweighed October run (c) The consistency in the reweighing process (statistical errors only) is shown.*
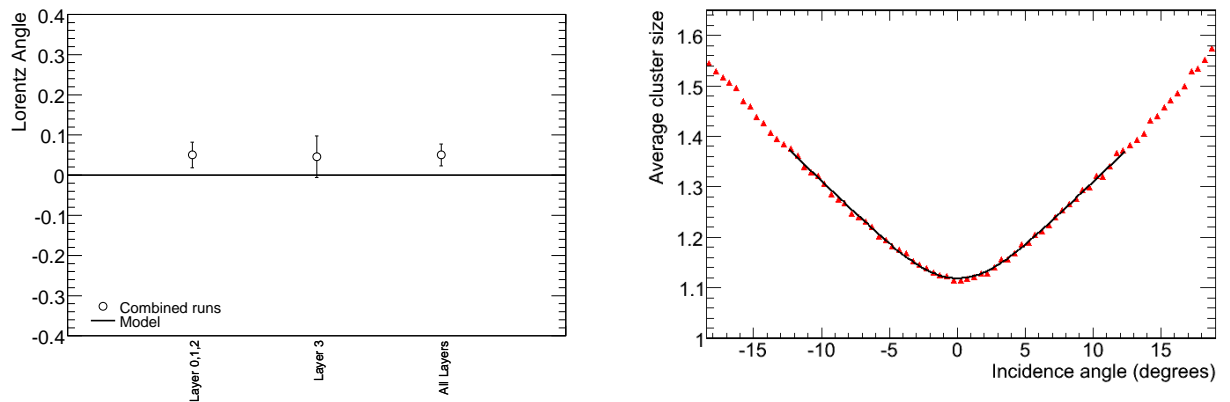
Figure 4.13: *Left: Lorentz Angle value calculated for Layers 0-2, Layer 3 and all the layers combined. Right: example of a fit to the average cluster size as function of the incidence angle for cosmic runs with no B field: the minimum is clearly around zero degrees.*
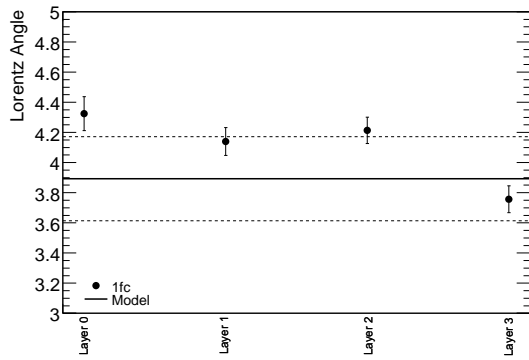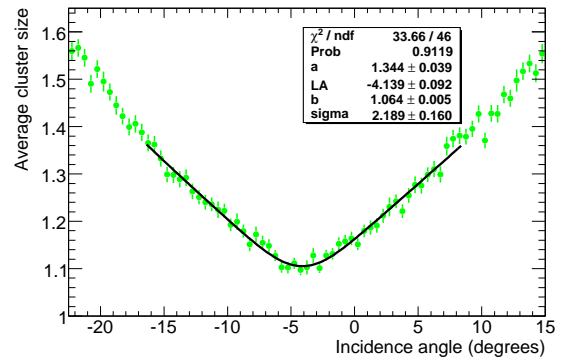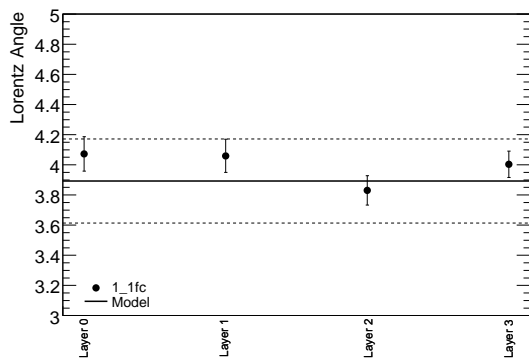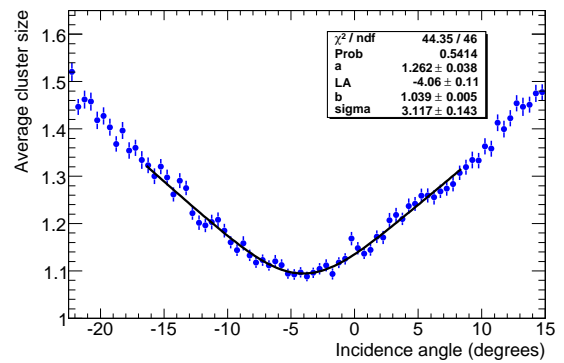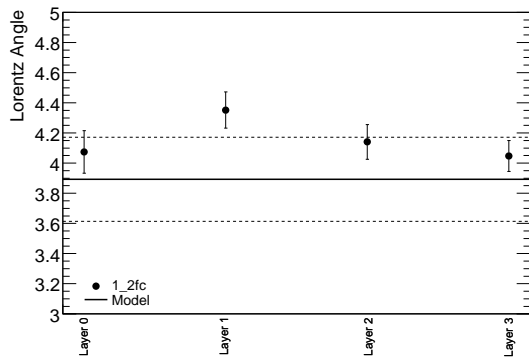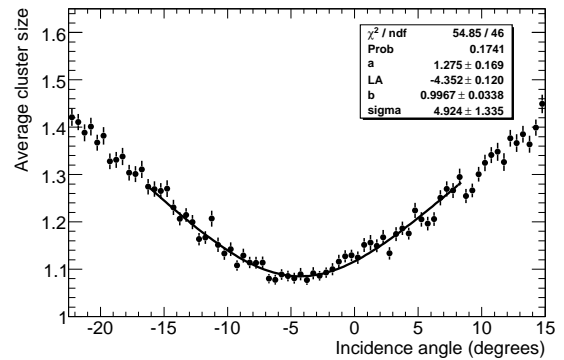
Figure 4.12: *Left column: Lorentz angle values as a function of layer, for runs with a threshold cut of 1 fC (a), 1.1 fC (b) and 1.2 fC (c). The right column presents example plots of the average cluster size as a function of the incidence angle, including details on the fitting curve, for Layer 1, for runs with a threshold cut of 1 fC (d), 1.1 fC (e) and 1.2 fC (f).*

Run	date (in 2010)	duration	# events
145720	Feb 02	11h 26m	359,771
145829	Feb 03	10h 44m	3,671,549
146046	Feb 06	11h 18m	508,686
146049	Feb 07	8h 19m	377,430
146054	Feb 07	9h 35m	433,367

Table 4.5: *List of cosmic runs taken between in February 2010 with no magnetic field used for the null test.*

The values for the Lorentz angle extracted from these runs are as follows:

	ϕ_L (°)
Layer 0,1,2	0.05 ± 0.03
Layer 3	0.04 ± 0.05
Overall	0.05 ± 0.03

As expected from runs with the B field off, these values are compatible with zero within the statistical uncertainty. B-off data are useful method to cross-check the analysis technique and the behaviour of the fitting function. Unfortunately, these runs suffer from low statistics and therefore it is harder to do a layer by layer analysis.

4.4   Collisions Data

As of 2009, the SCT started acquiring data from the collisions of protons. For the collisions data with $\sqrt{s} = 7$ TeV, the initial selection applied followed the Minimum Bias [4] analysis on first collision data, as listed below:

- $d_0 < 10$ mm;

- Transverse momentum, $p_T > 400$ MeV;

- Number of SCT hits > 6;

- Number of Pixel hits > 1.

However, since a large amount of collision events was available, it was necessary to study which selections to apply, in order to best study the Lorentz angle measurement.

[4]Minimum bias refers to the selection of inelastic events with the minimum possible trigger requirements necessary to ensure that an inelastic collision occurred. Minimum bias events are typically dominated by low transverse momentum and low particle multiplicity [54].

4.4.1   Event Selection Study

Impact Parameter, d_0

Figure 4.14 shows the distributions of the average cluster size as a function of the incidence angle for different bins of d_0, ranging from a larger d_0, to a d_0 as small as 1 mm.

For a d_0 further away from the collision point at 0, one can see a degradation in the information, for example, for the extreme cases of $1 = $ [-30,-5] and $6 = $ [5, 30]. The choice for d_0 was made such that:

$$d_0 < 1 \, \text{mm},$$

which corresponds to the best defined distribution and still a large amount of statistics.

Transverse Momentum

The transverse momentum of the track has also been studied, and as shown in Figure 4.15, for smaller p_T tracks, the incidence angle is very large and the region of the distribution where the Lorentz angle could be measured is not populated. So a necessary cut in the transverse momentum has been chosen such that:

$$p_T > 500 \, \text{MeV}.$$

Negative and Positive Tracks

A study has been made separating negative from positive tracks. Figure 4.16, shows a diagram of the modules, tilted by 11° with the positive (blue) and negative (red) tracks pictured hitting the modules (not to scale). It can be seen that the negative tracks contribute to a positive incidence angle and the positive tracks contribute to the negative incidence angles. The tracks intersect at around -10°, so, for the minimum cluster size, the Lorentz angle of -4° is dominated by the negative tracks. In Figure 4.17, is a set of distributions showing the contribution of the negative (red) and positive (black) for the incidence angle.

In this study, the selection applied, apart from the separation between negative and positive tracks, is: $d_0 < 1$ mm, $p_T > 500$ MeV, number of SCT hits and number of Pixel hits > 1. The value around the minimum cluster size can be perfectly measured using only the negative tracks, as can be observed. In fact, seeing that the fit is better for a smaller interval, the contribution from the positive tracks worsens the fit. Thus, it has been decided to consider only the negative tracks for the determination of the Lorentz angle.
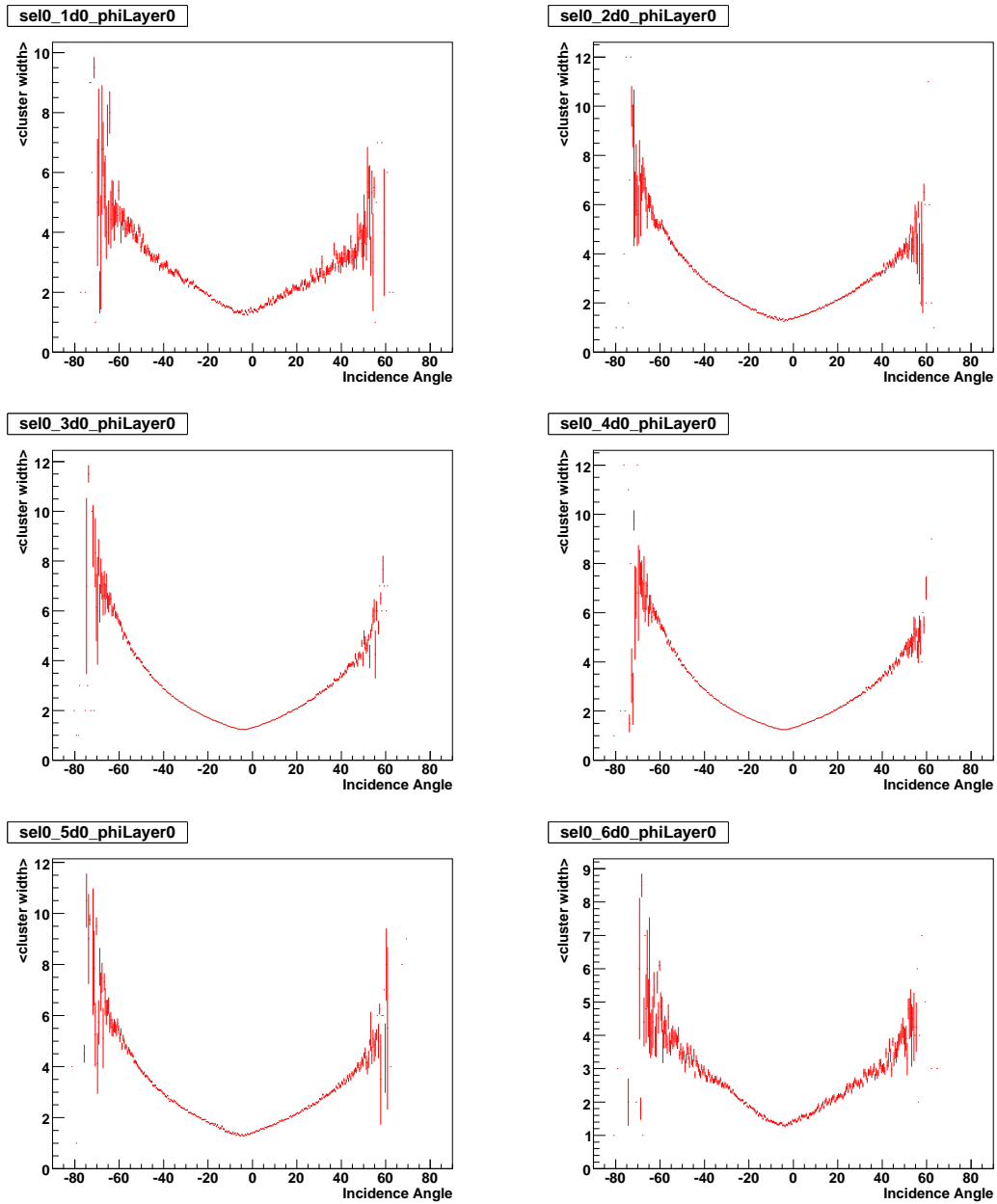
Figure 4.14: *Layer 0 average cluster size as a function of incident angle for different bins of impact parameter d_0. The ranges of d_0 bins are (in mm) from top-left to bottom-right: 1 = [-30,-5], 2 = [-5, -1], 3 = [-1, 0], 4 = [0, 1], 5 = [1, 5], 6 = [5, 30]. No other cuts are applied to the tracks selected in these plots.*
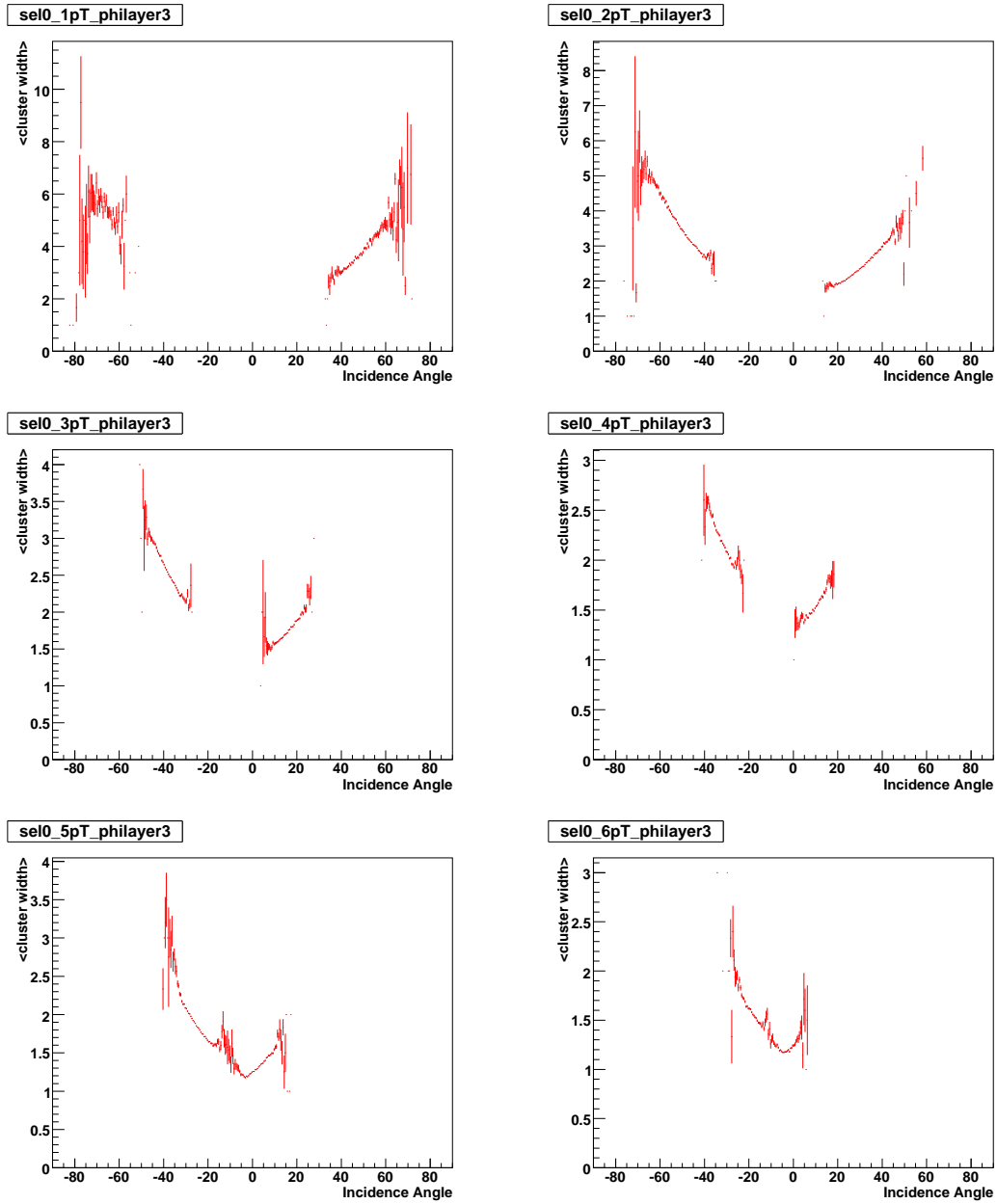
Figure 4.15: *Layer 3 average cluster size as function of incident angle for different bins in transverse momentum. The ranges of p_T bins are (in MeV) from top-left to bottom-right: 1 = [100, 200], 2 = [200, 300], 3 = [300, 400], 4 = [400, 500], 5 = [500, 1000], 6 = [1000,1500]. No other cuts are applied to the tracks selected in these plots.*
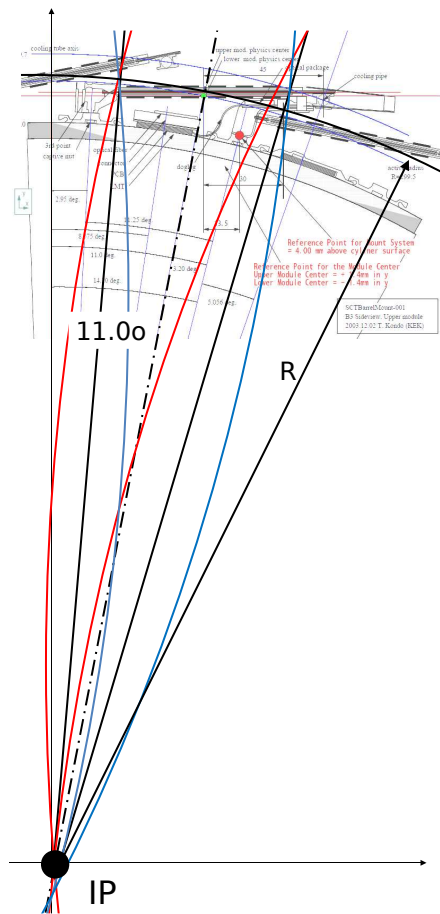
Figure 4.16: *schematic drawing showing the trajectories of positive and negative tracks with respect to the SCT barrel geometry [50].*

Fitting Range Studies on Collisions Data

The choice of the fitting range has been made using data from the cosmic ray runs [51]: the optimal range was found to be $\pm 12.5°$ around the minimum of the distribution. With collisions data available and the selection defined previously, the study was thus repeated for negative tracks only.

For collisions data, the distribution of the incidence angle varies between -30° and 60°, as a function of the average cluster width, hence being asymmetric. So an asymmetric fitting range is considered. The lower bound of the fitting range is varied between -10° and -6°in steps of 1°, whereas the upper bound is varied between -2° and 8° in steps of 2°.

Figure 4.18 (a) shows an example of the Lorentz angle values for the fit between -9° and $x°$, where $x = -2°, 0°, +2°, +4°, +6°, +8°$. The same Figure 4.18 (b) shows
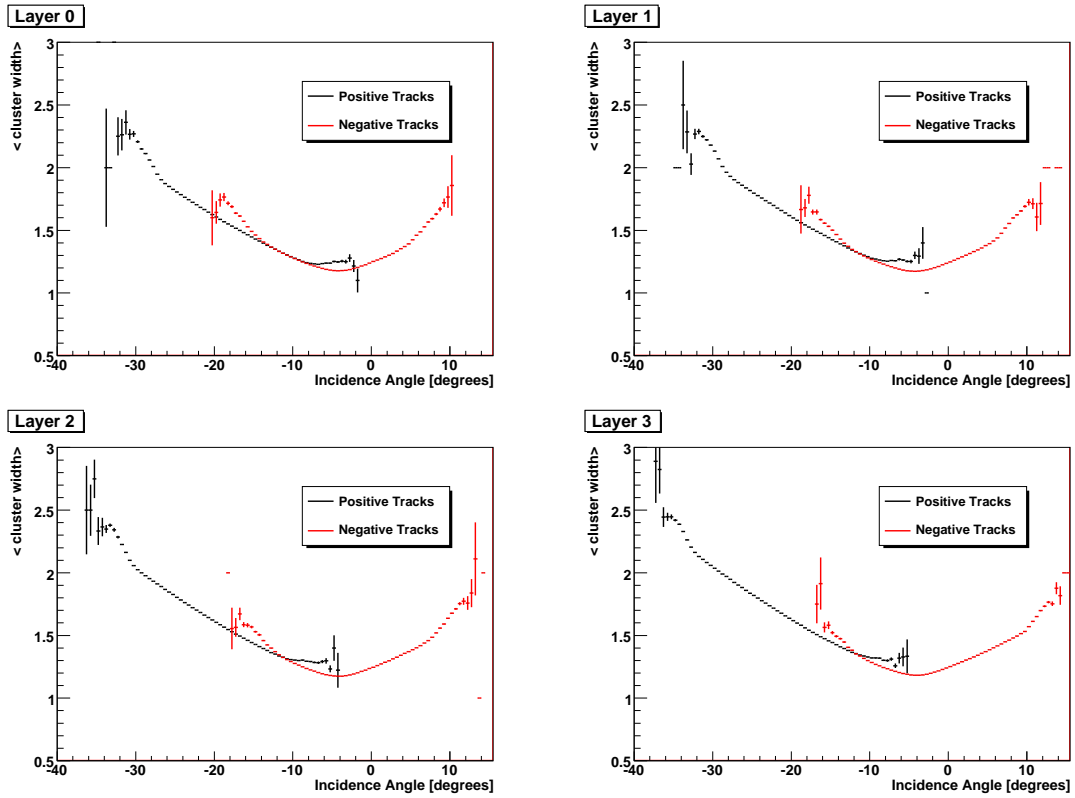
Figure 4.17: *Set of plots for positive and negative tracks study. The cluster size as a function of the incidence angle in the four SCT layers is shown. Red points represent cluster sizes from negative tracks, while black points correspond to positive tracks.*

the fit parameters, slope, minimum cluster, σ and χ^2/DoF for each range considered and from the distribution of the χ^2/DoF. Fit ranges such as $[x,6°]$, or $[x,8°]$, can be excluded, as the values are large and don't define the fit well. The ranges with a smaller upper bound have a reasonable χ^2/DoF, however, ranges ending in -2° or 0° are rather small and close to the minimum, which is a risky fitting limit. So, within the range of an upper limit of 2°, the range $[-9°,2°]$ has been chosen, which presents the best χ^2/DoF.

Figure 4.19 (a) and (b) show the average cluster size as a function of incidence angle for a chosen range of $[-9°,2°]$ and for a range of $[-7°,8°]$, respectively. A complete set of plots for all the considered fitting ranges, for Layer 0, can be found as an Appendix in [50].

Fitting Range Studies on Monte Carlo

For the Monte Carlo simulation, the same study was conducted. Since the Lorentz angle value measured in collision data and in simulation is different, a different fitting
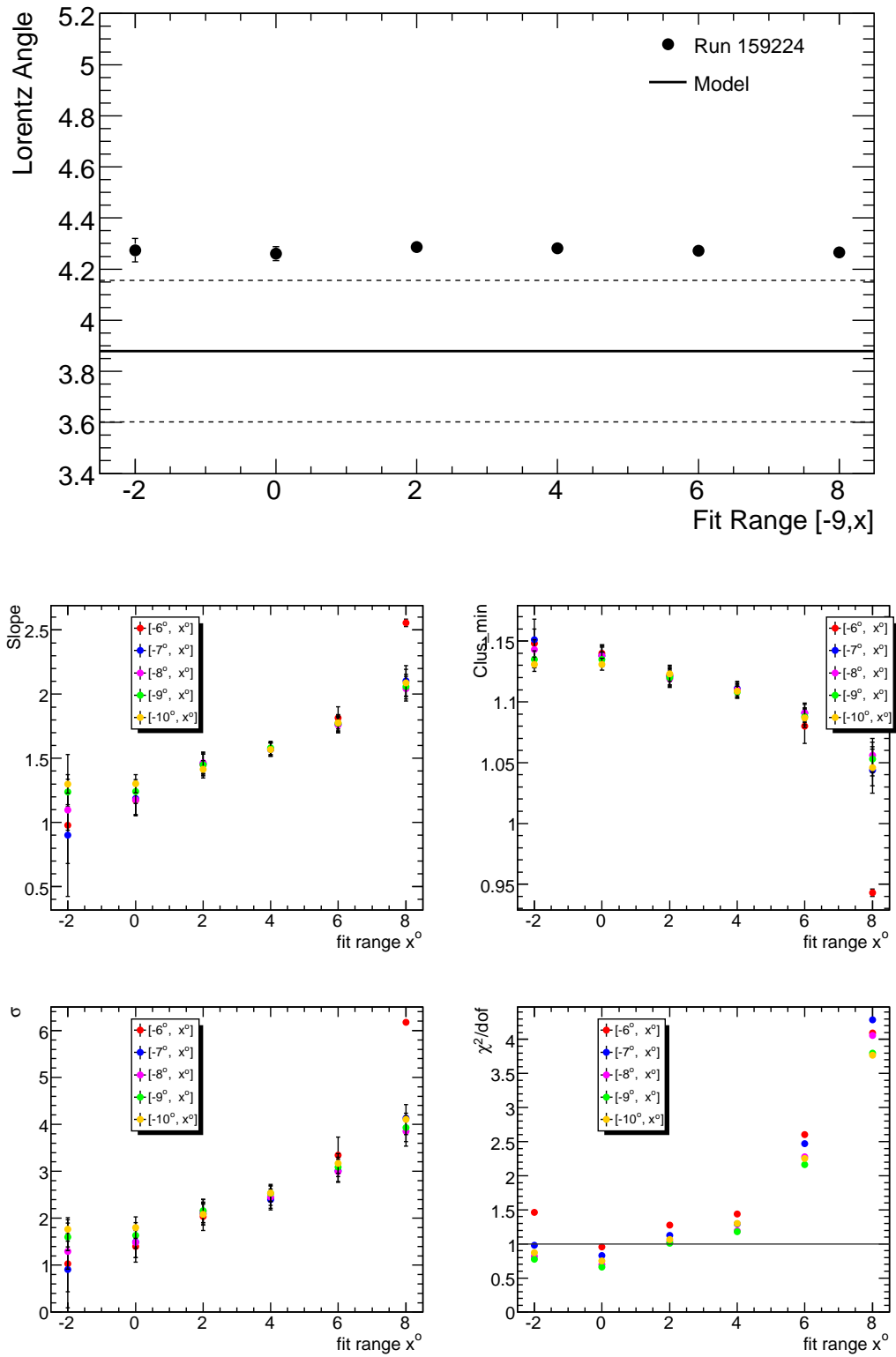
Figure 4.18: *Plots from the fitting range optimisation for Layer* 0 *on collision data. (a) Lorentz angle value as a function of the tested fit ranges with a lower bound of* −9° *and variable upper bound x. (b) The other three parameters of the fit function and the fit* χ^2 *as a function of the fit ranges tested.*
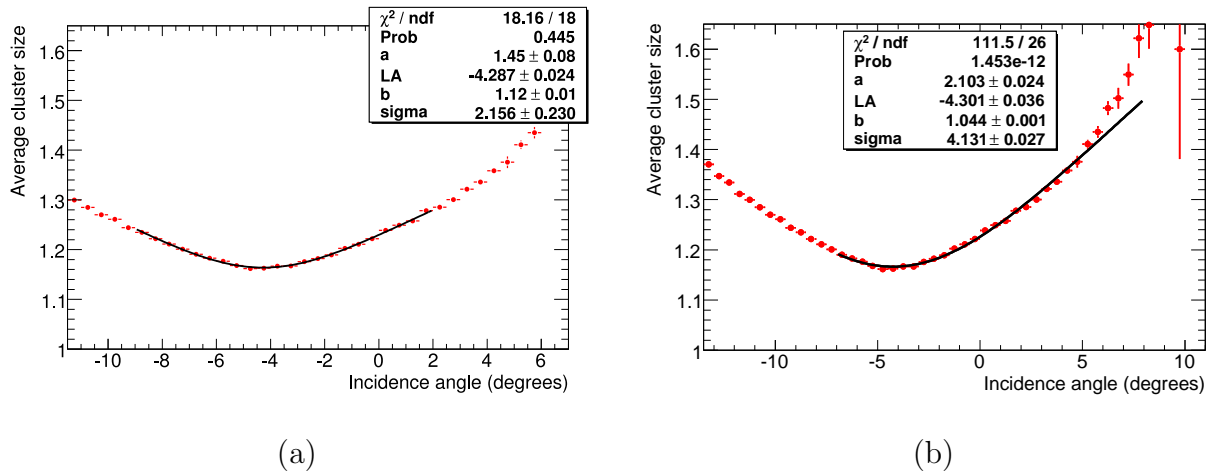
Figure 4.19: *(a) Example of the distribution of average cluster size as a function of incidence angle. The fitting function is shown for a fitting range of [-9°, +2°]. This is the chosen fit range to be used in the study of the Lorentz angle in 7 TeV collision data. (b) Another example of the distribution to be fitted in order to extract the Lorentz angle. The fit is shown using the fitting range [-7°, +8°] [50].*

range may be applied.

Figure 4.20 shows the Lorentz angle values for the different ranges applied ((a) and (b)) and examples ((c) and (d)) of the distributions fitted within one of the ranges shown above.

Similar conclusions can be drawn from the Monte Carlo study as for the collision data analysis: the value of the Lorentz angle does not change when varying the fit range, but the other fit parameters, shown in Figure 4.21, are less stable, hinting to a sub-optimal fitting function. From the χ^2/DoF distribution, the optimal fit range to be used in Monte Carlo studies for the Lorentz angle determination is chosen to be $[-8°, 0°]$: the fitted distribution is shown in Figure 4.20 (d). This range is different than the one chosen for data due to the fact that the Lorentz angle value determined for the MC simulation is lower than in data (cf. Figure 4.30).

As a summary, here is the selection chosen for the collisions data, in view of improving the Lorentz angle measurement:

- $d_0 < 1$ mm;

- $p_T > 500$ MeV;

- Fitting range: [-9°,2°] ([-8°, 0°] for Monte Carlo);

- Track charge < 0.
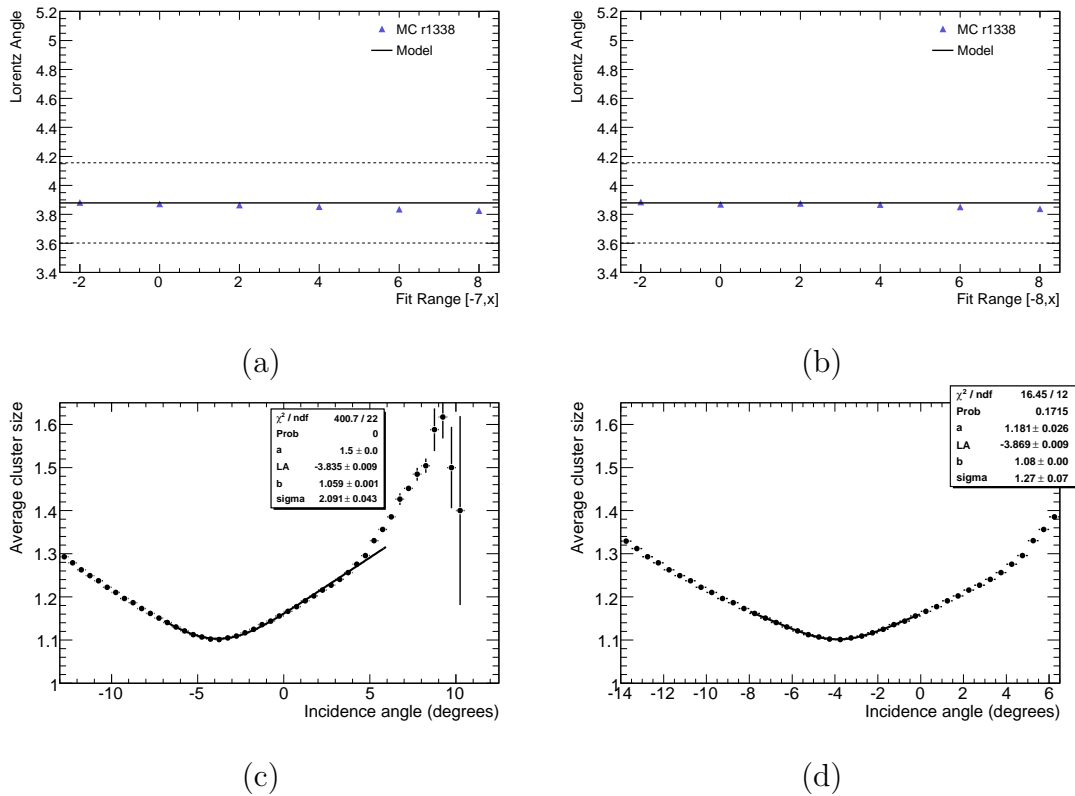
Figure 4.20: *Plots from the fitting range optimisation for Layer 0 on Monte Carlo data. (a) Lorentz angle value as a function of the fit ranges with a lower bound of $-7°$ and variable upper bound x. (b) Same as (a) with the ranges [-8°, x]. (c) Example of the distribution of average cluster size as a function of the incidence angle. The fitting function is shown for a fitting range of [-7°, +6°]. (d) Another example of the distribution to be fitted in order to extract the Lorentz angle. The fit is also shown with the fitting range [-8°, 0°]. This is the chosen fit range to be used in the study of the Lorentz angle in MC data.*

4.5 Region Dependence of the Modules

Due to the large amount of collision events available, the SCT module can be studied through the Lorentz angle value in more detail.

A study has been performed by dividing each module of the SCT Barrel into 12 equal rectangular regions and determining the Lorentz angle in each region separately. Figure 4.22 (a) shows how the modules are divided into regions with respect to their local coordinates *LocX* and *LocY* [5].

---

[5]*(LocX, LocY, LocZ)* is the local coordinate frame on the Barrel modules of the SCT [55]: the origin of the frame is the centre of the module; *LocX* and *LocY* are defined in the plane of the module and are parallel to the symmetry axis of the module.
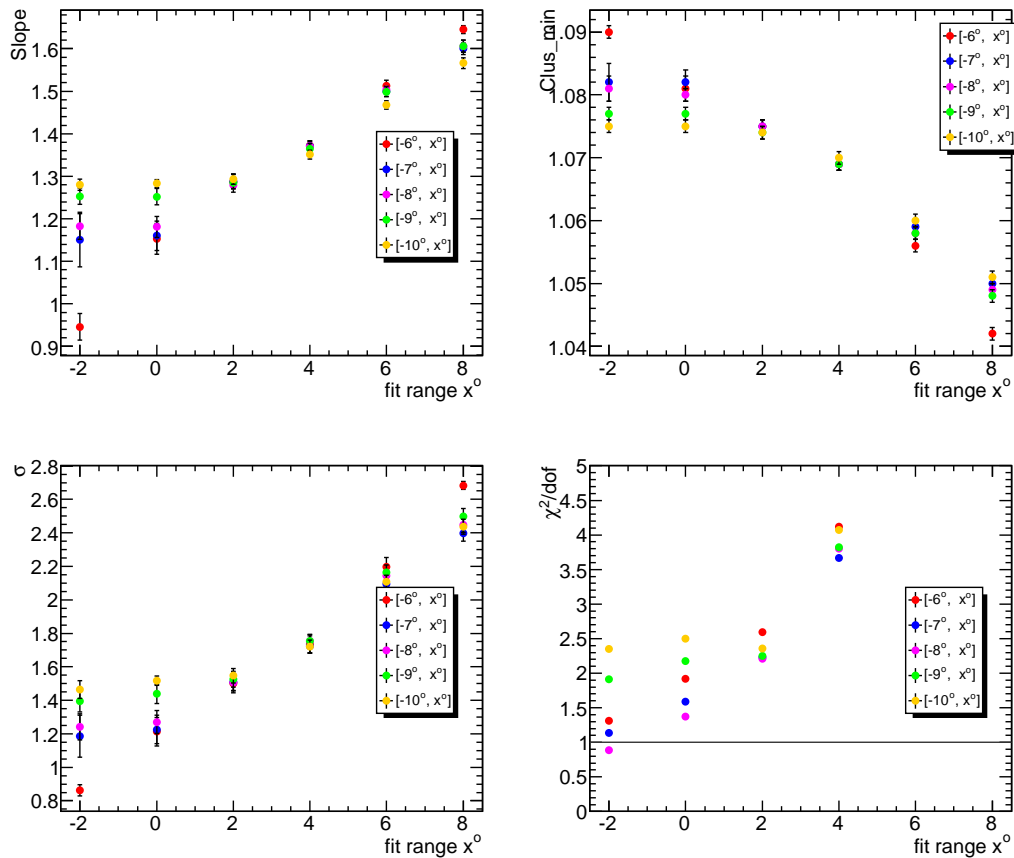
Figure 4.21: *Three parameters of the fit function: slope, minimum cluster size, σ and the fit χ^2/DOF as a function of the fit ranges tested [50].*
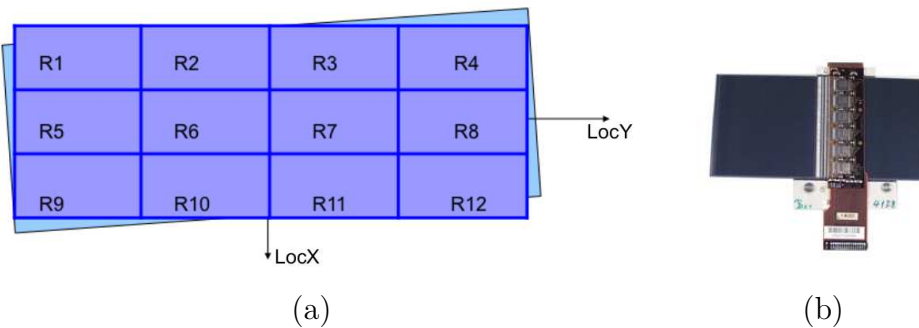
Figure 4.22: *(a) Scheme of the region division along the LocX and LocY coordinates, (b) Picture of a Barrel module of the SCT.*

The distributions of the average cluster size as a function of the incidence angle are studied in each region individually. This is shown here for run 153656, acquired in April 2010, but other runs have also been studied.

Figure 4.23 shows the regions regrouped with the same *LocX*, for Layer 1. The first feature to be observed is that a small peak can be found in all three distributions (a), (b) and (c). This peak is at the same incidence angle for equal *LocX*, but varies with different *LocX*. Therefore, the peaks occur at three different incidence angles. The slope and the range of the distribution also vary with the *LocX*.

(a)

(b)

(c)
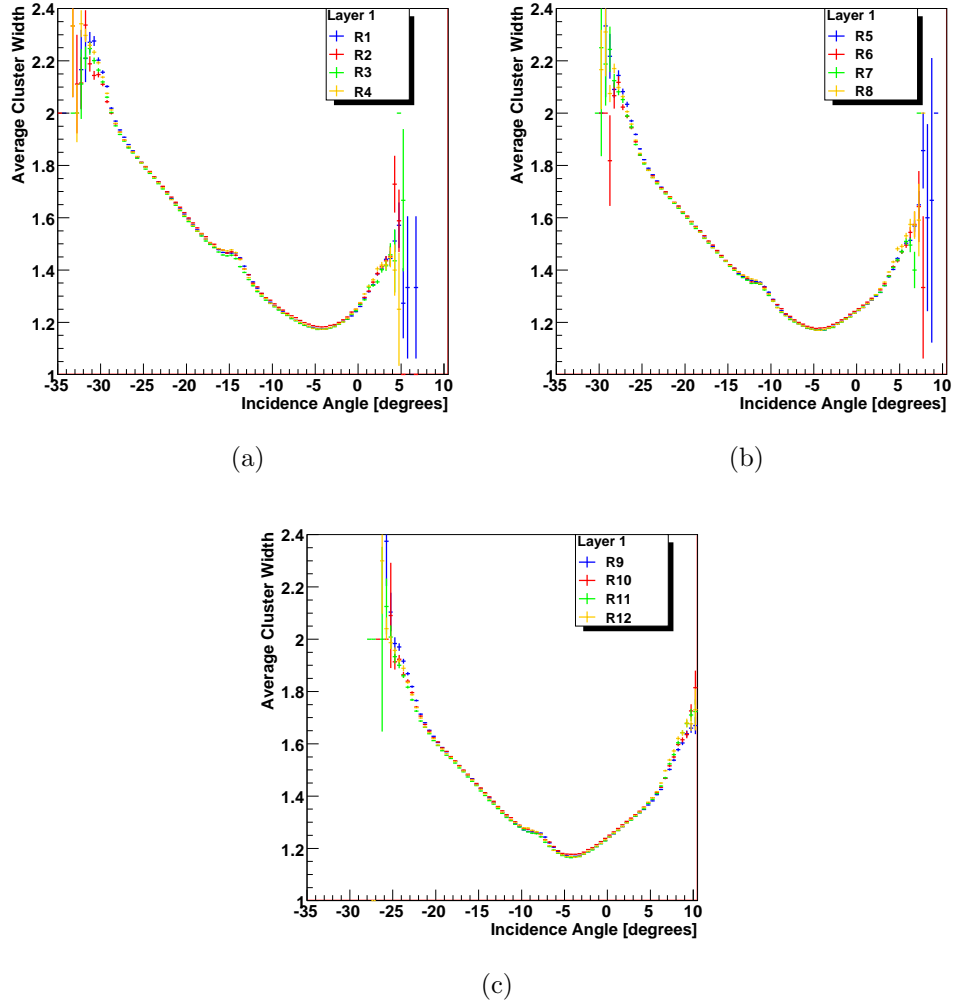
Figure 4.23: *Average cluster size as a function of the incidence angle for Layer 1: comparison between the twelve regions of the module. Each plot refers to a different region in LocX. Within the same plot, the contribution of four regions in LocY are plotted. (a) Regions 1, 2, 3 and 4. (b) Regions 5, 6, 7 and 8. (c) Regions 9, 10, 11 and 12 [50]. The region numbers refer to the diagram on Figure 4.22.*

Figure 4.24 shows the behaviour of the average cluster size as a function of the incidence angle for the four different *LocY* regions. Top row is from collisions data and bottom row is from Monte Carlo simulated data. In each plot there are the three peaks corresponding to the three different regions in *LocX*.
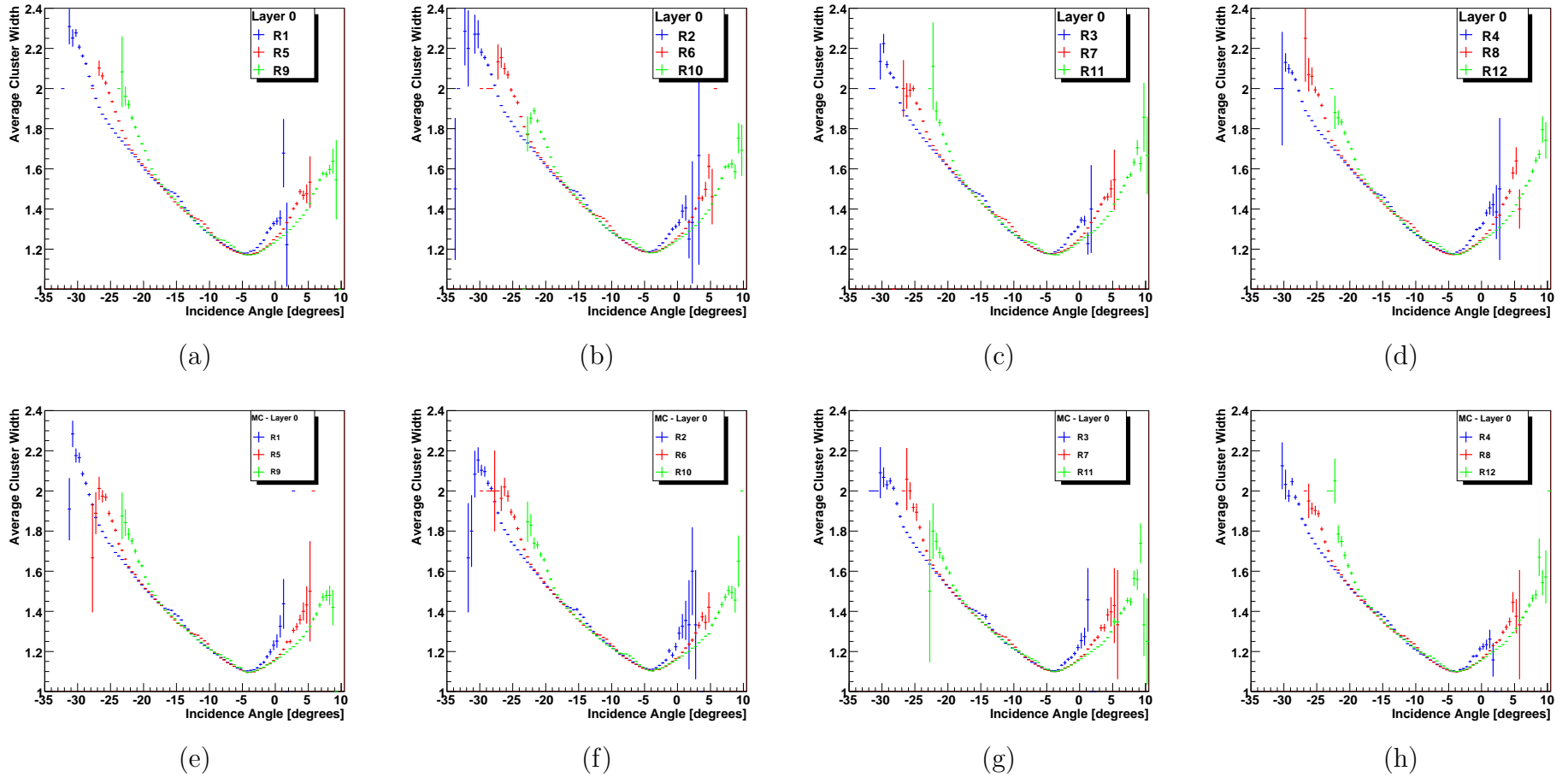
Figure 4.24: *Average cluster size as a function of the incidence angle for Layer 0 for different regions of the module. In each plot, the same region in LocY is considered. Within the same plot three different LocX regions are plotted together for comparison. Top row: (a) Regions 1, 5 and 9. (b) Regions 2, 6 and 10. (c) Regions 3, 7 and 11. (d) Regions 4, 8 and 12. Bottom row are the respective distributions for Monte Carlo simulation (e), (f), (g) and (h) [50]. The region numbers refer to the scheme in Figure 4.22.*

These peaks occur due to the kinematics of the tracks transversing the SCT Barrel modules and their geometry and tilt angle. Such a feature has not been observed so far because, when the average of all regions is made, the peaks also average up and disappear. Furthermore, if a track comes from the IP, for each region in *LocX* there is a different range of the track momentum, at the same incidence angle.

Hence, as can be explained by Figure 4.26, for a positive track (a) for the same incidence angle but increasing $LocX$, the p_T of the track increases, which leads to an increase in the deposited charge, resulting in a bigger cluster size. For a negative track (b), the reverse is true: for increasing $LocX$, the p_T decreases, which results in a smaller cluster size. Figure 4.25 shows the division into negative and positive tracks for one region (R1) and the combined track. It is observed that the peak is created at the intersection between the positive and negative tracks.
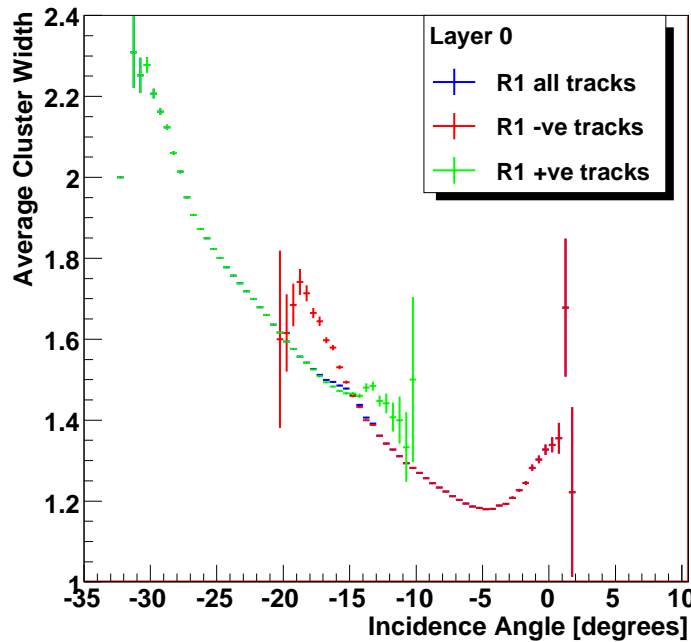
Figure 4.25: *Example of how negative and positive tracks contribute to the distribution generating the peak. Region 1 for modules of Layer 0 is shown.*

As for the value in the Lorentz angle, it also changes with the $LocX$. Figure 4.27 shows the Lorentz angle for each of the 12 regions for each layer of the SCT Barrel. The Lorentz angle is always bigger for the regions of smaller $LocX$. Layer 0 (top left plot) shows the most pronounced difference with the $LocX$.

(a)　　　　　　　　　　　　　　　(b)
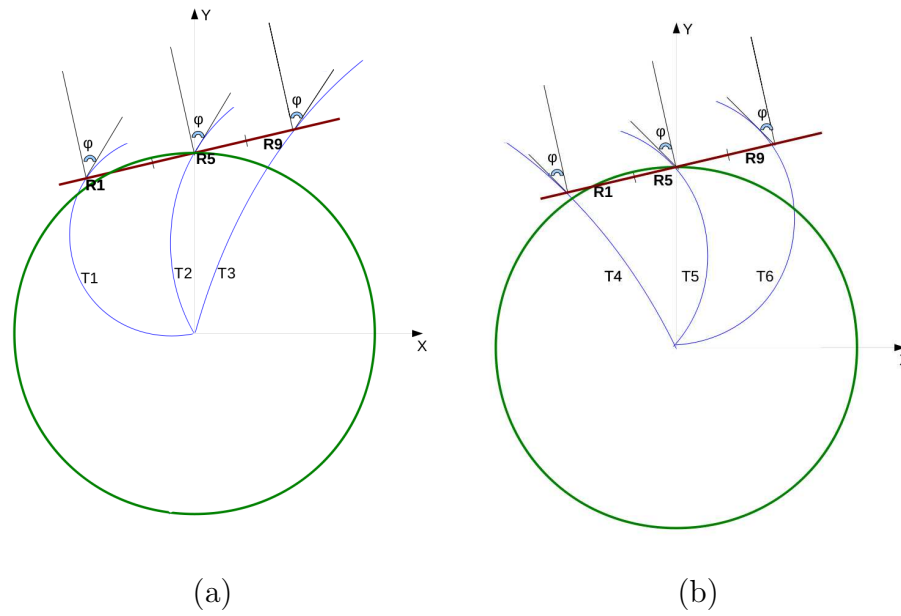
Figure 4.26: *Schematic showing three tracks passing through the module at three different LocX with same incidence angle ϕ. The transverse momentum of the tracks increases as the LocX coordinate increases. (a) shows positive tracks, (b) shows the case of negative tracks [50].*

(a)　　　　　　　　　　　　　　　(b)

(c)　　　　　　　　　　　　　　　(d)
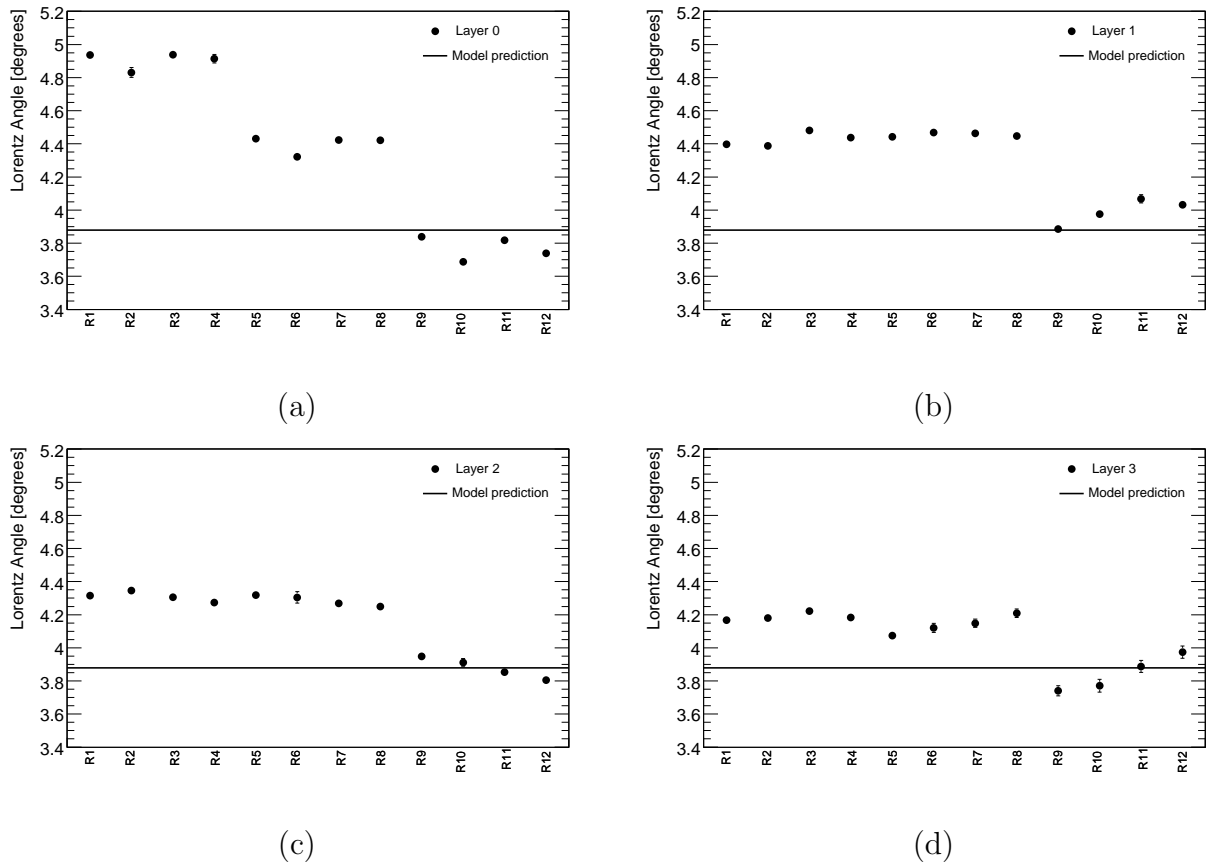
Figure 4.27: *Lorentz angle measured in collision data for each of the twelve regions of the module. Each plot refers to a different layer of the Barrel of the SCT.*

For the other layers, the difference of the value with the *LocX* is not so evident. This can be explained by the fact that these layers are further away from the IP, thus some tracks overlap. The full line is the model prediction.

(a)   (b)

(c)   (d)
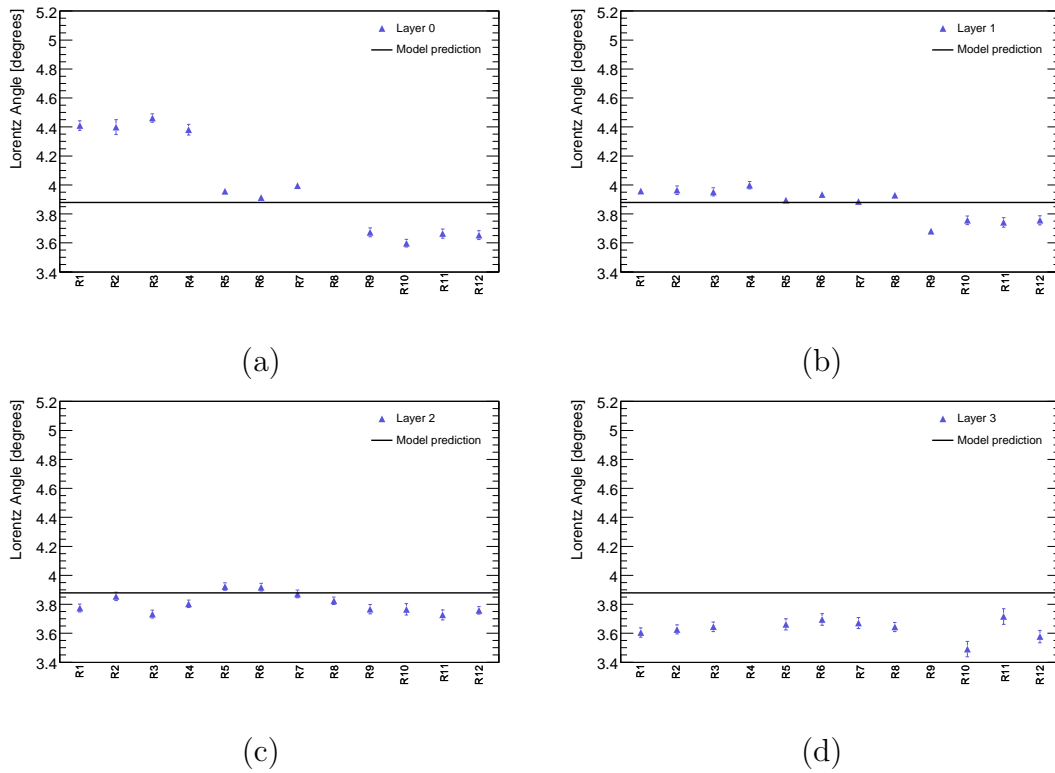
Figure 4.28: *Lorentz angle measured in Monte Carlo data for each of the twelve regions of the module. Each plot refers to a different layer of the Barrel of the SCT.*

Figure 4.28 shows the Lorentz angle results for the Monte Carlo simulated data analysed. From these plots, it is clear that the value for the Lorentz angle is smaller at all times with respect to the corresponding data collisions value. The Monte Carlo calculation is done following the digitisation model, as previously mentioned, so it is logical that its value approaches the Lorentz angle model prediction. The collision data show that the predicted Lorentz angle is lower than the actual value, but it is still unknown why.
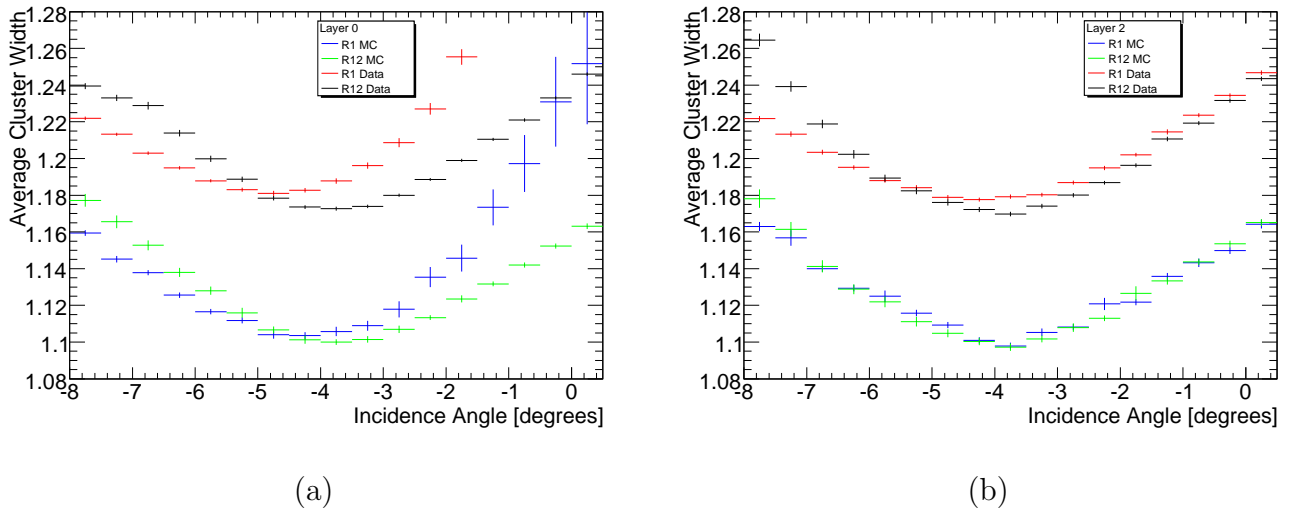
Figure 4.29: *Distributions of average cluster width as function of incidence angle: (a) Data-Monte Carlo comparison for Layer 0 for two opposite module regions: regions R1 and R12. (b) is for Layer 2.*

Figure 4.29 shows a zoom over the average cluster size as a function of the incidence angle, for two opposite regions, R1 and R12, and for both data and MC. The difference in the minimum cluster size can be clearly observed. It is also clear that in the Monte Carlo, although the slope does change, the minimum does not shift for the two extreme regions.

4.6   Results

The 7 TeV collision runs used are from the MINBIAS stream, acquired from March 2010 onwards. They are:

- 152166, 152221, 152345, 152409, 152441, 153565, 155160, 159086, 159224, 162882, 165591.
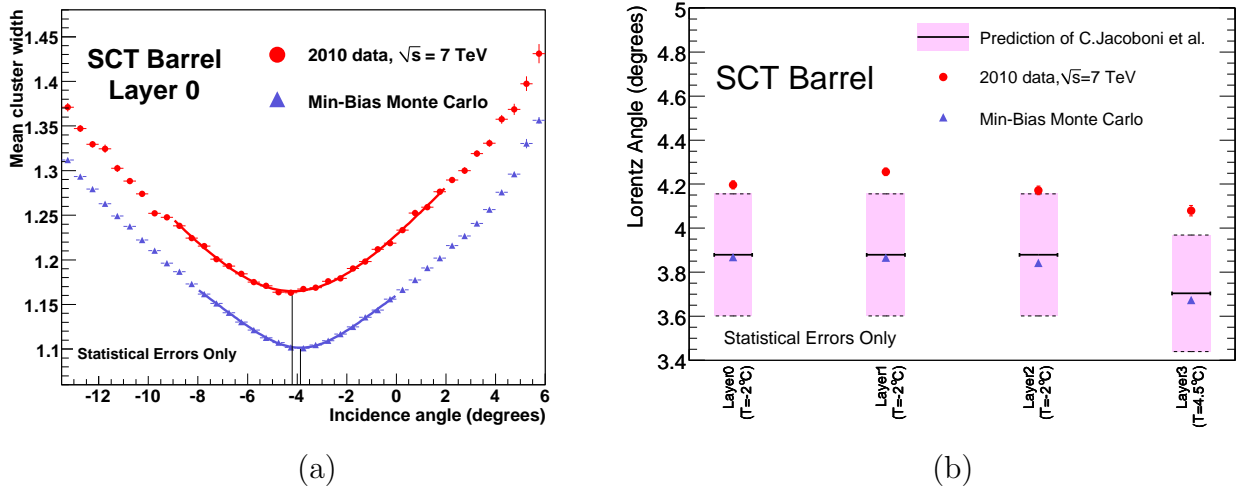
Figure 4.30: *(a) Example of a fitted profile of the average cluster size vs the incidence angle on both collision and simulated data. (b) The Lorentz angle values for all the SCT Barrel layers and both collision and simulation data.*

In Figure 4.30 results are shown for the Lorentz angle for collision data and for Monte Carlo simulation.

On the right plot, where the Lorentz angle is shown by layer, it is clear that the model is not in agreement with the results given by collision data. The simulation does agree with the model prediction, since it is generated based on such a model. The left distribution clearly shows the difference in the minimum of the cluster size, not only at a different incidence angle but also a different magnitude. Table 4.6 contains the values corresponding to collision data.

Run 167576	Lorentz angle value
Layer 0	-4.197 ± 0.018
Layer 1	-4.256 ± 0.018
Layer 2	-4.172 ± 0.021
Layer 3	-4.079 ± 0.024

Table 4.6: *The Lorentz angle values for all the layers in the collision run 167576, with statistical errors only. These values correspond to the points in Figure 4.30 (b).*

Other runs have been analysed and as can be observed from Figure 4.31, the results are all consistent. It is shown the Lorentz angle for several runs for all four layers in the SCT Barrel. All collisions data values are above the model prediction and its uncertainty.
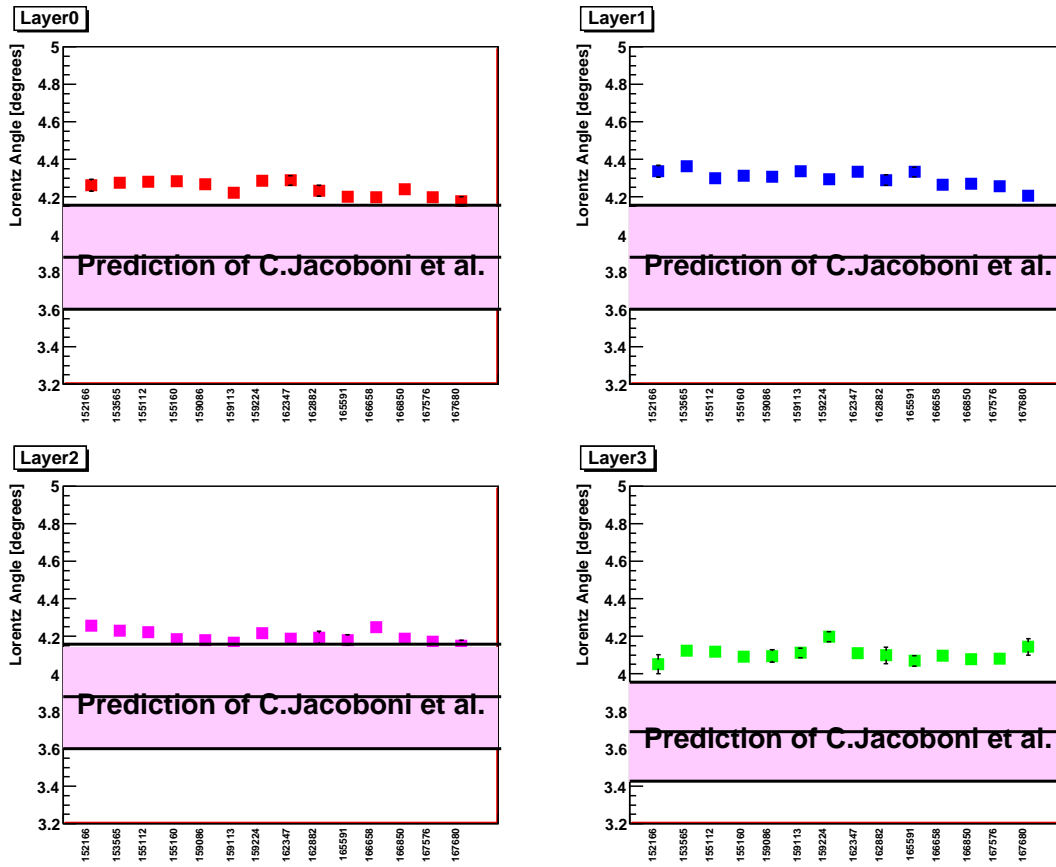
Figure 4.31: *Lorentz angle measured in each of the collision data runs considered in this study. From left to right and from top to bottom: Lorentz angle value as a function of the run number in Layer 0 to 3. The band represents the model prediction with its uncertainty as discussed in Section 4.2.1 [50].*

4.7 Conclusions

In this chapter, studies related to the calculation of the Lorentz angle in the SCT have been presented.

Recent literature suggests a change in the uncertainty value, however with the models available to determine the value of the drift velocity, such change is unjustified.

Studies were also made using cosmic rays data. Data has been acquired with voltages in Layer 2 of the Barrel different than the nominal one, at 150 V, from a minimum of 30 V to 350 V. As expected, the Lorentz angle depends on the voltage and different values are obtained. Also it is observed that data runs acquired in different periods with the same nominal voltage (150 V or 300 V were available for comparison), show a different Lorentz angle value. Looking at the θ angle (normal

to the Lorentz angle) reveal a different shape in θ, however it does not depend on the Lorentz angle. Unfortunately no more runs are available to pursue this study further.

Consistency tests were made using cosmic rays data: a variation of the threshold selection for the collected charge does not influence the Lorentz angle value; by turning the magnetic field off the Lorentz effect ceases to exist and the Lorentz angle value is consistent with zero.

With the collisions data available for $\sqrt{s} = 7$ TeV, it was necessary to define certain selection cuts for the tracks to better improve the results, since a large amount of statistics were present. The studied quantities are the impact parameter, the transverse momentum and the charge of the tracks. The fitting function used is improved by decreasing the range of the incidence angle that should be fitted. Different values for the optimal fitting range are found for the collisions data and the Monte Carlo simulated data. The reason for the difference in the range is caused by the fact that the minimum cluster size occurs at a different magnitude and different incidence angle for collisions data and Monte Carlo. As a consequence, the Lorentz angle value for simulation does not agree with that from data. Such disparity is still being studied and it may result in changes to the digitisation model for the SCT.

As a final study, the Lorentz angle is calculated individually for twelve regions of the SCT Barrel module. The value changes according to the position on the module and the distribution of the average cluster size as a function of the incidence angle reveals a peak at an angle near to the intersection of the positive with negative tracks. Such peak is due to the kinematics of the tracks and the geometry of the module.

The fact that the Lorentz angle measured from collision data deviates from the model prediction, is maybe an indication that the model needs to be rethought. Between different data runs the Lorentz angle has remained consistent throughout, so it may be concluded that such measurement is robust and may be used to control the operation of the SCT.

Chapter 5

t-Channel Cut Based Analysis

In this chapter, the data and Monte Carlo simulation samples are presented. The scaling necessary for the Monte Carlo simulation to agree with the data is described. The analysis to determine the t-channel cross section is presented. Demanding selection cuts are implemented and a selection of discriminant variables is described. A binned likelihood fit on the top invariant mass is done to calculate the cross section.

5.1 Data And Simulation Description

5.1.1 Data

The data considered for the main analysis has been acquired during the 2011 proton-proton running, with a total luminosity of 4.7 fb^{-1}. This data is divided into runs, which are blocks of continuous data acquisition and go from periods B to M. The different periods are marked by a change in conditions, whether an improvement or a fault in the detector or a change in the bunch spacing or an additional trigger menu (list of signatures that trigger the acquisition of an event). The runs are part of the Good Runs List (GLR), which indicate that all data acquired has the maximum quality on all sub-detectors, with the full ATLAS detector ON.

Relevant Triggers

The trigger naming convention is to use the trigger level and then the threshold, for example, a `EF_e20_medium` refers to an electron trigger with E$_T$ > 20 GeV at EF and medium identification required. For the electrons, the triggers applied were [56] `EF_e20_medium`, for periods B-H, `EF_e22_medium` for periods I-K and `EF_e22vh_medium1` for periods L-M. This last menu accounts for the increase in the luminosity (called the V3 chain), includes a hadronic core veto (the "h" in the name) and has a tighter selection than the medium menu [57].

Process	Cross Section [pb]	k-factor	Generator	N$_{events}$
t-channel (e+jets)	6.94	1.0	AcerMC+Pythia	700,000
Wt (all decays)	15.74	1.0	MC@NLO+Herwig/Jimmy	800,000
s-channel (e+jets)	0.498	1.0	MC@NLO+Herwig/Jimmy	250,000
t$\bar{t}$ no fully hadronic	80.1	1.12	MC@NLO+Herwig	12,500,000

Table 5.1: *Monte Carlo samples names, cross sections and number of generated events for the top quark processes. The cross sections include the decay branching ratios. The k-factor accounts for NNLO corrections.*

5.1.2   Simulation

The background and signal simulation samples are given by the Monte Carlo MC11c samples which correspond to the 2011 reprocessing with Athena Releases 17.0.X.Y. The MC11c uses the Pythia6 pile-up information and the simulation, digitization and reprocessing tag GEO-18-01-01. Both data and MC are produced with the reprocessing tags p937 corresponding to the production around June 2012.

Signal and Background Normalisation

The signal and background MC samples are normalised to the luminosity of the data (4.7 fb^{-1}). Additional scales are determined later for the the W+jets and W+heavy flavour samples, since their compositions are not accurately known and simulated.

The luminosity of each sample can be calculated knowing the channels' cross sections and the number of generated events. Table 5.1 indicates the top samples used and their parameters, including which generators are used. As for the remaining background processes, they are indicated in Table 5.2. The k-factor accounts for NNLO corrections.

Generators

Each sample is generated with a combination of generators. Some generators are specific to the channel whereas others are more generic and help to complete the simulation of the hard event, adding initial and final state radiation, hadronisation and decays.

As can be observed in Table 5.1, all top background is generated with MC@NLO [58] generator 4.10 with the CT10 [59] parton distribution functions (PDF) and for parton shower and underlying event, HERWIG v6.50 [60] and JIMMY v4.31 [61] using the same PDF. However, due to a modelling deficiency in the MC@NLO and HER-WIG setup, for the t-channel signal, the AcerMC generator [62] is used, alongside

Process	Cross Section [pb]	k-factor	Generator	N_{events}
Z→ ee + 0 partons	668.4	1.25	Alpgen+Herwig	8,000,000
Z→ ee + 1 parton	134.4	1.25	Alpgen+Herwig	2,000,000
Z→ ee + 2 partons	40.4	1.25	Alpgen+Herwig	734,000
Z→ ee + 3 partons	11.2	1.25	Alpgen+Herwig	300,000
Z→ ee + 4 partons	8.4	1.25	Alpgen+Herwig	78,300
Z→ ee + 5 partons	0.8	1.25	Alpgen+Herwig	25,000
W→ eν + 0 partons	6931.3	1.20	Alpgen+Herwig	3,500,000
W→ eν + 1 parton	1305.3	1.20	Alpgen+Herwig	2,500,000
W→ eν + 2 partons	378.0	1.20	Alpgen+Herwig	3,750,000
W→ eν + 3 partons	101.9	1.20	Alpgen+Herwig	1,000,000
W→ eν + 4 partons	25.7	1.20	Alpgen+Herwig	250,000
W→ eν + 5 partons	7.0	1.20	Alpgen+Herwig	70,000
W→ $\ell\nu$ + $b\bar{b}$ + 0 partons	47.35	1.20	Alpgen+Herwig	475,000
W→ $\ell\nu$ + $b\bar{b}$ + 1 parton	35.76	1.20	Alpgen+Herwig	205,000
W→ $\ell\nu$ + $b\bar{b}$ + 2 partons	17.33	1.20	Alpgen+Herwig	175,000
W→ $\ell\nu$ + $b\bar{b}$ + 3 partons	7.61	1.20	Alpgen+Herwig	70,000
W→ $\ell\nu$ + $c\bar{c}$ + 0 partons	127.53	1.20	Alpgen+Herwig	1,275,000
W→ $\ell\nu$ + $c\bar{c}$ + 1 parton	104.68	1.20	Alpgen+Herwig	1,050,000
W→ $\ell\nu$ + $c\bar{c}$ + 2 partons	52.08	1.20	Alpgen+Herwig	525,000
W→ $\ell\nu$ + $c\bar{c}$ + 3 partons	16.96	1.20	Alpgen+Herwig	170,000
W→ $\ell\nu$ + c + 0 partons	644.4	1.52	Alpgen+Herwig	6,500,000
W→ $\ell\nu$ + c + 1 parton	205.0	1.52	Alpgen+Herwig	2,070,000
W→ $\ell\nu$ + c + 2 partons	50.8	1.52	Alpgen+Herwig	520,000
W→ $\ell\nu$ + c + 3 partons	11.4	1.52	Alpgen+Herwig	115,000
W→ $\ell\nu$ + c + 4 partons	2.8	1.52	Alpgen+Herwig	30,000
WW (all decays)	11.5	1.48	Herwig	2,400,000
WZ (all decays)	3.46	1.48	Herwig	1,000,000
ZZ (all decays)	0.97	1.48	Herwig	250,000

Table 5.2: *Monte Carlo samples used for the background in the analysis. Their designations, cross section, generator used and number of generated events are also presented.*

PYTHIA [63] which uses MRST LO as the PDF. The cross section normalisation values for the top processes are:

- $t\bar{t}$: 177^{+10}_{-11} pb, approximate NLO order prediction [64, 65, 66, 67, 68, 69];

- t-channel: 64.6 pb, NNLO prediction [24];

- s-channel: 4.6 pb, NNLO prediction [23];

- Wt production: 15.7 pb, NNLO prediction [25].

For the vector boson production (W+jets, W+heavy flavour, Z+jets), ALP-GEN [70] interfaced with HERWIG and JIMMY was used. The PDF used was CTEQ6.1 [71] A heavy flavour overlap removal tool is used to avoid double counting of heavy quark production [72]. The di-boson samples (WW, ZZ and WZ) are produced with ALP-GEN and HERWIG.

The parameters widely used by the generators are:

Parameter	value
Top Mass	172.5 GeV
W Mass	80.399 GeV
W Width	2.085 GeV
Z Mass	91.1876 GeV
Z Width	2.4952 GeV

The detector full simulation is done with GEANT4 [73] which is a tool to simulate the passage of particles through matter.

5.2 Objects Definitions and Reconstruction

This analysis is performed on the 2011 data acquired by ATLAS with a total luminosity of $\mathcal{L} = 4.7$ fb^{-1}. Both data and simulation samples are in the D3PD format. The definitions or corrections of the objects and scaling or smearing of energy follow the default recommendations of the Top working group.

5.2.1 Electrons

For single top events, one high transverse momentum lepton, in this case an electron, needs to be selected. At the trigger level, (at the initial L1 hardware level) an energy deposition of $E_T > 10$ GeV or $E_T > 12$ GeV, depending on the instantaneous luminosity (which increased throughout the data taking), is required. For the high level trigger EF, $E_T > 20$ GeV or $E_T > 22$ GeV is required.

The electron candidates are reconstructed using a cluster-based algorithm and the transverse energy is required to be $E_T > 25$ GeV, with $E_T = E_{cl}/\cosh(\eta_{track})$, where E_{cl} is the calorimeter cluster transverse energy and η_{track} is the pseudorapidity associated to the tracks in the inner detector. On an analysis level, the electron combined four-momentum is reconstructed with the cluster energy and the track information for the η and ϕ components. The calorimeter crack is taken into account by requiring the cluster η component to be $1.37 < |\eta_{cl}| < 1.52$.

Events with only one electron with $p_T > 25$ GeV, $|\eta_{cl}| < 2.7$ and no muons are chosen. Moreover the electron candidates must satisfy the high quality requirements set of cuts defined as *tight++*: the variables used are the acceptance of the detector, track quality (number of hits in the pixel and SCT, transverse impact parameter) and matching Inner Detector tracks with EM clusters; the *plus-plus* regimen is optimised for a higher pileup environment [74].

The background electrons originate from three different sources: hadrons faking electron signatures, electrons from heavy flavour decays and photon conversions. In order to reduce such backgrounds, the sum of the calorimeter cell energies within a cone of radius $\Delta R = 0.2$, excluding the cells at the centre associated to the electron (variable called Etcone20) [75], and the sum of the p_T of all Inner Detector tracks within a cone of radius $\Delta R = 0.3$ with a $p_T > 0.4$ GeV excluding the electron tracks (variable called Ptcone30)[75], must correspond to a 90% isolation efficiency. To further reduce these background sources, the electrons are required to be isolated, if they are within a cone of radius $\Delta R < 0.4$ with a jet with $p_T > 25$ GeV and JVF>0.75, the candidate electron is rejected.

5.2.2   Muons

This analysis vetoes objects reconstructed as muons, so it is necessary to define them. Muons are reconstructed when hits from the muon spectrometer are matched with the inner detector tracks, using the track information from both detectors, also having into account material effects. The candidate objects are required to have $p_T > 20$ GeV and $|\eta| < 2.5$. These candidates must also satisfy a set of requirements on the muon track quality and must be classified as tight, satisfy the isolation requirements, and have as author MuidCombined. As for isolation criteria, Etcone20 > 2.5 GeV and Ptcone30 > 4 GeV [76].

5.2.3   Jets

Jets are observed as groups of topologically related energy deposits in the calorimeter. ATLAS uses the reconstruction algorithm called *Anti-k_T* 0.4 [77], which is a jet

finding algorithm of the clustering type, within a cone of $\Delta R = 0.4$.

The jet finding is done at the electromagnetic (EM) scale with a jet energy scale (JES) calibration, EM+JES [78]. This is the simplest scheme in which the jet calibration is obtained as a simple correction relating the calorimeter's response to the true jet energy. Jets are selected if $p_T > 30$ GeV and $|\eta| < 4.5$. In order to avoid pile-up events to be considered as jets, the jet vertex fraction (JVF) is required to be greater than 75%. The JVF variable measures the fraction of tracks that originates from the primary vertex that are associated with the jet, which allows to estimate the contribution from multiple interactions. To prevent electron-jet duplicates, if a jet is within $\Delta R < 0.2$ of the identified electron object, then that jet is removed from the jets list.

5.2.4 B-Tagging

The b-tagging algorithm chosen is called MV1, which is a neural network combination of three different b-tagging algorithms [79]:

- `IP3D` - Impact parameter based algorithm that uses a likelihood ratio technique where the input variables are compared to the b-jet and light-jet hypothesis' pre-defined distributions obtained from MC simulation;

- `SV1` - Secondary Vertex based algorithm that builds two-track pairs that form a good vertex using jet associated tracks far away from the primary vertex. All the selected tracks are combined into a single inclusive vertex using an iterative process to exclude the tracks that give the worst χ^2 fit;

- `JetFitter` - Uses a Kalman filter to find the b-jet and c-jet vertices positions as well as a common line on which the primary vertex lies with respect to the latter, in order to give an approximated flight path for the b-hadron.

The MV1 tag weight cut applied is $w_{MV1} > 0.905$, which corresponds to a b-tagging efficiency of 60%, with the jets considered having $p_T > 30$ GeV and $|\eta| < 2.5$.

5.2.5 Missing Energy

The missing transverse energy (E_T^{miss}) measures the neutrino transverse momentum and is calculated using calorimeter cells calibrated according to the different high p_T objects they are associated with. Those objects are electrons, photons, τs, jets, soft jets and muons. They are associated in the order they were referred to. The remaining energy that is not attributed to any object is included as a Cell Out term ($E_{x,y}^{CellOut}$), calibrated to EM scale. The E_T^{miss} is thus calculated as:

$$-E_{x,y}^{miss} = E_{x,y}^{Elec} + E_{x,y}^{Jet} + E_{x,y}^{SoftJet} + E_{x,y}^{Muon} + E_{x,y}^{CellOut}, \quad (5.1)$$

$$E_T^{miss} = \sqrt{(E_x^{miss})^2 + (E_y^{miss})^2}. \quad (5.2)$$

$E_{x,y}^{Elec}$, $E_{x,y}^{Jet}$ and $E_{x,y}^{SoftJet}$ are calculated from the sum of the cluster energies of the respective objects. The electron term uses tight quality selected electrons with $p_T > 10$ GeV. The jet term uses jets with $p_T > 20$ GeV corrected to the EM+JES scale, whereas the soft jets have 7 GeV $< p_T < 20$ GeV and are corrected to the EM scale.

$E_{x,y}^{Muon}$ is calculated from the sum of the measured momenta and the sum of the energy lost by the muons in the calorimeter. Photon and τ objects are not included in this calculation.

In this analysis the missing transverse energy is required to be greater than 30 GeV.

Determination of the Neutrino p_Z Component

The neutrino object needs to be reconstructed at analysis level because the W boson object needs to be reconstructed in order to then be able to reconstruct the top quark. Since in ATLAS the neutrinos are undetected, there is only access to the sum of the transverse missing energy which is assumed to come from neutrinos. So the p_Z component of the neutrino is calculated through energy-momentum conservation of the W boson:

$$M_W^2 = (P^e + P^\nu)^2 = 80.4^2 [GeV], \quad (5.3)$$

$$M_W^2 \simeq 2(E_e E_\nu - \vec{p_e} \cdot \vec{p_\nu}), \quad (5.4)$$

where P^e and P^ν are the four-momentum of the electron and neutrino, respectively. The W mass is fixed to its known value of $M_{W,pdg} = 80.4$ GeV [6]. The expression 5.4 produces two solutions, as shown in expression 5.5; the one that is chosen is the one that attributes to the neutrino a smaller η [80].

$$p_z^\nu = \frac{\lambda \pm \sqrt{\delta}}{2.0} \quad (5.5)$$

where,

$$\alpha = M_{W,pdg}^2 + (p_x^\nu + p_x^e)^2 + (p_y^\nu + p_y^e)^2 - (E^e)^2 \tag{5.6}$$

$$\beta = 0.5(\alpha - (p_T^\nu)^2 + p_z^e)^2) \tag{5.7}$$

$$\gamma = -\frac{\beta^2 - (E^e)^2(p_T^\nu)^2}{(E^e)^2 - p_z^e)^2} \tag{5.8}$$

$$\lambda = \frac{2\beta p_z^e}{(E^e)^2 - p_z^e)^2} \tag{5.9}$$

$$\delta = \lambda^2 - 4\gamma \tag{5.10}$$

In 25% of the cases this gives an imaginary solution. This happens when the transverse mass of the W boson ($M_T = 2(E_T^\nu E_T^e - \vec{p_T^e} \cdot \vec{p_T^\nu})$) is larger than $M_{W,pdg}$ because the W width is not taken into account. For these cases, one assumes the approximation of $M_T \simeq M_W$. Considering a longitudinal, M_L and transverse components for the W mass, M_T:

$$M_W^2 = M_T^2 + M_L^2, \text{where} \tag{5.11}$$

$$M_L^2 = 2|p^e||p^\nu|(1 - cos(\theta^e - \theta^{nu})) \tag{5.12}$$

where θ^e, θ^{nu} are the polar angles for the electron and neutrino respectively and when $M_T \sim M_W$, $\theta^e \simeq \theta^{nu}$ or $\eta^e \simeq \eta^{nu}$. Therefore, in order to solve the imaginary solutions for equation 5.5, in these cases, the η component of the neutrino is replaced by the η of the electron [80].

5.3   Data and Simulation Scaling

A data driven method is applied to determine the contribution of the QCD multijets background to the data. because this background is generally difficult to predict in theory In this section the JetElectron method is thus explained and implemented. The W+jets background, with light flavour jets and heavy flavour jets, one of the most significant in the t-channel analysis also needs to be scaled to better describe the data, through a charge asymmetry study.

5.3.1   QCD Estimation

With protons colliding at such high energies, the main high energy objects produced are jets. Their production is accounted for in the theory of strong interactions, Quantum Chromodynamics (QCD). At higher energies, and beyond the 2→2 scattering, the deviations from the predictions of QCD follow a perturbative expansion in α_S (coupling constant). So, inclusive jet or di-jet production is well known and tested

in hadron colliders, however multijets, where there are more than two jets in the final state, are difficult to deal with in simulation.

In ATLAS, and when high energy jets are required, the QCD is a significant part of the background, more specifically for the t-channel analysis. So in order to estimate the amount of QCD without having to rely on simulation, a data driven method has been applied.

JetElectron Model

The JetElectron model is a data driven method that makes use of the fact that the QCD multijet background is present when there is a jet that is wrongly identified as a lepton. A data sample is produced with a different set of triggers so that a jet can be identified as an electron [56]. A binned-likelihood fit to the data is performed, where the fit parameters are obtained with the conjunction of the so-called JetElectron sample and the rest of the available MC. The normalisation of the QCD background is taken from the fit, whereas the shape is given by the JetElectron sample.

Figure 5.1 illustrates the idea of the fit which looks into a region of a certain variable in which practically no signal can be found. The result of the fit is then extrapolated into the rest of the distribution. The variable chosen in this case is the Transverse Missing Energy, E_T^{miss}. The sideband area is defined as $E_T^{miss} < 30$ GeV.

The binned likelihood fit, that is performed to the data, is done using the TFractionFitter routine [81] in ROOT. This fit is based on a standard likelihood fit, using Poisson statistics. In this manner, the statistical uncertainties of both data and MC are taken into account. The fit is done bin by bin, for different MC and a minimisation of the fit parameters is done analytically. The final result is one scale factor for each MC considered and for the JetElectron sample, which is then scaled to meet the data (together with the MC). The QCD-multijet background is thus determined, with the normalisation provided by the fit and the shape by data.

Event Selection For Application of JetElectron Model

In order to search for the Single Top t-channel signature, one has to have in the final state, at least two jets, one of them tagged as a b-jet, E_T^{Miss} and one lepton, in the case of this analysis, one electron. Thus, each event needs to pass the requirement of having exactly one electron with a $p_T > 25$ GeV and $|\eta| < 2.7$, excluding the regions of $1.37 < |\eta| < 1.52$. The objects identified as jets need to have a transverse momentum greater than 25 GeV, $|\eta| < 4.5$ and there have to be present at least two jets. The normalisation studies focus on the two-jet and three-jet bins because they are the most probable regions to find the signal. In this study there is no minimum
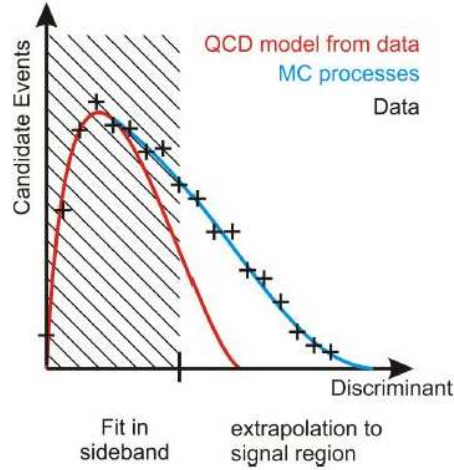
Figure 5.1: *Sketch to illustrate the fit done to obtain the rate of QCD background. The distribution of a chosen variable, in this case the Missing Transverse Energy, is fitted in a side-band where there is close to no signal, and then extrapolated to the other region of the variable [56].*

E_T^{Miss} required, since the fit will be performed in the low energy area as well. There is also the requirement of the transverse mass of W boson, $M_T(W)$ to be greater than 30 GeV, defined as:

$$M_T(W) = \sqrt{2(p_T^{elec}E_T^{Miss} - p_x^{elec}E_x^{Miss} - p_y^{elec}E_y^{Miss})}, \qquad (5.13)$$

where p_T^{elec}, p_x^{elec} and p_y^{elec} are the transverse x and y components of the momentum of the electron and E_T^{Miss}, E_x^{Miss} and E_y^{Miss} are the missing energy known components.

In the JetElectron data sample, the trigger used to obtain the fake electron is `Jet20`. The jet that is mis-identified as an electron needs to have a $p_T > 25$ GeV and the same $|\eta|$ coverage as the electron (although with no crack region). The fraction of the electromagnetic energy needs to be between 0.8 and 0.95 of the total jet energy. The number of tracks within the jet needs to be greater than 3, in order to avoid contribution from converted photons.

Two stages in the selection are studied: before the requirement of a b-tagged jet, which is referred to as the PreTag selection and after selecting at least one b-tagged jet, referred to as the Tag selection.

The distributions of the transverse missing energy can be found in Figure 5.2. Note that the data and MC samples for this study, besides covering the full E_T^{Miss} spectrum (there was no cut on this variable at any point of the datasets' production), are the so-called Loose samples, where the trigger criteria for the electron is set to Loose. The four distributions are then for the two stages of the selection, PreTag

and Tag and for the 2-jet and 3-jet samples.
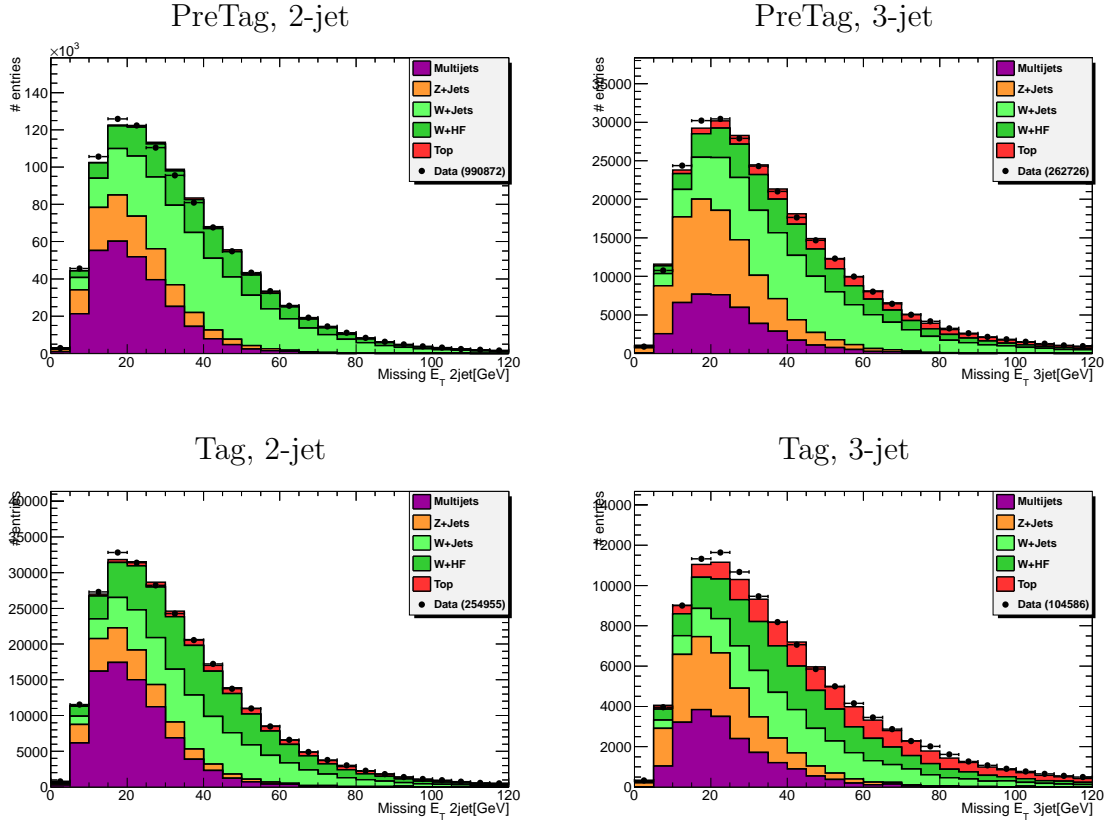
Figure 5.2: *Transverse Missing Energy distributions after the binned likelihood fit performed in order to determine the fraction of the QCD multijet events, for the PreTag dataset (top plots, left for a 2-jet multiplicity and right for 3-jet) and for the Tag datasets (bottom plots, left for a 2-jet multiplicity and right for 3-jet). The MC is normalised to the fit values.*

From these distributions, one can observe that the QCD contribution is greatest at low transverse energy ($E_T^{Miss} < 30$ GeV), so is the Z+jets background. Therefore, a cut in the E_T^{Miss} is perfectly justified in the analysis. There is relatively more QCD background in the 2-jet selection and that fact may be attributed to the di-jet processes. By tagging a b-jet, the processes with top quarks start to be noticeable. For the 3-jet selection the contribution of top samples increases, mainly due to the $t\bar{t}$ background.

5.3.2   W-Jets Scale Factors

There is a charge asymmetry in the W+jets background, since the rate of W^++jets is larger than that of the W^-+jets because there are more valence u quarks than d

quarks in the proton, thus the parton distribution functions (PDFs) will be different. The ratio of the cross sections $\frac{\sigma(pp \rightarrow W^+)}{\sigma(pp \rightarrow W^-)}$ is well understood theoretically, so one can use this knowledge to determine the contribution of the W+jets background to the data. This method works because the QCD multijets, Z+jets and $t\bar{t}$ are charge symmetric and do not contribute to the difference. The single top channels are also charge asymmetric, however, at a low level in the selection, their contributions are very small amongst the background and thus its contributions may be subtracted.

The overall W+jets scale factor are determined before the b-tagging requirement, in the PreTag selection samples, with a cut in the $E_T^{Miss} > 30$ GeV and all other selection cuts maintained as above.

The expression used to extract the W+jets background is:

$$N_{W^+} + N_{W^-} = \frac{\left(N_{W+}^{MC} + N_{W-}^{MC}\right)}{\left(N_{W+}^{MC} - N_{W-}^{MC}\right)} \left(D^+ - D^-\right) = \left(\frac{r_{MC} + 1}{r_{MC} - 1}\right) \left(D^+ - D^-\right), \quad (5.14)$$

where $N_{W^+} + N_{W^-}$ is the final total number of W+jet events, D^+ (D^-) are the total positive (negative) number of W+jets extracted from data, obtained by subtracting all the other MC; $r_{MC} = N_{W+}^{MC}/N_{W-}^{MC}$, taken from the simulated MC W+jets events.

The overall normalisation scale factor for the W+jets before the b-tagging is 0.807 ± 0.031 for the two jet bin and 0.917 ± 0.051 for the three jet bin.

For the Tag samples, the flavour composition of the W+jets e.g as Wc, Wb$\bar{b}$ and Wc$\bar{c}$ has to be taken into account. Each scale factor needs to be computed and determined through a set of dependent expressions [56]. The values used for this analysis are [76]:

	K_{ll}	K_c	K_{cc}	K_{bb}	W_{norm}
2 jet	0.906	0.578	2.199	2.199	0.816
3 jet	0.854	0.545	2.073	2.073	0.777

Here K_{ll} is the light jet scale factor, $K_{cc} = K_{bb}$ and W_{norm} is the overall W+jets scale factor with a b-tagged jet.

Energy Scaling or Smearing

The energy measured in the electromagnetic calorimeter needs to be corrected, and this is done using the well-known resonances decays such as Z→ee, J/ψ →ee or E/P studies that use isolated electrons from W→eν. The energy of the electron in a certain η/ϕ bin is rescaled using the expression $E_{corrected} = E/(1 + scale)$. The smearing of the MC is done to match the energy resolution of the data, taking into account the relevant uncertainties [56].

Pileup Reweighting

In ATLAS, with an increase in luminosity during the data taking, the pileup also increases. The Monte Carlo simulation also takes the pileup into account, but not its increase with the luminosity. As a consequence, the MC needs to be reweighted to account for the true pileup. For this purpose, the pileup information in data is used, the number of primary vertices (PV) are counted and the MC is reweighted to the data values. Because the bunch spacing decreases to 50 ns during the 2011 runs, there is also out-of-time pileup (when the detector has overlapping signals with the neighbouring bunches) to be considered. So, instead of the reweighting being performed with the number of PV, it is, for the 2011 MC, done with the average number of primary vertices, $< \mu >$ [72].

5.4   The t-channel Analysis

As previously stated, the single top t-channel analysis aims at reconstructing a top that decays into a b-jet and a leptonic W. The leptonic W is reconstructed from the neutrino and the electron. The top quark is reconstructed from the W boson and the b-tagged jet. An additional one or two light jets are required. In this study, the background processes are divided into the following categories when presented in distributions or event yield tables:

- t-channel: the signal process, single-top t-channel;

- other top: includes all other top processes: $t\bar{t}$, Wt associated production and the s-channel;

- W+jets: production of the W-boson associated with light jets;

- W+heavy flavour: production of the W-boson associated with heavy flavour jets (Wbb, Wcc and Wc);

- Z+jets, Diboson: production of Z-boson associated with light jets and diboson production: WW, WZ, ZZ;

- Multijets: QCD-multijet background.

5.4.1   Selection Criteria

The following selection is are made to select the exact topology of the t-channel:

- Veto on muons;

- One isolated electron, with $p_T > 25$ GeV and $|\eta| < 2.5$;

- Two or three jets with $p_T > 30$ GeV and $|\eta| < 4.5$;

- One of the jets is b-tagged and with $|\eta| < 2.5$;

- Transverse mass of the W $M_T^W > 30$ GeV;

- Missing Transverse Energy $E_T^{miss} > 30$ GeV.

The cuts on M_T^W and E_T^{miss} help reduce the contribution of the QCD-multijet background.

Initially two different stages of the analysis are presented: the PreTag selection, which includes the cuts described above with the exception of requiring a b-tagged jet. The Tag selection follow the PreTag selection plus the requirement of one of the selected jets to be tagged. Each sample will be studied separately in the cases where there are two and three jets.

Figure 5.3 shows some kinematic variables for the PreTag selection: the p_T and η of the electron, first jet and second jet, the transverse momentum of the missing energy (E_T^{miss}) and the transverse mass of the W boson (M_T^W), defined as:

$$M_T^W = \sqrt{2(p_T E_T - p_x E_x - p_y E_y)}, \tag{5.15}$$

where p_T, p_x and p_y are the transverse, x and y components of the momentum of the electron and E_T, E_x and E_y are the transverse, x and y components of the missing energy.

At this level of selection, the dominant backgrounds are W+jets, light and heavy flavour processes. Both Z+jets/Diboson and the QCD multijets backgrounds have small contributions, from the obvious choice of requiring only one isolated electron and high missing transverse energy. Table 5.3 show the number of events in the simulation and observed data for both 2-jet and 3-jet multiplicity for the PreTag selection.

Figure 5.4 shows the same kinematic distributions as in Figure 5.3, when one of the jets is tagged as a b-jet. It can be seen that most of the W+light jets background is eliminated; the dominant backgrounds remaining are W+heavy flavour jets and $t\bar{t}$ events. Table 5.4 shows the number of events in the simulation and data for both 2-jet and 3-jet multiplicity for the Tag selection. However the t-channel signal is still almost undetectable, at this stage.
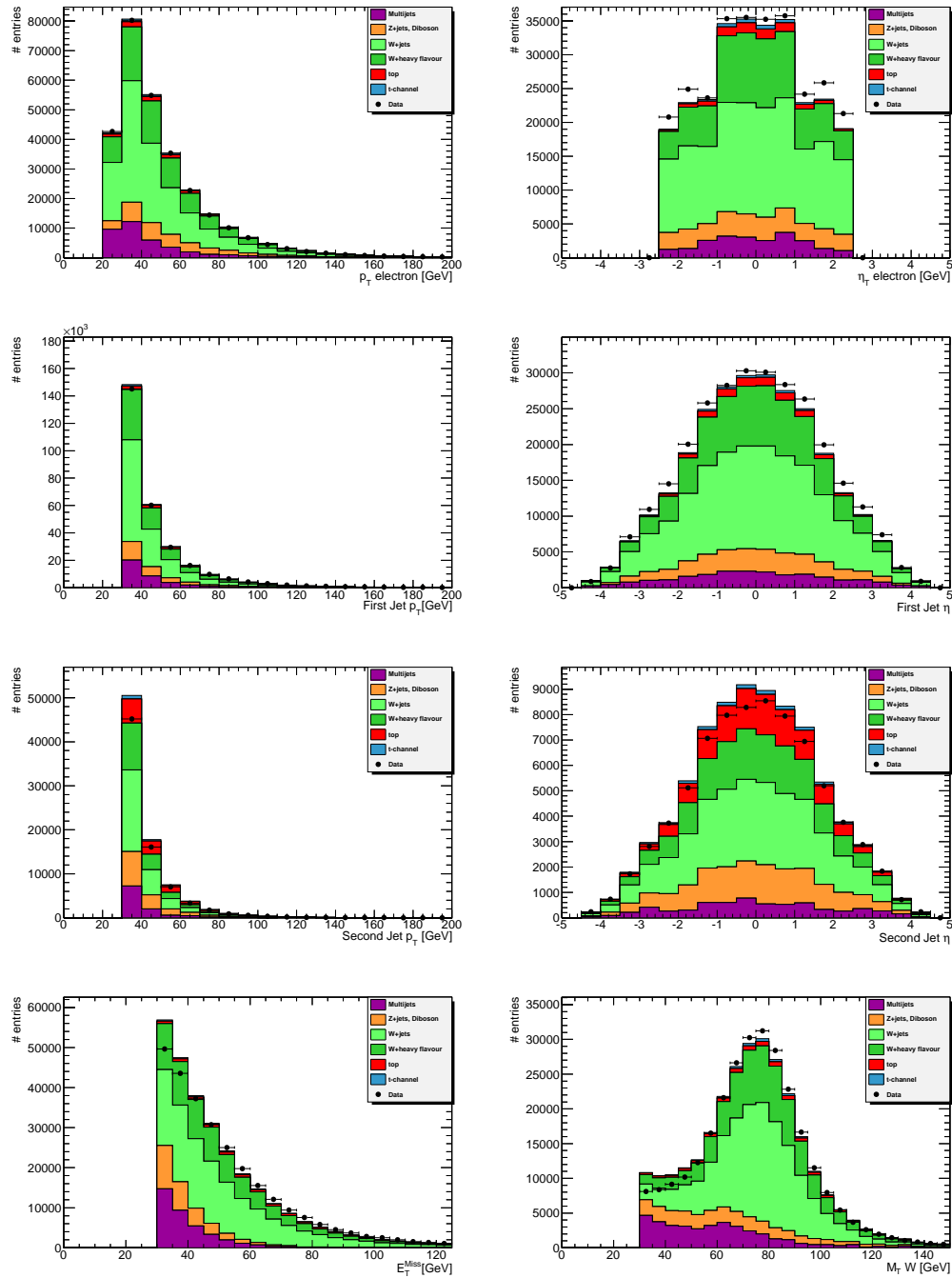
Figure 5.3: *Kinematic distributions for the PreTag selection for the data and simulation for events with two or more jets. Both multijets and W+jets (light flavour and heavy flavour jets) are normalised with data driven methods. The remaining MC is normalised to the SM prediction.*
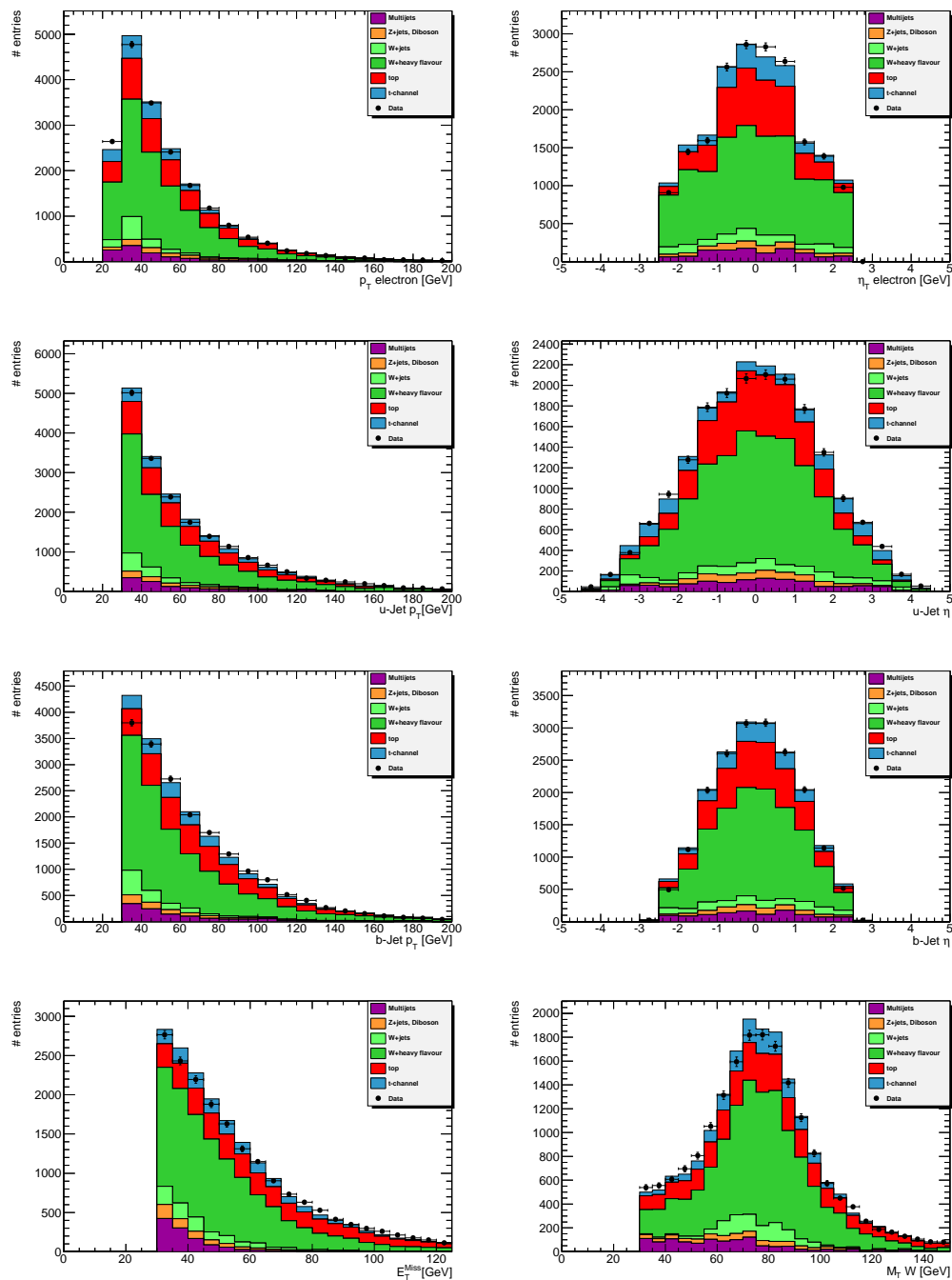
Figure 5.4: *Kinematic distributions for the Tag selection for the data and simulation for events with two or more jets. Both multijets and W+jets (light flavour and heavy flavour jets) are normalised with data driven methods. The remaining MC is normalised to the SM prediction.*

Process	2 jet	3 jet
t-channel	3126.5 ± 10	1441.7 ± 7
Other Top	8369.3 ± 17	11667.1 ± 18.8
W+light jets	134522.0 ± 483	29105.3 ± 181
W+heavy flavour	71746.6 ± 266	16933 ± 129
Z+jets, Diboson	29995.9 ± 96	14119.2 ± 63
Multijets	37428.1 ± 1140	6315.8 ± 408
Total Expected	285189.0 ± 1270	79582.4 ± 469
Obs. data	282464	75727

Table 5.3: *Number of events in the simulation and observed data for 2-jet (left column) and 3-jet (right column) multiplicity for the PreTag selection. Only statistical errors are shown.*

Process	2 jet	3 jet
t-channel	1706 ± 8	753 ± 5
Other Top	4206.3 ± 12	5926.7 ± 13
W+light jets	1087.8 ± 98	224.6 ± 48
W+heavy flavour	10215.7 ± 122.1	3434.7 ± 68
Z+jets, Diboson	640.3 ± 12	430.7 ± 10
Multijets	1122.7 ± 152.6	273.1 ± 58
Total Expected	18979.3 ± 220	11042.7 ± 103
Obs. data	18773	12277

Table 5.4: *Number of events in the simulation and data for 2-jet (left column) and 3-jet (right column) multiplicity for the Tag selection. Only statistical errors are shown.*

5.4.2 Discriminating Cuts

Later in the analysis one can look into trying to further discriminate the signal from the background. Four discriminating variables are presented here:

- The pseudorapidity of the most energetic of the non-tagged jets, $|\eta_{ujet}|$;

- The sum of the transverse momentum of the jets, the electron and the missing transverse energy, H_T;

- The difference between the pseudorapidity of the b-jet and the most energetic non b-jet, $|\Delta\eta_{(bjet,ujet)}|$;

- The invariant mass of the electron, b-tagged and neutrino system, $M_{\ell\nu b}$, which translates into the invariant mass of the top.

$M_{\ell\nu b}$ is given by:

$$M_{\ell\nu b}^2 = (E_\ell + E_b + E_\nu)^2 - (\vec{p}_\ell + \vec{p}_b + \vec{p}_\nu)^2, \tag{5.16}$$

where E and $\vec{p}$ are the energy momentum of each object. Assuming that the electron and neutrino masses are close to zero, the invariant mass is given by:

$$M_{\ell\nu b}^2 = M_b^2 + 2p_\ell p_\nu \left(1 - \cos\phi_{(\ell,\nu)}\right) - p_b \left(p_\ell \cos\phi_{(\ell,b)} + p_\nu \cos\phi_{(\nu,b)}\right) + 2E_b \left(p_\ell + p_\nu\right), \tag{5.17}$$

where M_b and E_b are the mass and energy of the b-jet, p_ℓ, p_ν and p_b are the magnitudes of the momentum for the electron, neutrino and b-jet, respectively. The $\phi_{(a,b)}$ quantities are the angles between objects (a,b) = electron, neutrino or b-jet.

Figures 5.5 and 5.6 show these discriminant variables after the Tag selection level for 2-jet and 3-jet, respectively.

The cuts performed on the discriminant variables are:

- $|\eta_{ujet}| > 2.0$;

- $H_T > 210$ GeV;

- $|\Delta\eta_{(bjet,ujet)}| > 1$.

These cuts aim at excluding the areas where the signal to background ratio is much smaller. They are very conservative and eliminate most of the events, but result in a more discriminated sample. The invariant mass discriminant is used to fit the MC to the data.

5.5   Cross Section Determination

The cross section, $\sigma_{tchannel}$ is determined by:

$$\sigma_{tchannel} = \frac{f_{tchannel} N_{data}}{\epsilon_{tchannel}^{reco} \mathcal{L} P_{(W \to e\nu)}}, \tag{5.18}$$

where $f_{tchannel}$ is the fitted fraction of the data corresponding to the t-channel signal, N_{data} is the number of events observed, $\mathcal{L}$ is the total integrated luminosity, $\epsilon_{tchannel}^{reco}$ is the reconstruction efficiency given by

$$\epsilon_{tchannel}^{reco} = \frac{N_{MC}^{reco}}{N_{MC}^{generated}},$$
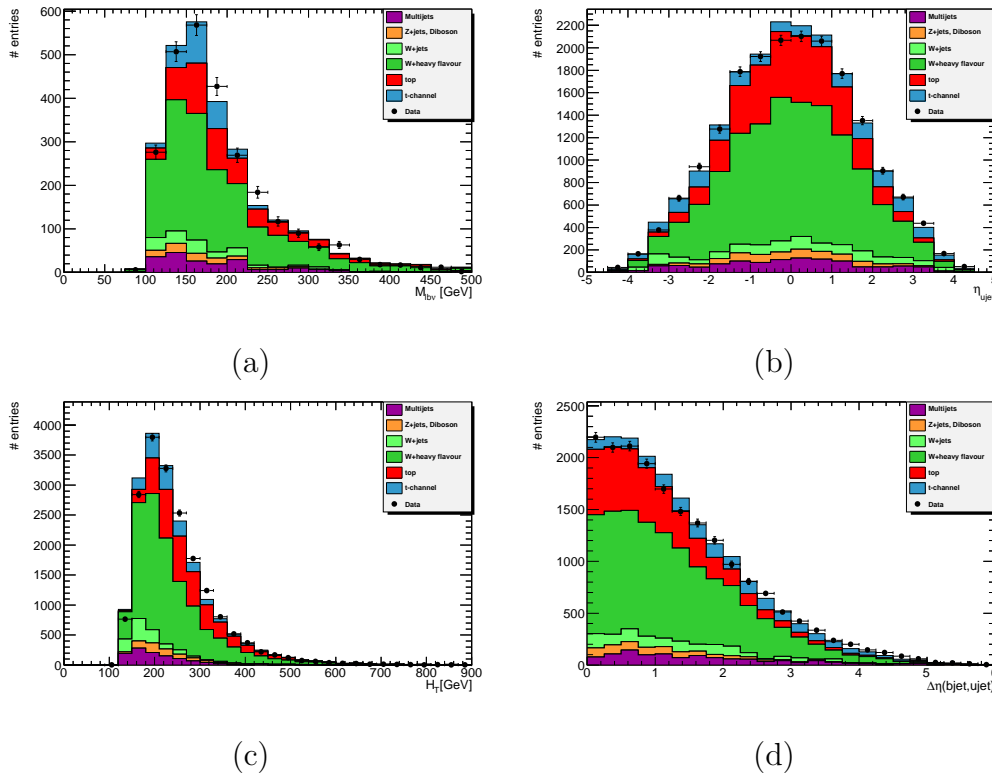
Figure 5.5: *Distributions of the discriminating variables for the samples of 2 jets, one of them tagged: (a) the top invariant mass, (b) $|\eta_{ujet}|$, (c) H_T and (d) $|\Delta\eta_{(bjet,ujet)}|$. Both multijets and W+jets (light flavour and heavy flavour jets) are normalised with data driven methods. The remaining MC is normalised to the SM prediction.*

where $N_{MC}^{generated}$ is the total number of generated t-channel events and N_{MC}^{reco} is the number of MC t-channel events that remain after all the analysis cuts. This analysis is only studying the case when the W boson decays leptonically into an electron and a neutrino. The W decays into an electron and neutrino $(10.75 \pm 0.03)\%$, however the case when W decays into τ and neutrino, $(11.25 \pm 0.20)\%$ must be taken into account when the τ lepton decays into the $\tau \to e\nu_e\nu_\tau$ $(17.85 \pm 0.05)\%$ or $\tau \to e\nu_e\nu_\tau\gamma$ $(1.75 \pm 0.18)\%$ (all values taken from [6]), because they have similar topologies. The variable $P_{(W\to e\nu)}$ is the probability of this channel to occur taking into account all possibilities.

In order to obtain the fraction of events corresponding to the t-channel, a binned likelihood fit is performed to the invariant mass distribution, with the ROOT function TFractionFitter [81]. This fits the Monte Carlo fraction to the data histogram. The free parameters for the fit are the fraction of t-channel simulation and the fraction of the other top added to the W+heavy flavour simulation. As can be seen from the invariant mass distribution in Figure 5.7, the contributions of the

(a)   (b)

(c)   (d)
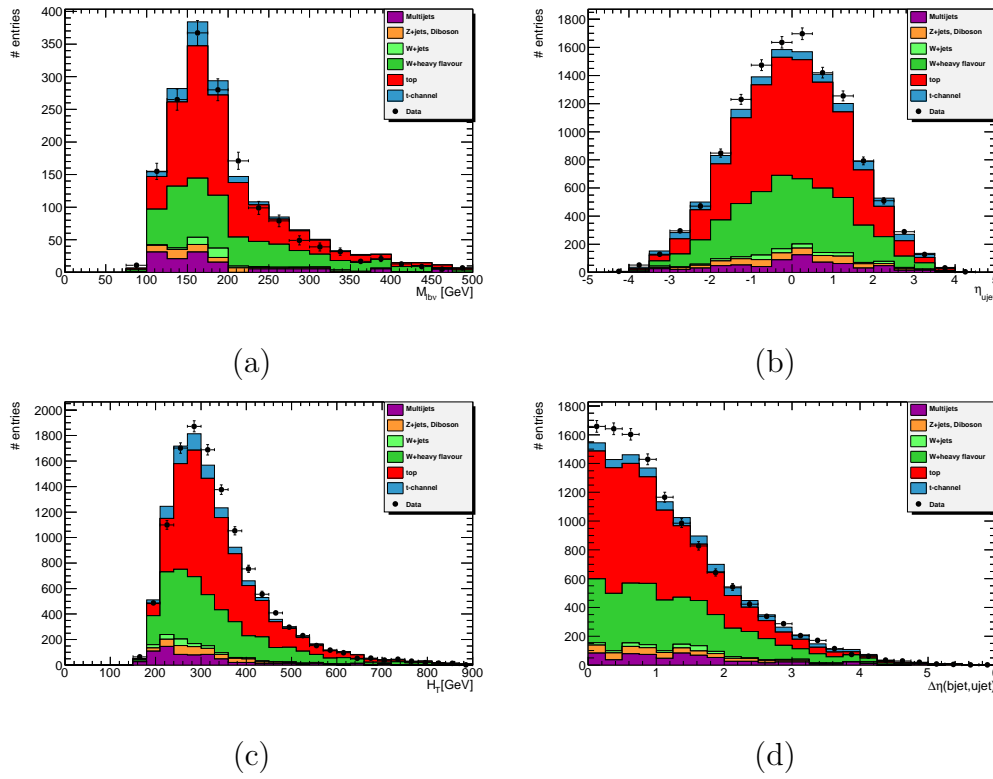
Figure 5.6: *Distributions of the discriminating variables for the samples of 3 jets, one of them tagged: (a) the top invariant mass, (b) $|\eta_{ujet}|$, (c) H_T and (d) $|\Delta\eta_{(bjet,ujet)}|$. Both multijets and W+jets (light flavour and heavy flavour jets) are normalised with data driven methods. The remaining MC is normalised to the SM prediction.*

Z+jets/Diboson, QCD and W+light jets backgrounds are very small after the discriminating selection, and since both QCD and W+light jets backgrounds have already been scaled through data driven methods, they are excluded, along with the Z+jets contribution from the fit. The shape of the invariant mass distributions for the non t-channel top events (which are mainly from $t\bar{t}$ events) and the W+heavy flavour backgrounds are very similar, considering that the selected events have the same topology, so these backgrounds are considered together, scaled with the fit parameters and their relative amounts taken from the MC.

The values for the quantities of the cross section calculation are:

$$\mathcal{L} = 4660 \pm 0.084\,\mathrm{pb}^{-1},$$

$$P_{(W\to e\nu)} = 0.1295 \pm 1.7334 \times 10^{-6},$$

and also the values for each of the samples considered are presented in Table [**?**]

Figure 5.8 shows on the left column the invariant mass distributions fitted to the fractions provided, for 2-jet (top) and 3-jet (bottom). On the right column are the
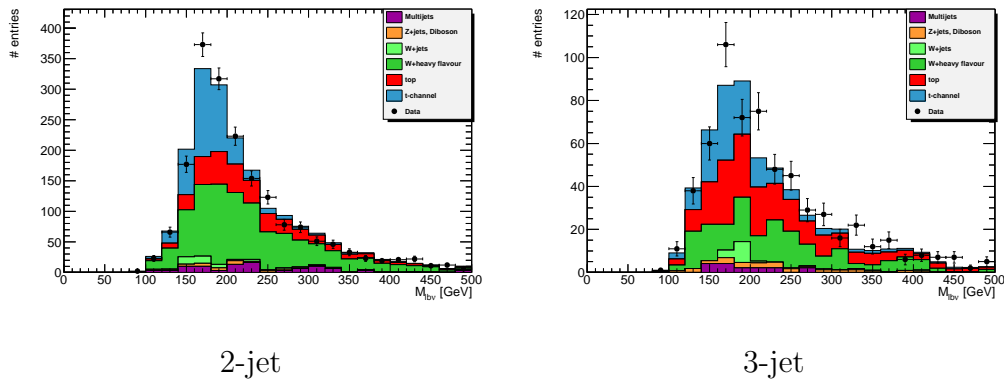
2-jet   3-jet

Figure 5.7: *Invariant mass distributions after the selection is applied for the 2-jet and the 3-jet samples.*

Quantity	2-jet	3-jet
N_{data}	1898	633
$f_{tchannel}$	0.317 ± 0.044	0.260 ± 0.070
$\epsilon_{tchannel}^{reco}$	$0.015 \pm 1.215 \times 10^{-4}$	$4.754 \times 10^{-3} \pm 6.895 \times 10^{-5}$

Table 5.5: *Values for each of the samples for the calculation of the cross section.*

adjusted MC prediction of each template used, in this case the t-channel and other top plus W+heavy flavour.

Table 5.5 gives the final event yields for the 2-jet and 3-jet samples, with the t-channel, other top and W+heavy flavour MC scaled to the fit results. QCD multijets and W+light jets are scaled with data driven methods.

The values for the cross sections for the 2-jet, 3-jet and 2-jet+3-jet samples are:

	2-jet	3-jet	2-jet+3-jet
$\sigma_{tchannel}$ [pb]	67.62 ± 9.58	57.43 ± 15.61	62.23 ± 8.04

The 2-jet sample is statistically more significant, whereas the 3-jet sample has more background present, especially due to the $t\bar{t}$ contribution. The 2-jet+3-jet sample is considering the sum of the two invariant mass distributions and a new fit is performed.

Charge separation

By dividing the samples according to the lepton charge, one can calculate the individual cross sections of top-quark and top-antiquark, with the same procedure as before. The resulting values for the cross section assuming the reconstruction efficiency is the same as for the full sample, are:

(a)

(b)

(c)

(d)
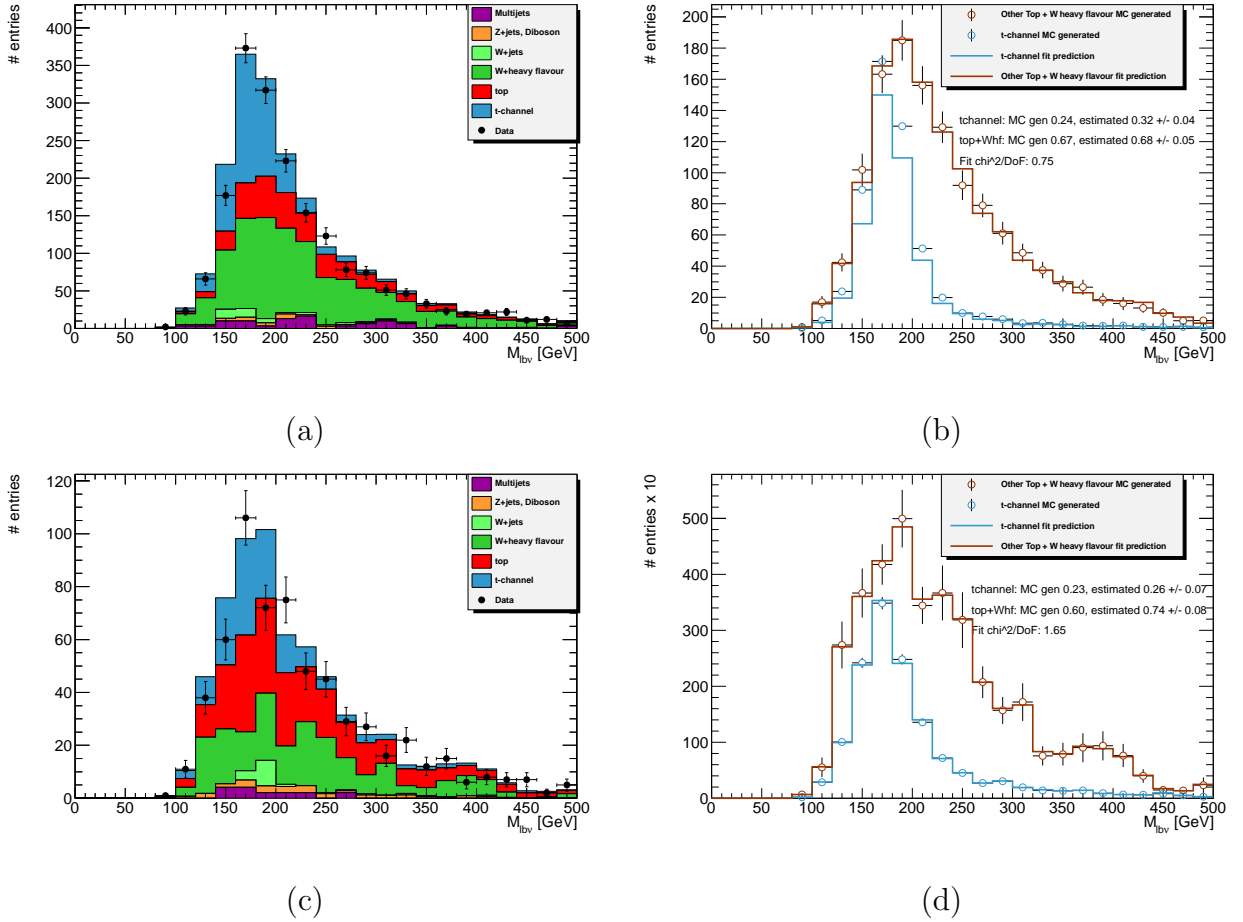
Figure 5.8: *Fitted top invariant mass distributions for the 2-jet (a) and 3-jet (c) samples. (b) and (d) (2-jet and 3-jet respectively) show the MC prediction for both templates used and indicate the resulting scale as opposed to the MC simulation provided scale.*

Channel	2-jet	3-jet	2jet+3jet
$\sigma_{t \to W^+ b}$ [pb]	46.28 ± 8.08	42.46 ± 14.56	41.40 ± 7.12
$\sigma_{\bar{t} \to W^- b}$ [pb]	24.37 ± 6.41	33.80 ± 11.60	22.63 ± 6.04

These results are in good agreement with the theoretical prediction of $41.9^{+1.8}_{-0.8}$ pb and $22.7^{+0.9}_{-1.0}$ pb for top-quark and top-antiquark, respectively [24].

The top process dominates with respect to the anti-top due to the PDF of the proton and the fact that the LHC collides proton with proton. Protons have two valence u quarks, so the light quark in the initial state is more likely to be of this flavour and thus resulting in a final state with a top quark.

Process	2 jet	3 jet
t-channel	538.5 ± 96	147.1 ± 44
Other Top	358.9 ± 30	248.7 ± 39
W+light jets	44.6 ± 23	17.2 ± 14
W+heavy flavour	951.6 ± 80	219 ± 34
Z+jets, Diboson	39.5 ± 3	23.8 ± 2
Multijets	94.4 ± 21	18.8 ± 7
Total Expected	2027.4 ± 132	674.6 ± 69.6
S/B	0.36 ± 0.07	0.28 ± 0.09
$S/\sqrt{S+B}$	11.96 ± 2.17	5.67 ± 1.72
Obs. data	1898	633

Table 5.6: *Final selection after the likelihood fit event yields for the data and simulation, for the 2-jet and 3-jet samples. The signal (S) over background (B) ratio and the significance are also indicated. Only statistical errors are shown.*

Chapter 6

Systematic Uncertainties

This chapter describes my contribution made to the MultiJetsUncertaintyProvider package in order to determine the flavour composition uncertainty. Some observations are made and the example distributions are shown.

The main sources of systematic uncertainties are briefly explained and the final measured value for the cross section is presented.

6.1 Multi-jet JES Uncertainty

The Jet Energy Scale (JES) is an energy calibration of jets originating from the fragmentation of quarks and gluons, which are the most common and complicated final state objects in hadron collider experiments such as ATLAS. The uncertainty associated to the JES is one of the main source of uncertainties for many measurements involving jets.

This uncertainty can be estimated using two C++/ROOT compatible packages to access the current estimation of the JES uncertainty on the full 2011 7 TeV dataset: MultijetJESUncertaintyProvider and the package from which is derived, JESUncertaintyProvider [82]. In the case of multijets, as more than two jets are involved in this particular analysis, the uncertainty provided includes the global JES uncertainty from the JESUncertaintyProvider for isolated QCD jets plus the additional terms accounting for the flavour composition, calorimeter response and close-by jets effects, via the MultijetJESUncertaintyProvider package. The uncertainty is valid for Anti-k_T 0.4 or 0.6 (this study only uses 0.4) jets with the EM+JES calibration and it takes into account pile-up corrections.

In the MC simulation, gluon-initiated jets (gluon-jets) have a slightly different calorimeter response from the light-quark-initiated jets (LQ-jets). This is verified because jets that are associated to the gluon-jets tend to be wider, with less energy density in the central cone of the jet before interacting with the detector and to have

more particles that are also softer than in the case of the LQ-jets [83]. This feature is one source of systematic uncertainty.

Only the $t\bar{t}$ process input files, with a few selection cuts specific to that channel are available as part of the package, therefore the need to create input files for the single top processes. Both t-channel and Wt production processes are considered for this study. The s-channel input files could not be produced due to lack of statistics and available samples.

The goal is to calculate the fractions of LQ-jets and gluon-jets for each single-top process, in order to determine the flavour composition uncertainty. The MultijetJESUncertaintyProvider package receives three types of information as input: gluon-jets fraction, uncertainty of the gluon-jets fraction and the average response of jets.

The samples used are from MC10 simulation, using Release 16, in the form of Single Top ntuples, using the LooseTopInputs tree with loose electron and muon definitions from those ntuples. To access the truth information, TruthTree is used. Table 6.1 lists the samples used for this study including the generator. For the gluon-jet fraction determination and the jet-response calculation for each process, both electron and muon channels are considered. The nominal samples are the MC@NLO generated ones. The AcerMC generated samples are used for the determination of the uncertainty in the gluon-jet fraction.

Jets with $p_T > 10$ GeV are considered. Firstly, events with electron ($\Delta R(jet,electron) < 0.2$) or muon ($\Delta R(jet,electron) < 0.4$) overlap are excluded. The highest energy truth particle, if it is a gluon or a light-quark (all quarks excluding the top quark) and within a cone of $\Delta R = 0.4$ is then associated to each jet[1].

For the calculation of the fraction of gluon-jets, a simple counting of matched jets is done:

$$F_g = \frac{N_g}{N_g + N_q},$$

where N_g is the number of gluon-jets and N_q is the number of LQ-jets in the sample considered.

The gluon-jets fraction uncertainty is a systematic uncertainty obtained by the maximum difference between the default MC@NLO and the three samples: the gluon-jets fractions obtained with a different generator (AcerMC) and variations in initial and final state radiation (referred to as ISR/FSR) processed with AcerMC as well. Any uncertainty on the gluon-jets fraction consequently propagates into an uncertainty on the JES. Figure 6.1 shows the gluon-jet fraction as a function

---

[1]Association of partons to jets is not theoretically accurate, as it depends on the analysis and the definition of light-quark of gluon is at best a leading-order concept. However, for purposes of these performance studies, leading-order is sufficient [83].

Channel	Generator	ID
t-channel	MC@NLO	108340
		108341
		108342
wt-prod	MC@NLO	108346
t-channel	AcerMC	117360
		117361
		117362
wt-prod	AcerMC	105500
t-channel	AcerMC,ISR/FSR up	117380
		117381
		117382
wt-prod	AcerMC, ISR/FSR up	117386
t-channel	AcerMC,ISR/FSR down	117370
		117371
		117371
wt-prod	AcerMC, ISR/FSR down	117376

Table 6.1: *Samples used for the determination of gluon-jet fraction and the jet-response in each process. The nominal samples are the MC@NLO generated ones. The AcerMC generated samples are used for the determination of the uncertainty in the gluon-jet fraction.*

of the jet p_T for the four different samples of t-channel considered. The gluon-jet fraction differs with the two generators (MC@NLO and AcerMC) and also shows an increase (decrease) with the increase (decrease) of ISR/FSR, with respect to the default AcerMC generator.

The jet transverse momentum response (henceforth referred to as jet-response) is given by Response $= \frac{p_T^{reco}}{p_T^{true}}$, where p_T^{reco} is the reconstructed transverse momentum of the selected jets and p_T^{true} is the truth transverse momentum which is associated to that jet. The response is computed in bins of η and p_T. The average response is the mean given by a Gaussian for each fraction bin. For this calculation isolated jets are required: with $\Delta R > 2.5 \times 0.4$ from the closest jet with $p_T^{EM} > 7$ GeV and need to be within $\Delta R = 0.3$ of its associated parton.

The gluon-jets fraction, its uncertainty and the jet-response as described above, need to be provided as input to the package, in the form of three distributions in bins of: $0 < p_T < 2500$ GeV and $0 < |\eta| < 4.5$. With such a high p_T range, some higher p_T bins fail to have relevant statistics so those values are obtained by extrapolating
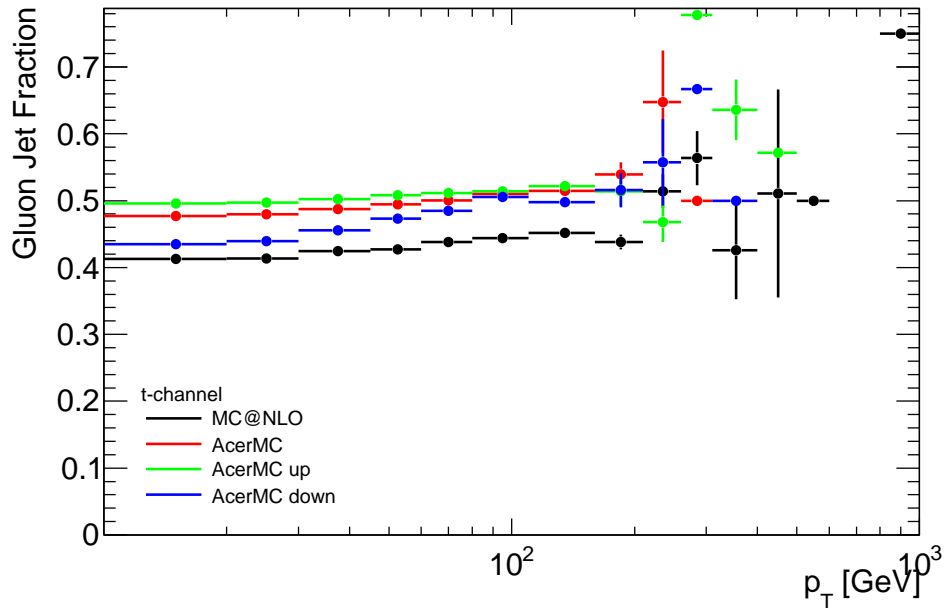
Figure 6.1: *Gluon-jet fraction for the t-channel process with four different samples: two generators, MC@NLO (black points) and AcerMC (red points) and with an increase (AcerMC up, green points) or decrease (AcerMC down, blue points) in the ISR/FSR.*

the response values of the nearest bins.

The jet flavour composition uncertainty can be therefore calculated by estimating the maximum (relative) increase or decrease in response when varying the fraction of gluon jets:

$$\Delta^+ = \frac{r_{lquark} - r_{sample}}{r_{sample}},$$

$$\Delta^- = \frac{r_{sample} - r_{gluon}}{r_{sample}},$$

where r_{lquark}, r_{gluon} and r_{sample} are the light-quark, gluon and sample response, respectively. r_{sample} is the term provided in the input files, since it is analysis dependent.

This can be understood with the simple sketch below[82]:
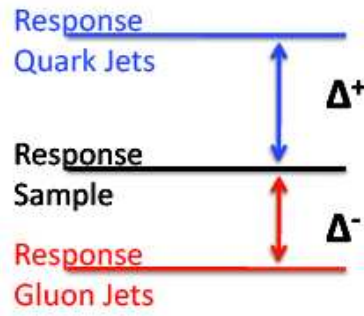
Δ^+ and Δ^- are multiplied with the fraction of the maximum increase or decrease in response that is possible with the gluon fraction uncertainty (Δf_{gluon}):

$$\alpha_c^+ = \Delta f_{gluon}/f_{gluon} \, , \, \alpha_c^- = \Delta f_{gluon}/(1 - f_{gluon}),$$

where α_c^+/α_c^- are called the alpha correction factors, which are supplied by the package as a function of the jet p_T. These combined quantities represent the provider's knowledge of how the mean response would change due to the uncertainty of how many gluon-jets are found in data [82].

Figure 6.2 shows the jet-response 3-dimensional distribution obtained from the input files for the package. The jet-response is shown as a function of η and p_T of the jets for the t-channel process; the Wt-production process has a similar behaviour. One can see that there is a small response at low p_T region, which reflects on a large relative positive uncertainty and a small relative negative uncertainty.
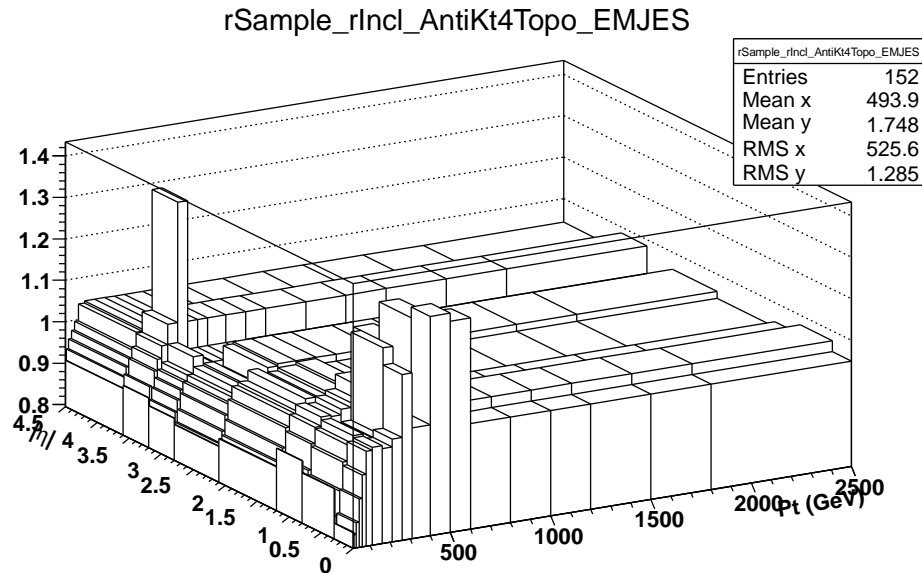
Figure 6.2: *Jet-response as a function of η and p_T for the jets for the t-channel process.*

While performing these studies, it has been shown that a percentage of jets, mainly at low p_T, fail to be matched to a gluon or light-quark parton, as can be seen from Figure 6.3: the p_T (left) and η (right) of the jets which can be associated to light-quarks (green line), to gluons (yellow line) or the non-matched jets (red line) is shown for the default t-channel MC@NLO sample. These unmatched jets could be assumed to be gluon-jets from ISR/FSR. However they make around 6% of the isolated jets[2] and so, until a better understanding of their provenance is found, they will not be considered.
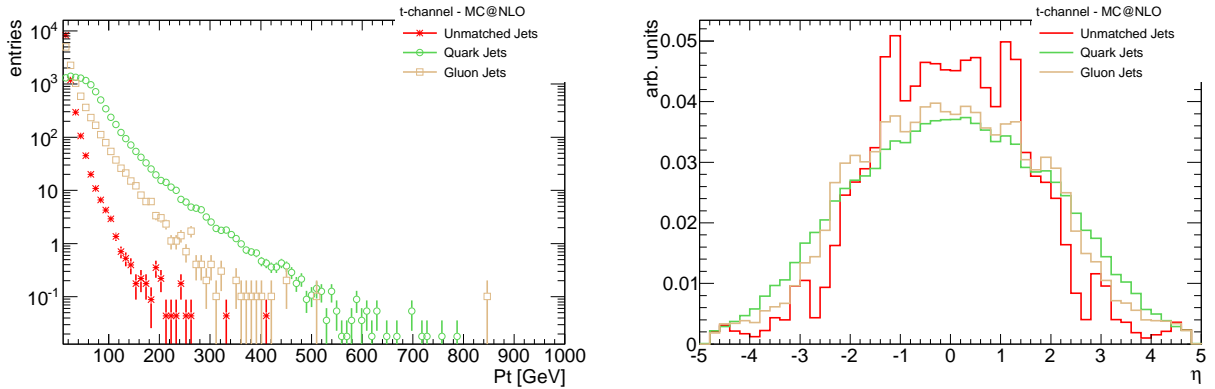
Figure 6.3: *The p_T (left) and η (right) distributions of the jets which can be associated to light-quarks (green line), to gluons (yellow line) or the non-matched jets (red line) for the t-channel MC@NLO sample.*

Figure 6.4 shows the jet response for all jets (black points) and for the isolated jets (red points). The isolated jets show a greater response than overall jets.

Figure 6.5 shows example plots of the relative negative (left side) and positive relative (right side) uncertainties for the t-channel process as a function of the p_T, in the $1.2 < |\eta| < 2.1$ bin. Some bins have large statistical fluctuations (due to low statistics), which are not a physics effect, and therefore the distributions need to be smoothed. This effect can push the jet response below or above the response for gluons or light-quark jets respectively. This may lead to a zero negative or positive flavour composition uncertainty.

The input files created with this study are also used throughout Release 17. They are thus valid for this analysis.

---

[2]as mentioned before isolated jets are the ones outside a $\Delta R > 2.5 \times 0.4$ from the closest jet and have a $p_T^{EM} > 7$ GeV
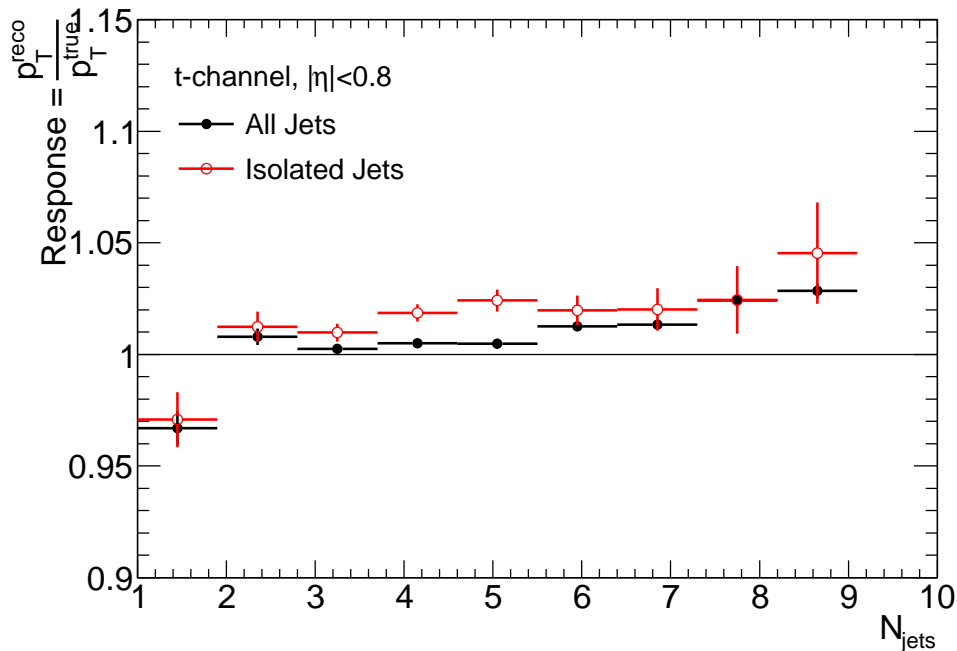
Figure 6.4: *Response for all jets (black) and for isolated jets (red points) as a function of jet multiplicity.*

6.2 Sources of Systematic Uncertainties

The systematic uncertainties for the cross section determination have several sources: jets, electron, missing transverse energy and others (listed below). These systematics are used in accordance to the Top Group systematic uncertainties recommendations and their applications are mainly described in [76].

6.2.1 Jets

- **Jet Energy Scale** - Provided by the MultijetJESUncertaintyProvider package, the uncertainty depends on the p_T and η of the reconstructed jet. The jet energy is scaled 1σ up and down, its change is propagated to the E_T^{Miss} calculation and the analysis is repeated. The package also includes uncertainties due to pile-up events and on b-tagged jets, which are added quadratically to the JES uncertainty.

- **Jet Reconstruction Efficiency** - These studies are done using a tag-and-probe method on QCD di-jet events, where jets are reconstructed from tracks and from the calorimeter cells. A tool [84] provides the probability of the jet being badly reconstructed. The analysis is run and jets above a probability
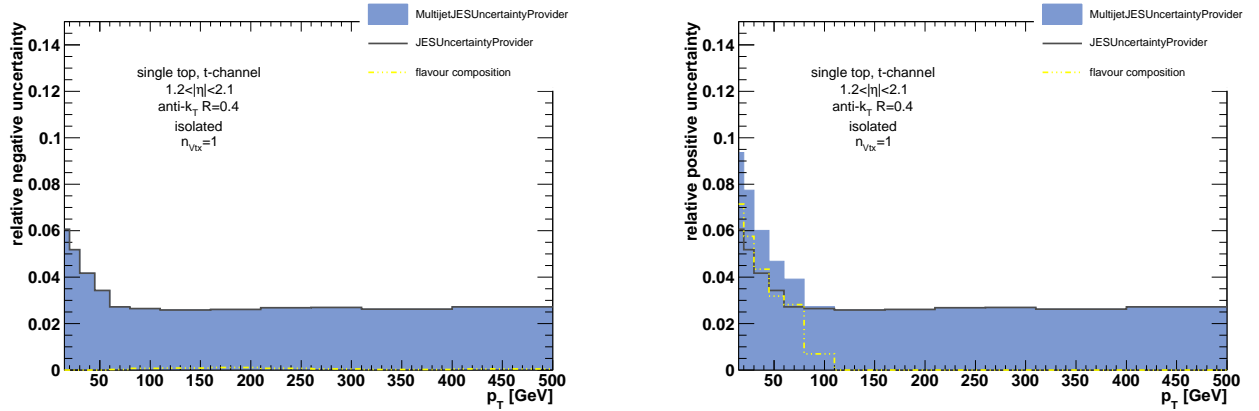
Figure 6.5: *Response for all jets (black) and for isolated jets (red points) as a function of jet multiplicity.*

value are discarded and a comparison is made with the nominal analysis.

- **Jet Energy Resolution** - The jet energy is smeared in MC events with a tool provided by the jet group [84] and the analysis is run and compared with the nominal one.

6.2.2 Electron

- **Electron reconstruction, ID efficiency, Isolation and Trigger Scale Factors** - The scale factors (SF) applied to the MC events have associated uncertainties which are used as systematics uncertainties.

- **Electron Energy Scale and Resolution** - The systematic estimation is done by scaling the transverse momentum 1σ up and down and performing the event selection. For the electron energy resolution, the energy is smeared in data and its impact is evaluated, according to the Top Group suggestions.

6.2.3 Missing Transverse Energy

- **CellOut and SoftJet Uncertainty** - These uncertainties are 100% correlated and account for the uncertainties in the cell out and soft jets terms used in the calculation of the E_T^{miss}, as described in Chapter 5.

- **Pile-up Uncertainty** - Application of 6.6% uncertainty is suggested by the top group of ATLAS and accounts for uncertainties on the value of E_T^{Miss} due to pile-up.

6.2.4 Other Systematics

- **Luminosity** - The recommendation is to attribute the luminosity an uncertainty of 1.8%.

- **PDF** - The uncertainty in the PDFs is calculated by taking the envelope of the estimated uncertainties for the CT10, MSTW2008NLO and NNPDF2.0 PDF sets, following the PDF4LHC recommendations[85].

- **ISR/FSR** - The variation in ISR/FSR is determined with collision data and its dependence on the acceptance for all top processes is estimated with a set of AcerMC+Pythia samples tuned to those variations.

- **MC generator** - This uncertainty is estimated by comparing different generators: for instance, the $t\bar{t}$ process default generator is MC@NLO+Herwig, which is then compared with Powheg+Herwig and Alpgen+Herwig. The largest difference is considered. For single-top processes, the generator is the same, and the uncertainty is estimated through a parton level study using 4-flavour or 5-flavour schemes.

- **Background MC cross section normalization** - The uncertainty on the background simulation normalization is considered statistical for the top, diboson and Z+jets processes. For the data driven processes, W+jets (light and heavy flavour) and QCD, an uncertainty of 50% is considered.

- **Template Fit** - The uncertainty on the template fit is estimated by varying each of the background distributions by 50% (in the cases where the fit converges) and extracting the maximum difference.

6.2.5 Summary of Uncertainties

Table 6.2 shows the breakdown of the systematic uncertainties discussed above. The values, except from the Template fit uncertainty, are either fixed recommendations or calculated by [76] with its analysis coinciding with the same data-taking period and luminosity. The ISR/FSR and MC generator are the largest sources of systematic uncertainties. Statistical uncertainties include data and MC simulation statistics, the errors associated with the template fit parameters and each variable used for the calculation of the cross section.

The overall t-channel cross section, by combining two different channels (with two or three jets) is:

$$\sigma_{t-channel} = 62.2 \pm 8.0(\text{stat})^{+8.6}_{-8.8}(\text{syst})\,\text{pb}.$$

Source	$\Delta\sigma_{obs}/\sigma_{obs}$ [%]
Jet Energy Scale	+5.0/-5.5
Jet Reconstruction Efficiency	±0.8
Jet Energy Resolution	±2.6
Electron reconstruction, ID eff, Isolation and Trigger SF	±1.3
Electron Energy Scale and Resolution	±0.7
CellOut and SoftJet	±0.4
E_T^{Miss} Pile-up	+0.9/-0.8
Luminosity	±1.8
PDF	+4.1/-2.6
ISR/FSR	±7.9
MC generator	±7.3
Background MC cross section normalization	±3.8
Template Fit	+2.2/-3.3
Total systematics	+13.8/-14.2
Total	+16.0/-16.3

Table 6.2: *Contribution [76] of each source of uncertainty of the t-channel cross section. Statistical uncertainties are quadratically added to the total.*

This value agrees well with the theoretical prediction $64.2^{+1.8}_{-1.1}$ pb [24].

Chapter 7

Conclusions

The main study of this thesis is the calculation of the cross section of the single top t-channel process with a cut based analysis.

After the theoretical background and the ATLAS detector are explained, my contribution to the SCT is presented. The Lorentz angle is calculated for cosmic ray and collisions data, as well as for MC simulation data. Even though the result for the collisions data differs from the theoretical predicted one, such measurement is consistent between different data runs and robust enough to serve to control the SCT operation.

For the analysis of t-channel events, the data and MC simulation needs to be tuned. The MC is simulated with the present knowledge of the theory models, of previous data taken in previous detectors and of the expected behaviour of the current detector. With real collisions data arriving, it is understandable that the MC will need to be corrected. The single top is expected to be found amongst several backgrounds: $t\bar{t}$ and W+heavy flavour jets are the main ones. Other backgrounds are Z+jets, W+light jets, QCD multijets and diboson (WW, ZZ and WZ processes).

QCD multijets background is not very well known and simulation does does predict it accurately. Thus, a data-driven method was implemented to simulate this background: the JetElectron model, where a jet is wrongly identifies as a lepton. This method is a good approximation to the QCD multijets background, however one is left with little statistics after all the selection cuts, leaving some p_T ranges with zero QCD simulated events. A different method could be implemented for future studies.

A cut based analysis is performed. The selection cuts are the necessary to best eliminate the background: high transverse momentum jets and electron, high amount of missing transverse energy, a jet tagged as a b-quark, and the reconstruction of the W boson and the top quark. Three powerful discriminating cuts are applied to exclude the areas where the signal to background ratio is much smaller.

Finally a binned likelihood fit is performed using the invariant mass of the reconstructed top distribution. The fit chooses the amount of data one believes to correspond to the t-channel signal.

The value for the cross section, combining the samples for two and three jets present is

$$\sigma_{t-channel} = 62.2 \pm 8.0(\text{stat})^{+8.6}_{-8.8}(\text{syst})\ pb.$$

This value is in good agreement with the theoretically predicted value of $64.2^{+1.8}_{-1.1}$ pb.

The value obtained has an uncertainty of about 19%. This can be improved by increasing the amount of data analysed and improving the knowledge on the sources of systematics. As a future work proposal, the muon channel can be included in order to combine statistics. The data acquired at $\sqrt{s}=$ 8 TeV can also be looked at. For the continuation of studies of the t-channel, the top quark polarization can be calculated.

Single top quark production in the t-channel has been studied in $\sqrt{s} = 7$ TeV and $\sqrt{s} = 8$ TeV pp collision data recorded with the ATLAS and CMS detectors in 2011 and 2012. With $\sim$1 fb^{-1} of 7 TeV data the inclusive cross section was measured with multivariate techniques: for ATLAS, a neural network technique is used which combines several variables into one discriminant; the obtained cross section is: $\sigma_{t-channel} = 83 \pm 20$ pb [27]. For CMS, two independent multivariate analyses are performed as a cross-check for each other, one based on a neural network discriminant and the other on Boosted Decision Trees (BDT) discriminant; the obtained cross section is $\sigma_{t-channel} = 62 \pm 6$ pb [86].

The result presented in this thesis benefits from more statistics (4.7 fb^{-1}) than the published result for 7 TeV (more luminosity is currently being used for $\sqrt{s} = 8$ TeV) and the cut selection of the analyses are the same. With the use of Multivariate analyses the results take into account the effects of all variables on the responses of interest, as opposed to only one variable (the invariant mass in the case of this analysis) and provide a result more robust an less dependant on statistical fluctuations.

Overall, it can be concluded that with an amount of 4.7 fb^{-1}, the single top t-channel can be observed performing a straightforward cut based analysis.

Bibliography

[1] F. Abe et al., *Observation of top quark production in $p\bar{p}$ collisions with the collider detector at fermilab, Phys. Rev. Lett.* **74** (1995) 2626–2631.

[2] S. Abachi et al., *Observation of top quark, Phys. Rev. Lett.* **74** (1995) 2632–2637.

[3] **ATLAS** Collaboration, G. Aad et al., *Observation of a new particle in the search for the Standard Model Higgs boson with the ATLAS detector at the lhc, Phys.Lett.* **B716** (2012) 1–29.

[4] **CMS** Collaboration, S. Chatrchyan et al., *Observation of a new boson at a mass of 125 GeV with the CMS experiment at the LHC, Phys.Lett.* **B716** (2012) 30–61.

[5] "Standard model of particle physics."
`http://www-sldnt.slac.stanford.edu/alr/standard_model.htm`.

[6] J. Beringer et al., *Particle data group - 2012 review of particle physics, Phys. Rev.* (2012), no. 1.

[7] Y. L. Dokshitzer, *Calculation Of The Structure Functions For Deep Inelastic Scattering And $e^{+}e^{-}$ Annihilation By Perturbation Theory In Quantum Chromodynamics., Soviet Physics, JETP [Zh. Eksp. Teor. Fiz.* **73** *(1977) 1216]* **46** (1977), no. 641.

[8] V. N. Gribov and L. N. Lipatov, *$e^{+}e^{-}$ Pair Annihilation And Deep Inelastic ep Scattering In Perturbation Theory, Yad. Fiz. [Sov. J. Nucl. Phys.* **15** *(1972) 675]* **15** (1972), no. 1218.

[9] V. N. Gribov and L. N. Lipatov, *Deep Inelastic ep Scattering In Perturbation Theory, Yad. Fiz. [Sov. J. Nucl. Phys.* **15** *(1972) 675]* **15** (1972), no. 718.

[10] G. Altarelli and G. Parisi, *Asymptotic Freedom In Parton Language, Nucl. Phys.* **B126** (1977), no. 298.

[11] **H1 and ZEUS Collaboration** Collaboration, N. Raicevic, *Structure functions and extraction of pdfs at hera*, .

[12] **H1 and ZEUS Collaboration** Collaboration, K. Wichmann, *Recent results from hera experiments*, .

[13] J. Pumplin, D. R. Stump, J. Huston, H.-L. Lai, P. Nadolsky, and W.-K. Tung, *New generation of parton distributions with uncertainties from global qcd analysis*, *Journal of High Energy Physics* **2002** (2002), no. 07 012.

[14] Y. Petersn, *Single top quark production at the Tevatron*, *FERMILAB-CONF* **12-583-E** (2012).

[15] J. M. Campbell, J. W. Huston, and W. J. Stirling, *Hard interactions of quarks and gluons: a primer for LHC physics*, *Reports on Progress in Physics* **70** (2007), no. 1 89.

[16] N. Kidonakis, *Next-to-next-to-leading soft-gluon corrections for the top quark cross section and transverse momentum distribution*, *Phys.Rev.* **D82** (2010) 114030.

[17] *Combination of ATLAS and CMS results on the mass of the top quark using up to 4.9 fb^{-1} of data*, Tech. Rep. ATLAS-CONF-2012-095, CERN, Geneva, Jul, 2012.

[18] **ATLAS, D0** Collaboration, F. Déliot, *Combination of the top-quark mass measurements from the Tevatron and from the LHC colliders*, tech. rep., 2013.

[19] *Combination of ATLAS and CMS top-quark pair cross section measurements using up to 1.1 fb^{-1} of data at 7 TeV*, Tech. Rep. ATLAS-CONF-2012-134, CERN, Geneva, Sep, 2012.

[20] **ATLAS** Collaboration, *Measurement of the top quark charge in pp collisions at $\sqrt{s}$ = 7 TeV in the ATLAS experiment.*, Tech. Rep. ATLAS-CONF-2011-141, CERN, Geneva, Aug, 2011.

[21] **D0** Collaboration, V. M. Abazov et al., *Observation of single top-quark production*, *Phys. Rev. Lett.* **103** (2009) 092001.

[22] **CDF** Collaboration, T. Aaltonen et al., *Observation of electroweak single top-quark production*, *Phys. Rev. Lett.* **103** (2009) 092002.

[23] N. Kidonakis, *Next-to-next-to-leading logarithm resummation for s-channel single top quark production*, *Phys. Rev. D* **81** (2010) 054028.

[24] N. Kidonakis, *Next-to-next-to-leading-order collinear and soft gluon corrections for t-channel single top quark production*, Phys. Rev. D **83** (2011) 091503.

[25] N. Kidonakis, *Two-loop soft anomalous dimensions for single top quark associated production with a W^- or H^-*, Phys. Rev. D **82** (2010) 054018.

[26] **CDF Collaboration, D0 Collaboration** Collaboration, T. E. W. Group, *Combination of cdf and d0 measurements of the single top production cross section*, .

[27] **ATLAS** Collaboration, *Measurement of the t-channel single top-quark production cross section in pp collisions with the ATLAS detector*, Phys. Lett. B **717** (2012), no. 4–5 330–350.

[28] "ATLAS physics summary plots." `https://twiki.cern.ch/twiki/bin/view/AtlasPublic/CombinedSummaryPlots`.

[29] G. Aad et al., *The ATLAS Experiment at the CERN Large Hadron Collider*, JINST **3** (2008).

[30] "CERN frequently asked questions - LHC, the guide." `https://cdsweb.cern.ch/record/1165534/files/CERN-Brochure-2009-003-Eng.pdf`.

[31] G. Aad et al., *THE CERN LARGE HADRON COLLIDER: ACCELERATOR AND EXPERIMENTS*, JINST **3** (2008).

[32] "ATLAS magnetic field." `http://atlas.web.cern.ch/Atlas/GROUPS/MUON/magfield/mag_page1.html`.

[33] *Trigger Performance - Technical Design Report*, CERN/LHCC 98-15, 1998.

[34] "ATLAS experiment public site." `http://atlas.ch/`.

[35] "Luminosity public results." `https://twiki.cern.ch/twiki/bin/view/AtlasPublic/LuminosityPublicResults`.

[36] **ATLAS Collaboration** Collaboration, G. Aad et al., *Performance of the ATLAS detector using first collision data*, J. High Energy Phys. **09** (May, 2010) 056. 65 p.

[37] H. Pernegger, *Atlas detector upgrade and performance*, .

[38] L. M. Drage, *The Evaluation of Silicon Microstrip Detectors for the ATLAS Semiconductor Tracker and Supersymmetry Studies at the Large Hadron Collider*. PhD thesis, University of Cambridge, 1999.

[39] A. Ahmad et al., *The silicon microstrip sensors of the ATLAS semiconductor tracker*, Nuclear Instruments and Methods in Physics Research Section A: Accelerators, Spectrometers, Detectors and Associated Equipment **578** (2007), no. 1 98 – 118.

[40] P. Behera, T. Lari, and A. L. Schorlemmer, *Measurement of lorentz angle and depletion depth in the ATLAS pixel detector with cosmic rays data*, Tech. Rep. ATL-COM-INDET-2010-041, CERN, Geneva, 2010.

[41] W. Shockley, *Electrons and holes in semiconductors*. Van Nostrand, Princeton N.J., 1950.

[42] S. Gadomski, *Model of the SCT detectors and electronics for the ATLAS simulation using geant4*, Tech. Rep. ATL-SOFT-2001-005, CERN, Geneva, 2001.

[43] D. Varouchas, T. Lari, A. Andreazza, and B. D. Girolamo, *Pixel lorentz angle at sqrt(s) = 900 gev and 7 TeV*, Tech. Rep. ATL-COM-INDET-2010-063, CERN, Geneva, 2010.

[44] C.Jacoboni, *A review of some charge transport properties of silicon, Solid State Electonics* **20** (1977) 77.

[45] C.Canalli, G. Ottaviani, and A. A. Quaranta, *Drift velocity of electrons and holes and associated anisotropic effects in silicon, J. Phys. Chem. Solids* **32** (1971) 1707–1720.

[46] T. E. Seidel and D. L. Sharfetter, *Dependence of hole velocity upon electric field and hole density for p-type silicon, J. Phys. Chem. Solids* **28** (1967) 2563–2574.

[47] V. Rodriguez, H. Ruegg, and M.-A. Nicolet, *Measurement of the drift velocity of holes in silicon at high-field strengths, IEEE Trans. Electron Devices* **14** (1967) 44–46.

[48] T. W. Sigmon and J. F. Gibbons, *Diffusivity of electrons and holes in silicon, Applied Physics Letters* **15** (1969), no. 10 320–322.

[49] C. B. Norris and J. F. Gibbons, *Measurement of high-field carrier drift velocities in silicon by a time-of-flight technique, IEEE Trans. Electron Devices* **14** (1967) 38–43.

[50] M. Bona, M. Castanheira, S. McMahon, E. Piccaro, and P. Ward, *Lorentz angle analysis and measurement for the ATLAS SCT*, Tech. Rep. ATL-COM-INDET-2011-114, CERN, Geneva, 2011.

[51] E. Coniavitis, A. Okamoto, and R. Tanaka, *Lorentz angle and cluster width studies for the ATLAS SCT*, Tech. Rep. ATL-COM-INDET-2009-039, CERN, Geneva, 2009.

[52] CERN, *ROOT - An Object-Oriented Data Analysis Framework*, 2000.

[53] T. Cornelissen, S. Fratina, B. Jackson, C. Schmitt, E. Thomson, and B. Williams, *The Measurement of Cosmic-Ray Time with the Transition Radiation Tracker*, ATLAS note **ATL-COM-INDET-2010-045** (2010).

[54] **ATLAS Collaboration** Collaboration, M. Leyton, *Minimum bias and underlying event measurements with atlas*, .

[55] S. Haywood, *Local Coordinate Frames for the Alignment of Silicon Detectors*, ATLAS note **ATL-COM-INDET-2004-001** (2004).

[56] B. Acharya, S. Adomeit, et al., *Object selection and calibration, background estimations and mc samples for the winter 2012 top quark analyses with 2011 data*, Tech. Rep. ATL-COM-PHYS-2012-224, CERN, Geneva, Feb, 2012.

[57] O. Igonkina and B. Petersen, *Proposal and motivations for 2011 trigger menu*, Tech. Rep. ATL-COM-DAQ-2011-007, CERN, Geneva, Jan, 2011.

[58] S. Frixione and B. R. Webber, *Matching NLO QCD computations and parton shower simulations*, *JHEP* **0206** (2002) 029.

[59] H.-L. Lai, M. Guzzi, J. Huston, Z. Li, P. M. Nadolsky, et al., *New parton distributions for collider physics*, *Phys.Rev.* **D82** (2010).

[60] G. Corcella, I. G. Knowles, G. Marchesini, S. Moretti, K. Odagiri, P. Richardson, M. H. Seymour, and B. R. Webber, *Herwig 6: an event generator for hadron emission reactions with interfering gluons (including supersymmetric processes)*, *Journal of High Energy Physics* **2001** (2001), no. 01 010.

[61] J. Butterworth, J. R. Forshaw, and M. Seymour, *Multiparton interactions in photoproduction at HERA*, *Z.Phys.* **C72** (1996) 637–646.

[62] B. P. Kersevan and E. Richter-Was, *The Monte Carlo event generator AcerMC version 2.0 with interfaces to PYTHIA 6.2 and HERWIG 6.5*, 2004.

[63] T. Sjostrand et al., *Pythia 6.4 - Physics and Manual*, arXiv:hep-ph/0603175, 2006.

[64] M. Cacciari, M. Czakon, M. Mangano, A. Mitov, and P. Nason, *Top-pair production at hadron colliders with next-to-next-to-leading logarithmic soft-gluon resummation*, Phys.Lett. **B710** (2012) 612–622.

[65] M. Czakon, P. Fiedler, and A. Mitov, *The total top quark pair production cross-section at hadron colliders through $O(\alpha_S^4)$*, Comput.Phys.Commun. (2013).

[66] M. Czakon and A. Mitov, *NNLO corrections to top pair production at hadron colliders: the quark-gluon reaction*, JHEP **1301** (2013) 080.

[67] M. Czakon and A. Mitov, *NNLO corrections to top-pair production at hadron colliders: the all-fermionic scattering channels*, JHEP **1212** (2012) 054.

[68] M. Czakon and A. Mitov, *Top++: A Program for the Calculation of the Top-Pair Cross-Section at Hadron Colliders*, .

[69] P. Baernreuther, M. Czakon, and A. Mitov, *Percent Level Precision Physics at the Tevatron: First Genuine NNLO QCD Corrections to $q\bar{q} \to t\bar{t} + X$*, Phys.Rev.Lett. **109** (2012) 132001.

[70] M. L. Mangano, M. Moretti, F. Piccinini, R. Pittau, and A. D. Polosa, *ALPGEN, a generator for hard multiparton processes in hadronic collisions*, JHEP **0307** (2003) 001.

[71] D. Stump, J. Huston, J. Pumplin, W.-K. Tung, H. Lai, et al., *Inclusive jet production, parton distributions, and the search for new physics*, JHEP **0310** (2003) 046.

[72] S. Allwood-Spires, M. Barisonzi, H. Beauchemin, R. Bruneliere, J. Buchanan, N. F. Castro, E. Devetak, C. Feng, J. Ferrando, R. Hawkings, D. Hirschbuehl, U. Husemann, B. P. Kersevan, G. Khoriauli, T. Kuhl, T. Lenz, L. Mijovc, A. Papadelis, M. P. Sanders, L.-Y. Shan, P. Sturm, F. Veloso, W. Verkerke, N. Vlasov, and C. Wasicki, *Monte Carlo samples used for top physics*, Tech. Rep. ATL-PHYS-INT-2010-132, CERN, Geneva, Dec, 2010.

[73] S. Agostinelli et al., *Geant4 - a simulation toolkit*, Nucl Inst Meth A **506** (2003) 250–303.

[74] *Performance of the ATLAS electron and photon trigger in p-p collisions at $\sqrt{s} = 7$ tev in 2011*, Tech. Rep. ATLAS-CONF-2012-048, CERN, Geneva, May, 2012.

[75] M. Hance, D. Olivito, and H. Williams, *Performance studies for e/gamma calorimeter isolation*, Tech. Rep. ATL-COM-PHYS-2011-1186, CERN, Geneva, Sep, 2011.

[76] K. Becker, D. Chakraborty, D. Hirschbuehl, J. Koll, R. Schwienhorst, and C. Suhr, *Measurement of t-channel single top quark production cross section with oldmathpp collisions using a cuts-based approach*, Tech. Rep. ATL-COM-PHYS-2012-1430, CERN, Geneva, Sep, 2012.

[77] M. Cacciari, G. P. Salam, and G. Soyez, *The Anti-k(t) jet clustering algorithm*, JHEP **0804** (2008) 063.

[78] G. Aad et al., *Jet energy measurement with the ATLAS detector in proton-proton collisions at $\sqrt{s} = 7$ TeV*, Eur.Phys.J. **C73** (2013) 2304.

[79] *Commissioning of the ATLAS high-performance b-tagging algorithms in the 7 tev collision data*, Tech. Rep. ATLAS-CONF-2011-102, CERN, Geneva, Jul, 2011.

[80] A. Shibate, *Investigation of Electroweak Production of the Top Quark at the LHC*. PhD thesis, Queen Mary University of London, 2007.

[81] R. Barlow and C. Beeston, *Fitting using finite Monte Carlo samples*, Comp. Phys. Comm. **77** (1993) 219–228.

[82] S. Adomeit, F. Balli, T. Carli, C. Doglioni, D. Gillberg, G. Halladjian, B. Malaescu, L. Mijovic, C. Meyer, A. Picazio, S. Schramm, A. Schwartzman, J. Taenzer, K. Terashi, and D. Lopez Mateos, *Jet energy scale and its systematic uncertainty in proton-proton collisions at sqrt(s)=7 tev with ATLAS 2011 data*, Tech. Rep. ATLAS-COM-CONF-2012-171, CERN, Geneva, Aug, 2012.

[83] *Light-quark and gluon jets in ATLAS: Calorimeter response, jet energy scale systematics and properties*, Tech. Rep. ATLAS-CONF-2012-139, CERN, Geneva, Sep, 2012.

[84] **ATLAS Collaboration** Collaboration, G. Aad et al., *Jet energy resolution in proton-proton collisions at $\sqrt{s} = 7$ TeV recorded in 2010 with the ATLAS detector*, Eur.Phys.J. **C73** (2013) 2306.

[85] M. Botje, J. Butterworth, A. Cooper-Sarkar, A. de Roeck, J. Feltesse, et al., *The PDF4LHC Working Group Interim Recommendations*, tech. rep., 2011.

[86] **CMS Collaboration** Collaboration, A. O. M. Iorio, *Measurements of t-channel single top quark production in pp collisions*, tech. rep., CERN, Geneva, Oct, 2013.